1225-0767(ISSN Print)
2287-6715(ISSN Online)
한국연구재단 우수등재학술지

Journal of Ocean Engineering and Technology

Vol. 35, No. 4 (Serial Number 161)

August 2021

한국해양공학회지

KSOE

www.joet.org

KSOE The Korean Society of Ocean Engineers

Journal of Ocean Engineering and Technology
한국해양공학회지
Vol. 35 No. 4
(Serial Number 161)
August 31, 2021
www.JOET.org

Editorial Board

Research and Publication Ethics Committee

Published on August 31, 2021
Published by The Korean Society of Ocean Engineers (KSOE)
Room 1302, 13, Jungang-daero 180beon-gil, Dong-gu, Busan, 48821, Korea
TEL: +82-51-759-0656 FAX: +82-51-759-0657 E-mail: ksoehj@ksoe.or.kr URL: http://www.ksoe.or.kr
Printed by Hanrimwon Co., Ltd., Seoul, Korea E-mail: hanrim@hanrimwon.co.kr
ISSN(print) 1225-0767 **ISSN(online)** 2287-6715

This journal was supported by the Korean Federation of Science and Technology Societies (KOFST) grant funded by the Korean government.

Journal of Ocean Engineering and Technology
한국해양공학회지

CONTENTS

Volume 35, Number 4 August, 2021

<Original Research Articles>

GENERAL INFORMATION

"Journal of Ocean Engineering and Technology" is the official journal published by "The Korean Society of Ocean Engineers (KSOE)". The ISO abbreviation is "J. Ocean Eng. Technol." and acronym is "**JOET**". It was launched in 1987. It is published bimonthly in February, April, June, August, October, and December each year. Supplement numbers are published at times.

Journal of Ocean Engineering and Technology (JOET) is a medium for the publication of original research and development work in the field of ocean engineering. JOET covers the entire range of issues and technologies related to the following topics:

Ships and offshore platforms: Design of marine structures; Resistance and propulsion; Seekeeping and maneuvering; Experimental and computational fluid dynamics; Ocean wave mechanics; Fatigue strength; Plasticity; Optimization and reliability; Arctic technology and extreme mechanics; Noise, vibration, and acoustics; Concrete engineering; Thermodynamics and heat transfer; Hydraulics and pneumatics;
Coastal civil engineering: Coastal structures; Port and harbor structures; Soil mechanics; Drilling and exploration; Hydraulics of estuary; Seismic engineering; Coastal disaster prevention engineering;
Ocean renewable energy platforms: Offshore wind turbines; Wave energy platforms; Tidal current energy platforms; Floating photovoltaic energy platforms;
Marine robots: Robot sensor system; Autonomous navigation; Robot equipments; Spatial information and communications; Underwater network; Design of underwater vehicles;
Multidisciplinary areas: Design for safety; IT-based design; IT-based production engineering; Welding mechanics; Control engineering; GPS and GIS; Inspection and sensor; Port and logistics; Leisure boat and deep see water; Offshore process systems engineering; Marine metallic materials; Marine organic materials; Marine Composite materials; Materials properties; Corrosion and Anti-corrosion; Tribology;

It contains original research articles, case reports, brief communications and reviews on technial issues. Conference papers, research papers, diploma papers and academic articles can be submitted.

All of the manuscripts are peer-reviewed. **JOET** has a system where two or more peer reviewers must review each submitted paper and it is operated very strictly.

JOET is being indexed in some prominent database such as Korean Citatation Index (KCI), Google Scholar, Science Central, Korea Science and Directory of Open Access Journals (DOAJ).

For correspondences concerning business matters, author needs to contact KSOE Secretariat by email or phone (e-mail: ksoehj@ksoe.or.kr or Tel: +82 51 759 0656). Correspondences for publication matters can be asked via email to the Editor-in-Chief (email: heroeswise2@gmail.com).

KSOE

Journal of Ocean Engineering and Technology 35(4), 247-256, August, 2021
https://doi.org/10.26748/KSOE.2021.015

pISSN 1225-0767
eISSN 2287-6715

Original Research Article

Computational Analysis of KCS Model with an Equalizing Duct

Joseph Mwangi Ng'aru[1], Sunho Park[2] and Beom-soo Hyun[3]

[1]*Graduate Student, Department of Naval Architecture and Ocean Systems Engineering. Korea Maritime and Ocean University, Busan, Korea*
[2]*Associate Professor, Department of Ocean Engineering, Department of Convergence Study on the Ocean Science and Technology. Korea Maritime and Ocean University, Busan, Korea*
[3]*Professor, Department of Naval Architecture and Ocean Systems Engineering. Korea Maritime and Ocean University, Busan, Korea*

KEY WORDS: Energy saving device (ESD), Computational fluid dynamics (CFD), OpenFOAM, KCS, Equalizing duct

ABSTRACT: *In order to minimize carbon emissions and greenhouse gas, the Energy Efficiency Design Index (EEDI) has become a major factor to be considered in recent years in a ship's design and operation phases. Energy-Saving Devices (ESDs) improve the EEDI of a vessel and make them environmentally friendly. In this research, the performance of an equalizing duct-type ESD installed upstream of a Korea Research Institute of Ships & Ocean Engineering (KRISO) Container Ship (KCS) model's propeller was investigated by computational fluid dynamics (CFD). Open-source CFD libraries, OpenFOAM, were used for computational analysis of the KCS with and without the ESD to verify the performance improvement. The flow field near the stern region and propulsive coefficients were considered for comparison. The results showed a considerable improvement when an ESD was used on the model. Using different sizes of the duct, the performance of the ESD was also compared. It was observed that with an increased duct size, the propulsive performance was improved.*

1. Introduction

The enforcement of the energy efficiency design index (EEDI) as an approach to decarbonization has led to a focus on improvement and further verification of the hydrodynamic performance of energy-saving devices (ESDs) used on ships to improve propulsion efficiency. With screw propellers still being a dominant propulsion device, the need for energy savings and emissions reduction has prompted research in ESDs that are related to propulsion efficiency. An efficiently and optimally designed hull and propeller can significantly recover lost energy during propulsion when used in conjunction with the ESDs. In recent years, ESDs have been crucial for both old vessels seeking retrofitting and new buildings. The improvement in propulsion performance from these devices plays a crucial role in complying with the EEDI and reduction of fuel consumption.

Various types of ESDs are being used in the shipping industry. Some ESDs have been used to modify flows upstream and downstream of the propeller. An ESD in front of the propeller improves the inflow to the propeller plane. One downstream of the propeller makes use of the rotational flow of the propeller slipstream. In other cases, a composite device uses both mechanisms.

Kim et al. (2013) investigated a design of a duct-type ESD attached to the stern of a very large crude oil carrier (VLCC) hull. The research used computational fluid dynamics (CFD) simulation and considered the duct flow field, the hydrodynamic effects on resistance, and propulsive performance. Numerical flow analysis identified a reduction of hull resistance by the straightening effect of the stern flow and pressure recovery on the stern region. The power reduction was calculated to be 5%.

Bart and van Terwisga (2017) studied the effects of a duct and nozzles on propulsion devices. Koushan et al. (2020) considered a pre-swirl ESD that had fixed lifting foils mounted in front of a screw propeller. Using the lifting surface vortex model, the results showed an increase in 4% at the design point in comparison to when the ESD was not used. There are many ESDs that provide flow to the propeller by use of a pre-swirl stator (PSS) (Krol and Tesch, 2018; Henrich and Yan, 2017). The use of a composite device that incorporates a duct and pre-swirl stators has been extensively researched. The duct provides uniform velocity distribution to the propeller plane in addition to providing more thrust by use of the foil section. Such a device is a Mewis duct that incorporates fins to improve energy-saving performance (Mewis and Guiard, 2011).

When a duct is placed in front of a propeller, it has similar effects that are almost equal to those of a nozzle around a propeller. Nozzles

Received 15 March 2021, revised 13 May 2021, accepted 2 July 2021
Corresponding author Sunho Park: +82-51-410-4329, spark@kmou.ac.kr

around a propeller are used to improve efficiency of the propeller due to their ability to accelerate the flow through the propeller plane. An increase of flow to the propeller plane increases the mass flux through the propeller, in turn contributing to a high amount of efficiency. A duct used in the ducted propeller is also believed to cut down the amount of axial kinetic energy losses and increase the flow rate through the propeller disk. Furthermore, it can be used to capture the viscous wake through the propeller wake, thereby increasing the propeller-hull interaction contribution to the efficiency (Bart and van Terwisga, 2017).

CFD has become an essential tool for the design of an ESD due to its ability to analyze a detailed flow that cannot be captured in experimental methods. Open-source software has gained extensive use in the ship building industry in the study of resistance, self-propulsion, and ship motions in waves. Park et al. (2013) developed a solver using open-source libraries for shipbuilding. Shen et al. (2014) applied dynamic overset grids in OpenFOAM for the self-propulsion and maneuvering of the Korea Research Institute of Ships & Ocean Engineering (KRISO) container ship (KCS). Seo (2017) used OpenFOAM to study the effects of wave periods on added resistance and motion of a ship in head simulations. Go et al. (2017) studied the effects of a duct before a KP505 propeller on the propulsion performance without a hull form. From the results, it was found that the duct is applicable to high-speed vessels such as containers.

The present work discusses the use of an equalizing duct-type ESD located upstream of the KCS model's propeller. The thrust improvement and flow through the duct have been analyzed to study the effects of the equalizing duct-type ESD. The duct was realized with a sectional NACA 4420 profile with an angle of attack of 20 degrees. Stators for the duct were not considered in this study. The performance of the KCS model with the equalizing duct-type ESD was compared with that of a KCS model without a duct. Three sizes of ducts were used for comparison to study how the duct's size relative to the propeller diameter affects the generated thrust by the propeller.

2. Model Description

Fig. 1 shows the baseline of the equalizing-type ESD. The hydrofoil cross section is a NACA4420. The hydrofoil has an angle of attack (AOA) of 20 degrees and constant duct length and chord length. The diameters (D_{ESD}) used were $0.6D_P$, $0.7D_P$, and $0.8D_P$, where D_P is the propeller diameter. $0.8D_P$ was used as the maximum outlet diameter since a diameter larger than that would extend beyond the model's keel.

3. Computational Methods

3.1 Governing Equations

To ship studied follows the continuity and Navier-Stoke's equations:

$$\nabla \cdot \vec{U} = 0 \tag{1}$$

$$\frac{\partial \vec{U}}{\partial t} + (\vec{U} \cdot \nabla)\vec{U} = -\nabla p + \nabla \cdot (\nu + \nu_t)(\nabla \vec{U} + \nabla \vec{U}^T) \tag{2}$$

where $\vec{U}$ is the velocity vector, p is the pressure, ν is the kinematic viscosity, and ν_t is the turbulent kinematic viscosity. The k-w SST turbulence model was used for the turbulence closure (Menter, 1993). We captured the free surface using OpenFOAM's multiphase solver with the volume of fluid (VOF) method and interFoam.

3.2 Numerical Methods

The Reynolds-averaged Navier Stokes (RANS) equations were discretized using the finite volume method (FVM). A second-order-accurate transient bounded-time-derivative Crank Nicolson scheme was used. The gradient schemes were discretized using the total variation diminishing (TVD) schemes with the van Leer limiter (van Leer, 1979). The second-order limited approach has been used to solve for the Laplacian term and the convection terms were solved using second-order schemes. The diffusion terms were solved using the central differencing schemes. The PIMPLE algorithm was used to couple the velocities and the pressure fields. The algorithm combines the "pressure implicit with splitting of operator" (PISO) method and semi-implicit method for pressure-linked equations (SIMPLE) (Gaggero et al., 2015).

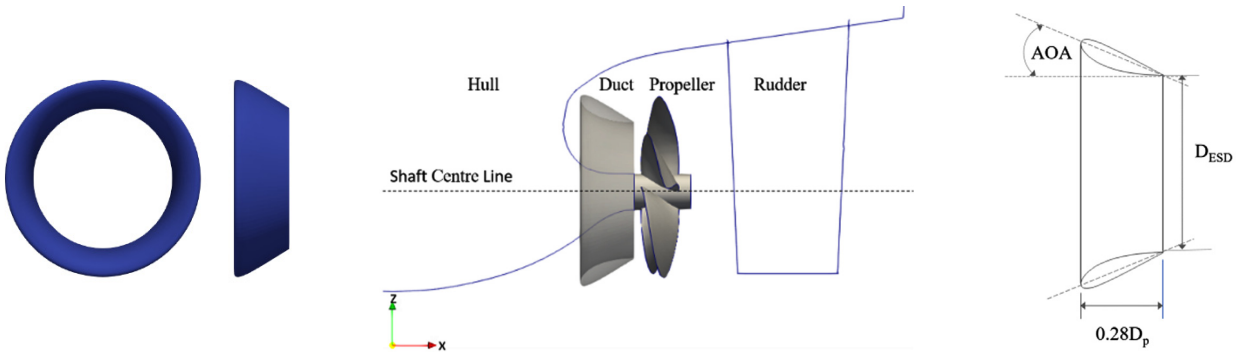

(a) Front and side view of duct (b) Duct location at stern (c) Duct cross section

Fig. 1 Equalizing duct-type ESD

4. Results and Discussion

4.1 Resistance

For the bare hull resistance of the KCS model, a computation was carried out at the design speed with a Froude number (*Fn*) of 0.26. Fig. 2 shows the grid and domain used for the resistance and propulsion. The domain extent was set to $1.0L_{PP}$ in the forward direction, $3L_{PP}$ in the stern direction, $1.0L_{PP}$ in the width direction, and $0.5L_{PP}$ and $1.5L_{PP}$ above and below the free surface, respectively. L_{PP} is the length between perpendiculars of the KCS model.

The Dirichlet conditions were applied for the velocity, turbulence, and volume fraction at the inlet boundary and the pressure at the outlet boundary. The Neumann conditions were applied for the pressure at the inlet boundary and the velocity, turbulence, and volume fraction at the outlet boundary. During forward ship motion in calm water, a wave is generated from the bow area, while in the stern region, flow separation occurs. Therefore, during mesh preparation, a high mesh resolution was given around the bow and stern region to capture the flow effects. In addition, the fluid interface region was also given high mesh resolution to accurately predict the ship resistance in calm water.

Table 1 shows the total resistance coefficient ($C_T = R_T/(\frac{1}{2}\rho U^2 S)$) for three grids. The difference (%*D*) is the percentage difference from the experimental data. The difference between the experimental resistance coefficient (C_T) and computed data was 3.457% for the fine mesh and 6.638% for the coarse mesh. The computed results for the resistance have been overestimated. During the simulation, it was observed that the result improved with the use of a finer mesh.

Table 1 Resistance results

Grid sets	Background mesh	Number of grids	C_T ($\times 10^{-3}$)	Difference (%)
1	45 × 11 × 28	4,023,280	3.840	3.457
2	32 × 9 × 20	2,157,269	3.878	4.511
3	25 × 6 × 15	1,362,365	3.957	6.638

4.2 Propeller Open Water (POW)

A steady-state solver with a moving reference frame (MRF) approach was used for computations of the complete propeller geometry. In the MRF approach, the simulation of the propeller is divided into two cell zones. The zone with the propeller is set as the rotating cell zone as shown in Fig. 3. The flow is inversely rotated instead of the actual propeller, so there is no actual relative propeller rotation. The MRF approach is fast, steady, and takes a short time to attain convergence. When using the MRF approach to solve the governing equations, the effects of centrifugal and Coriolis forces resulting from the angular velocity are considered as body terms in the

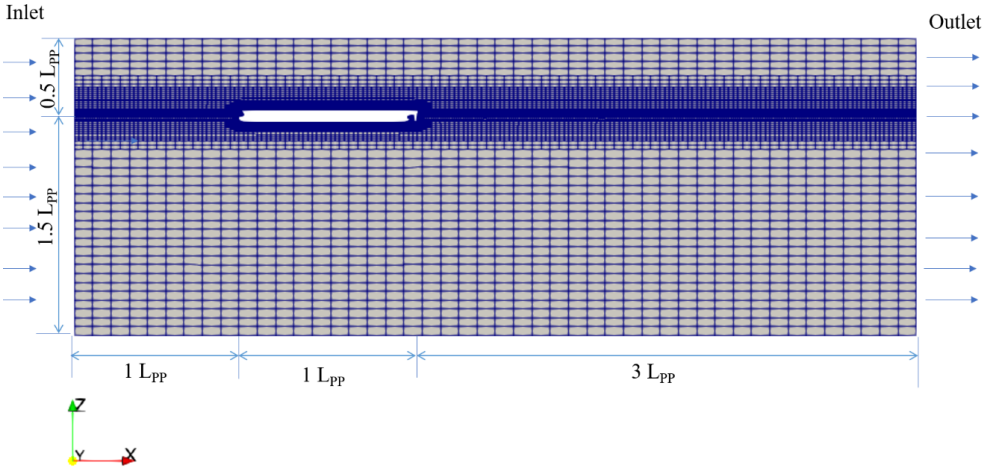

Fig. 2 Computation domain and grid for resistance

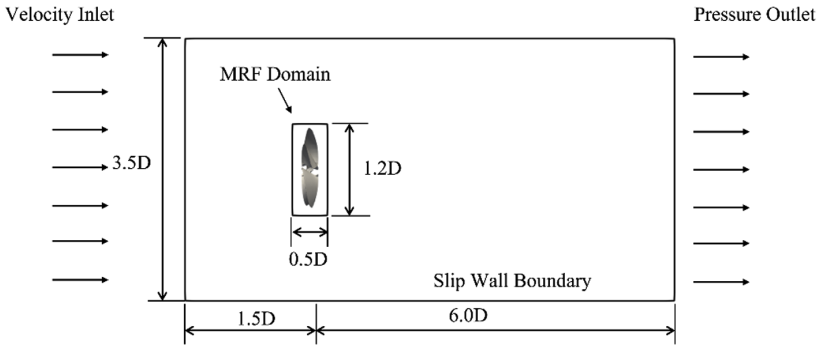

Fig. 3 Computational domain for POW

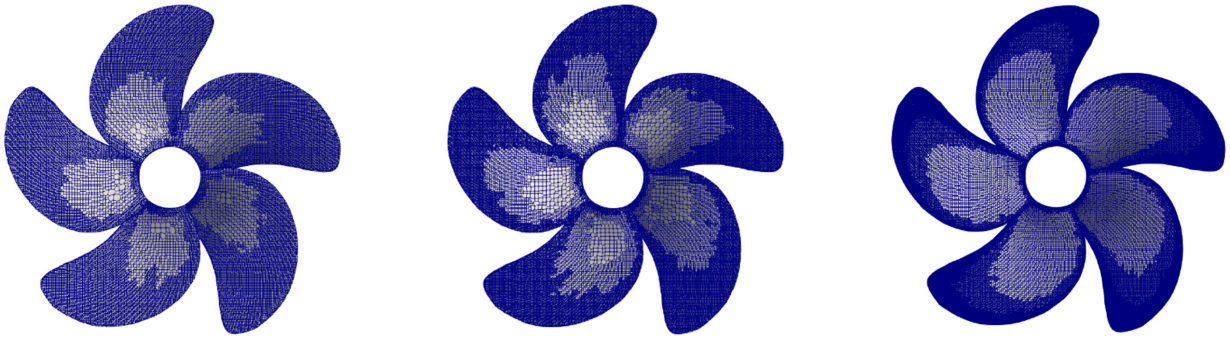

(a) Coarse mesh (b) Medium mesh (c) Fine mesh

Fig. 4 Propeller surface meshes

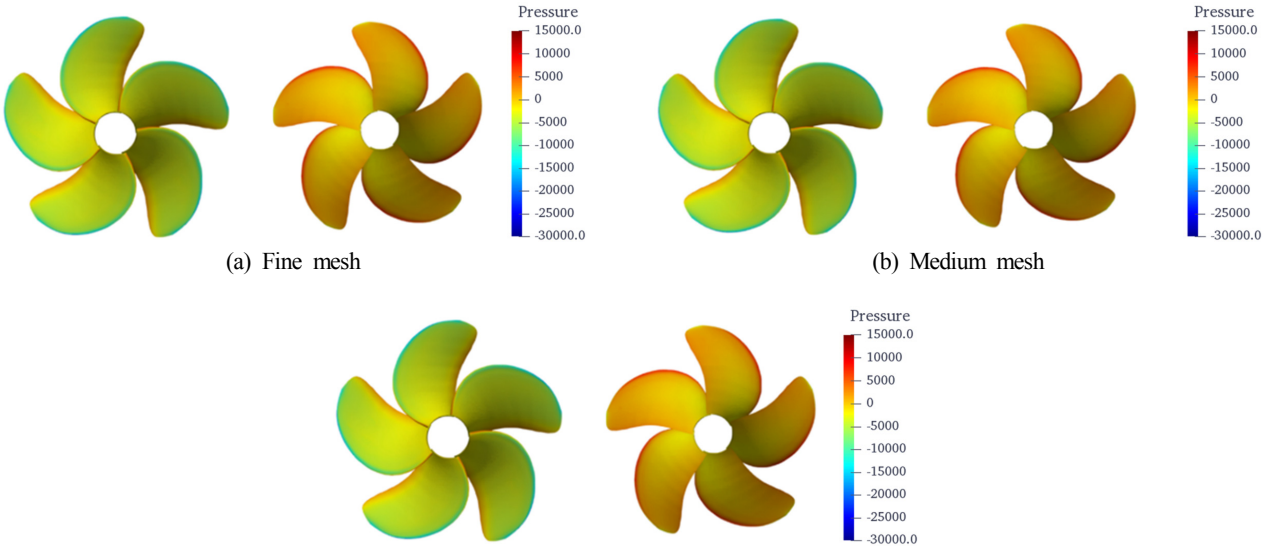

(a) Fine mesh (b) Medium mesh

(c) Coarse mesh

Fig. 5 Pressure distribution on the propeller blades at $J = 0.6$.

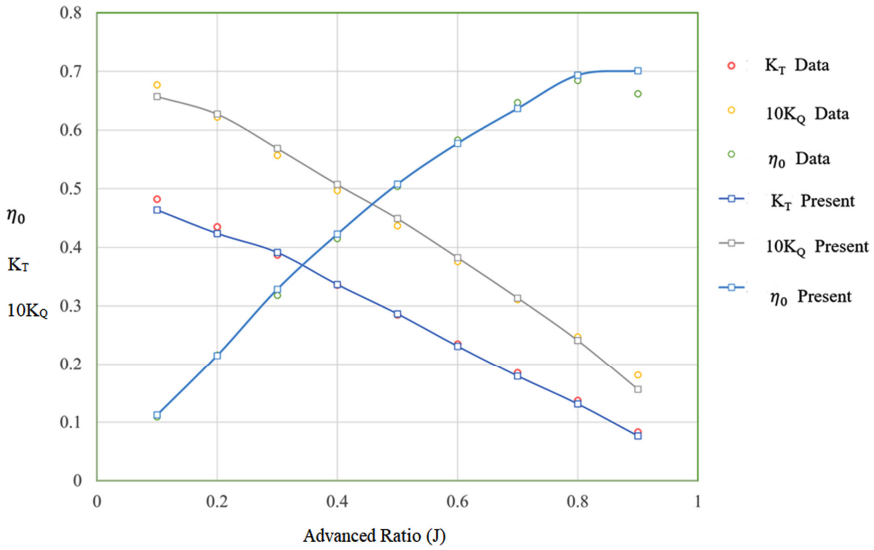

Fig. 6 Propeller open-water results

momentum equations (Seb, 2017).

The number of cells in the open-water simulation was limited when considering self-propulsion. Fig. 4 shows the three grids. The meshes around the leading and trailing edges and tip were resolved. Fig. 5 shows the pressure contours at the pressure and suction sides of the propeller blades for three grids at an advance ratio (J) of 0.6. In the

coarse mesh, low pressure at the tip was observed. Fig. 6 shows the POW results. The present data were compared with experimental data. The computational results agree with the experimental data, meaning the approach works well for open-water cases, and the propeller experiences a uniform inflow field. The error found between the present computation and experiment is generally low apart from the data at high advance coefficients.

4.3 Self-propulsion

For the computations of self-propulsion, an unsteady VOF solver was used with dynamic mesh motions and a sliding mesh to enable propeller rotation using the arbitrary mesh interface (AMI) method.

Table 2 Self-propulsion without ESD

	Revolutions (rps)	R_T (N)	T (N)	Balance (T - $R_{T(SP)}$ + SFC)	Torque (N·m)
Computation	9.5	95.3	50.00	-13.100	2.535
	10	99.250	67.110	0.060	2.725
Interpolation	9.998	99.232	67.032	0	2.724

Table 3 Validation data for KCS model without ESD

Item	EFD (NMRI)	KRISO	HSVA	SVA	Present	%D[1)]
K_T	0.170	-	-		0.172	0.588%
$10K_Q$	0.288	-	-	-	0.279	-3.125%
$1\text{-}t$	0.835	0.846	0.865	0.910	0.835	0.0 %
J	0.728	0.729	0.725	0.708	0.72	1.098%
η_0	0.682	0.671	0.667	0.614	0.673	-1.173%
η_R	1.011	1.023	0.981	1.007	1.035	2.374%
$1\text{-}w$	0.792	0.779	0.789	0.765	0.819	3.409%
n	9.500	9.380	9.560	9.500	9.998	5.242%
η_D	0.740	0.746	0.717	0.618	0.710	-4.054%

1) $\%D = \dfrac{present - EFD}{EFD}$

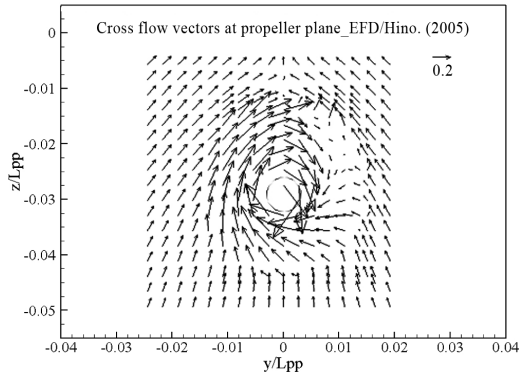

(a) Crossflow vectors (EFD)

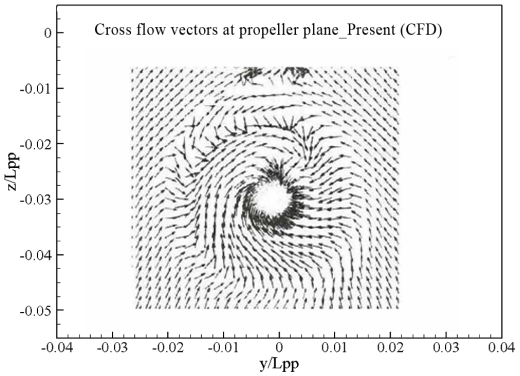

(b) Crossflow vectors (Present)

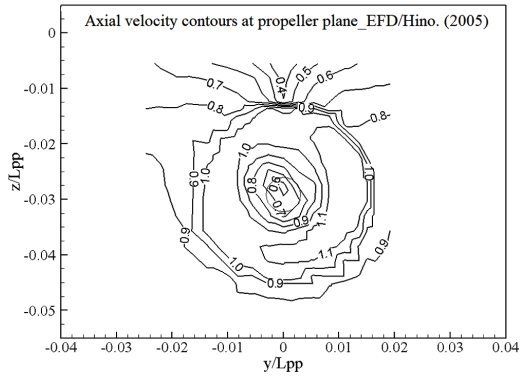

(c) Axial flow contours (EFD)

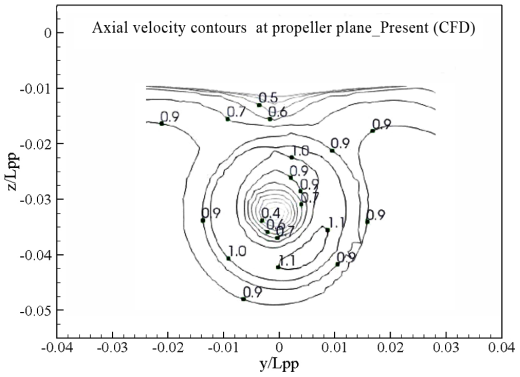

(d) Axial flow contours (Present)

Fig. 7 Wakes of propeller plane (x/L_{PP} = 0.9911)

The revolution speeds (n) were 9.5 rps and 10 rps. From the simulation values obtained for each revolution, balance is obtained, and linear interpolation is done to obtain the ship propulsion. To obtain the skin friction coefficient (SFC), a series of double body resistance computations was done at slow speed for a range of $Fn \in [0.1, 0.2]$ using Prohaska's method (Birk, 2019). The SFC was obtained as 32.2 N.

Table 2 shows the results for two revolutions at 9.5 rps, 10 rps, and the interpolation point. From the interpolation data in Table 2, revolution n = 9.998 was found to be the revolution at which the equilibrium point was obtained. The related thrust (T) of 67.032 and torque (Q) of 2.724 N·m are the parameters associated with the equilibrium point.

The result obtained from the KCS model without ESD can be compared with the experimental data and simulations (Larsson et al., 2015), and the results are shown in Table 3. At 9.5 rps, the computation overestimated the resistance by 4.2%. In the experimental data, the self-propulsion point was obtained at 9.5 rps, while in the present case, the self-propulsion point was obtained at 9.998. This variation can be attributed to a few factors, such as the number of grids due to the limitation of the number of cells used after considering the available computation resources. Also, the overestimation of the resistance could have contributed to this variance.

At the self-propulsion point, the value of K_T was approximately equal to the experimental value of K_T. Conversely, the value of K_Q was underpredicted by around 3.125%. η_D is the ultimate goal for the self-propulsion computation in the present case and was underestimated by 3.784%, as shown in Table 3. Even though the thrust deduction shows some agreement with the experimental data, the effective wake coefficient shows a little discrepancy of about 3.535%.

The cross-vector flows and axial flow contours were plotted for the KCS model during self-propulsion, as shown in Fig. 7. Wake contours were compared at x/L_{PP} = 0.9911. For the overall wake shape, the results without ESD agree well with EFD data (Hino, 2005). The swirl in the present case seems to be overestimated.

4.4 Self-Propulsion with Equalizing Duct-Type ESD

This section presents data for a model with the equalizing duct-type ESD installed upstream of the propeller. The results were compared with the KCS model results without the ESD to analyze its effectiveness. Table 4 shows the results of self-propulsion with the equalizing duct-type ESD at $D_{ESD} = 0.55D_P$. Revolution n = 9.89 was found to be the approximate revolution at which self-propulsion point was obtained. The thrust T = 66.855 N and torque Q = 2.600 N·m are the parameters associated with the self-propulsion point.

Table 5 compares the propulsive coefficients for the cases with and without the ESD. Considering the two scenarios for these cases, the thrust coefficient shows an increase when the ESD is used on the KCS model. The improvement of thrust delivered at the self-propulsion point represents a 2.35% increase when the two cases are compared. From the interpolation results, the KCS model with the ESD was observed to reach self-propulsion earlier at 9.89 rps as compared to the model without ESD at n = 9.998 rps.

Table 4 Interpolation data for KCS model with ESD

	Revolution (rps)	R_T (N)	T (N)	Balance	Torque (N·m)
Computation	9.5	95.767	51.502	12.067	2.105
	10	99.850	70.401	-2.750	2.712
Interpolation	9.89	99.035	66.855	0	2.600

Table 5 Comparison of KCS model data with and without ESD

Item	Present w/o ESD	Present w/ ESD
K_T	0.172	0.175
$10K_Q$	0.279	0.271
$1\text{-}t$	0.835	0.837
J	0.720	0.715
η_0	0.673	0.67
η_R	1.035	1.058
$1\text{-}w$	0.819	0.805
n	9.998	9.89
η_D	0.710	0.7379

Comparing the thrust for the two cases while on the same number of revolutions, the thrust for the KCS model with the ESD is greater than for the case without the ESD, as shown in Tables 2 and 4. This can be related to the flow that is directed to the propeller by the duct. The change in resistance values for both cases is insignificant. Comparing the quasi-propulsive efficiency of the ship model with and without the ESD, the performance shows improvement of about 3.929%, which is attributed by the improved upstream flow to the propeller.

Different locations were considered to compare the effects of flow with and without the ESD at various points in the stern region around the propeller, as shown in Fig. 8. Flow-through points 1, 2, 3, and 4 represent x/L_{PP} = 0.96, 0.97, 0.98, and 0.99, respectively, and are presented in Fig. 9. The axial flow distribution for the case with the

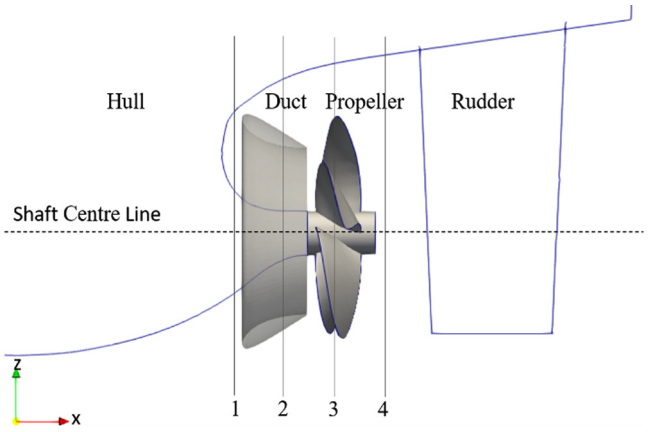

Fig. 8 Flow measurement planes around stern

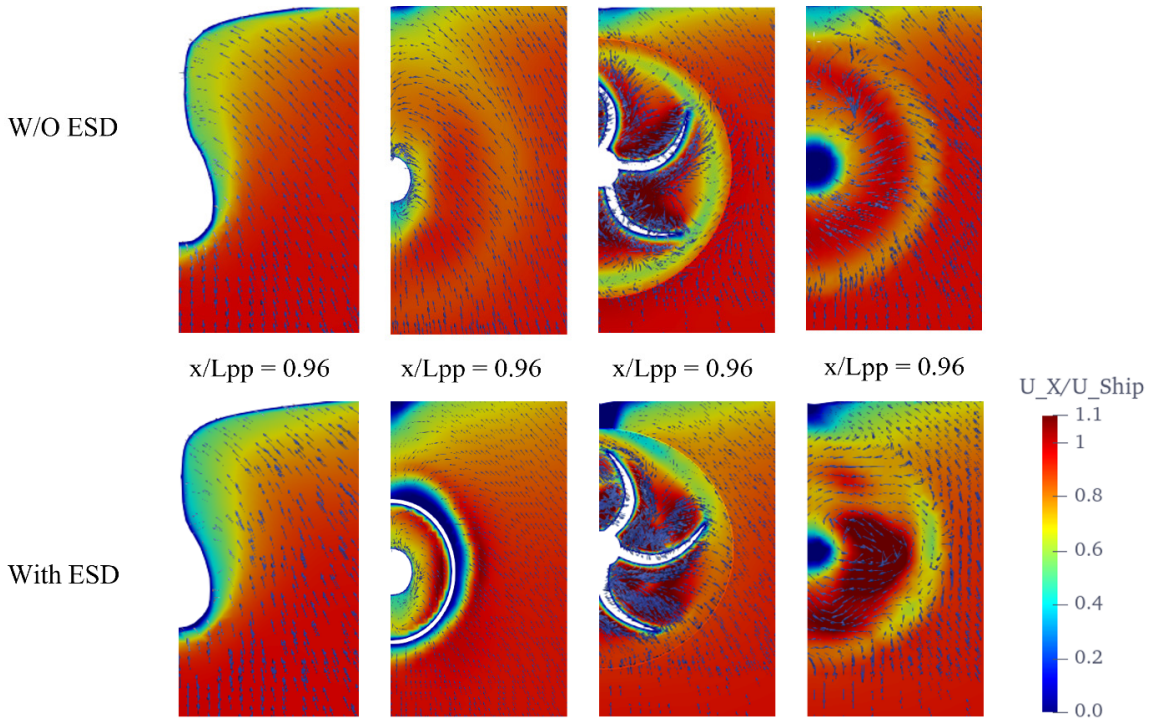

Fig. 9 x-velocity contours for KCS model without and with ESD

duct is distinct in that fast flow induced by the duct is concentrated. Downstream of the duct, the duct' effects are evident. There are distinct variations along the circumferential direction on the duct as the axial velocity near the outer side of the duct becomes weaker due to the duct's angle of attack. On the stern side, the wake of the ship can be seen to influence the propeller, and the propeller also influences the ship flow.

4.5 Effect of the Outlet Diameter for Equalizing Duct type ESD

Three outlet diameter sizes for the duct were considered and compared at 9.5 and 10 rps. The ducts had equal length and angle of attack with only a change in the diameter of the duct. The diameter of the baseline duct was $0.7D_P$. A bigger one ($0.8D_P$) and a smaller one ($0.6D_P$) were considered. $0.8D_P$ was the maximum duct size that could have been used since a larger size would have extended below the keel. In comparison to the duct with an outlet diameter of $0.55D_P$, the ducts with larger diameters of $0.6D_P$, $0.7D_P$, and $0.8D_P$ showed improvement in the propulsive performance at the self-propulsion point, as shown in Table 6. When the duct's outlet diameter was $0.8D_P$, the results showed the highest thrust output compared to the other ducts sizes. With the increased diameter size, the thrust of the propeller was observed to improve.

In this type of hull design, the stern of the ship is well designed, so the difference of the resistance forces was insignificant for all cases with and without a duct. Therefore, the propeller performance became the focal point. In the performance comparison to the model without the ESD, all the cases with the ESD showed improved propulsive performance. This is shown in both Tables 5 and 6. Both the propeller thrust and torque increase with the size of the duct. With the increased size of the duct, Fig. 10 shows that the wake fraction (w) was increased, while the thrust ratio (t) was reduced, thereby increasing the hull efficiency performance.

Table 6 Performance of KCS model with ESD and various D_{ESD}

Item	$0.55D_P$	$0.6D_P$	$0.7D_P$	$0.8D_P$
K_T	0.175	0.176	0.180	0.187
$10K_Q$	0.271	0.276	0.290	0.318
$1-t$	0.837	0.8474	0.862	0.879
J	0.715	0.71	0.700	0.685
η_0	0.67	0.655	0.640	0.63
η_R	1.053	1.106	1.085	1.0367
$1-w$	0.805	0.7931	0.766	0.726
n	9.89	9.813	9.609	9.329
η_D	0.7378	0.7736	0.7812	0.789

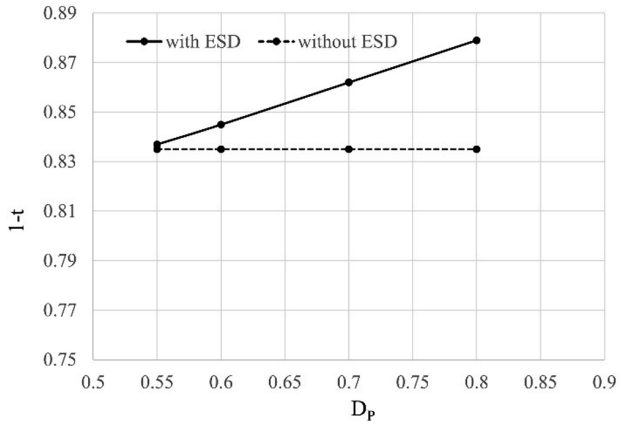

(a) Thrust deduction

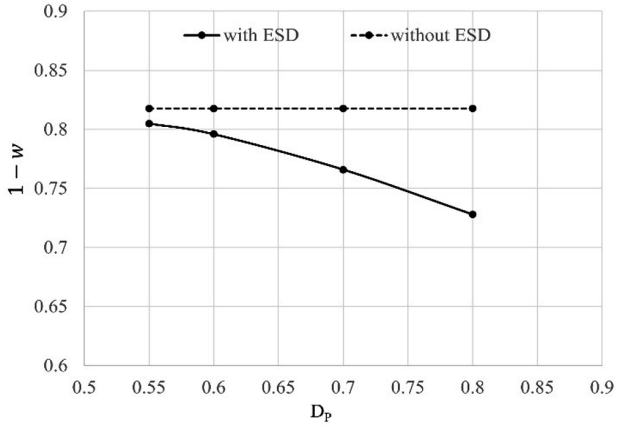

(b) Wake fraction

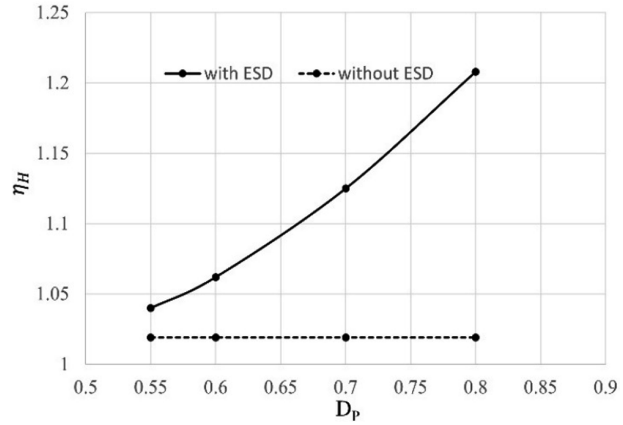

(c) Hull efficiency

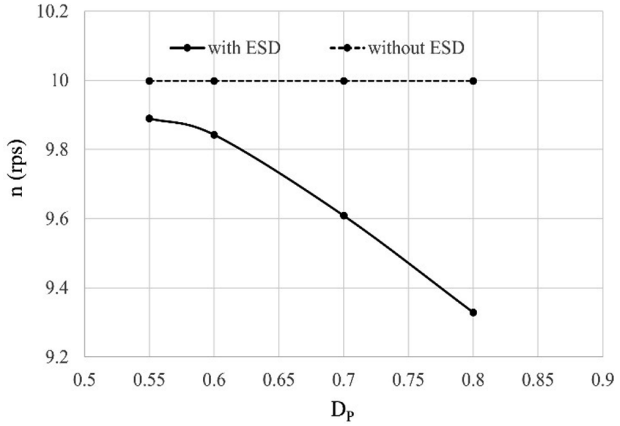

(d) Self-propulsion point

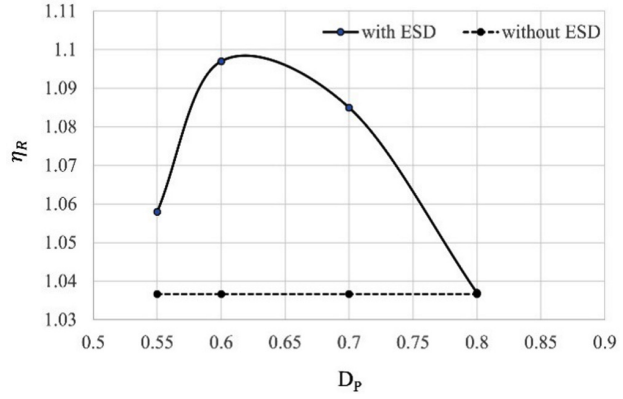

(e) Relative rotative efficiency

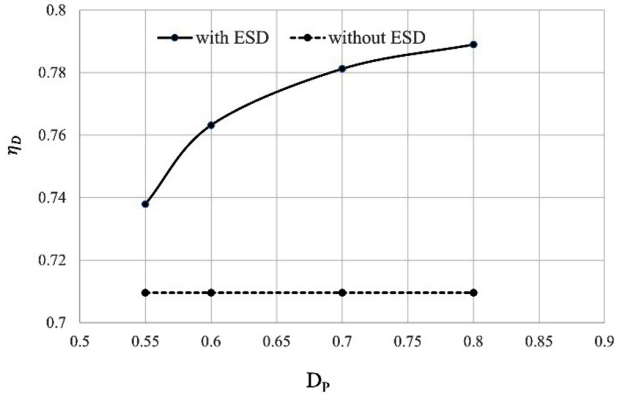

(f) Propulsive efficiency

Fig. 10 Propulsion performance for different duct sizes

Fig. 10(d) shows that the self-propulsion point was achieved earlier as the thrust generated by the propeller was higher than in the case without the ESD. The self-propulsion point was obtained with less revolution as the duct size increased, which was due to the increased thrust generated by the propeller. As the size of the duct increased, the overall efficiency η_D also increased.

The relative rotative efficiency is highest between $0.6D_P$ and $0.65D_P$. At $0.8\ D_P$, which is the highest size of the duct in this case, the relative rotative efficiency is almost equivalent to the case without a duct. In Fig. 10(f), the propulsive performance steeply increases until $0.7D_P$, and between $0.7D_P$ and $0.8D_P$, the propulsive efficiency change is small, which may be a result of reduced relative rotative efficiency and open-water propeller efficiency. Despite the largest duct giving the highest propulsion efficiency, its relative rotative efficiency is almost equivalent to the case without a duct Fig. 10(e). It is insufficient to say that it is the most effective duct because this case requires a different angle of attack for comparison and other aspects of the design of the duct. The improvement in the performance of the propulsive

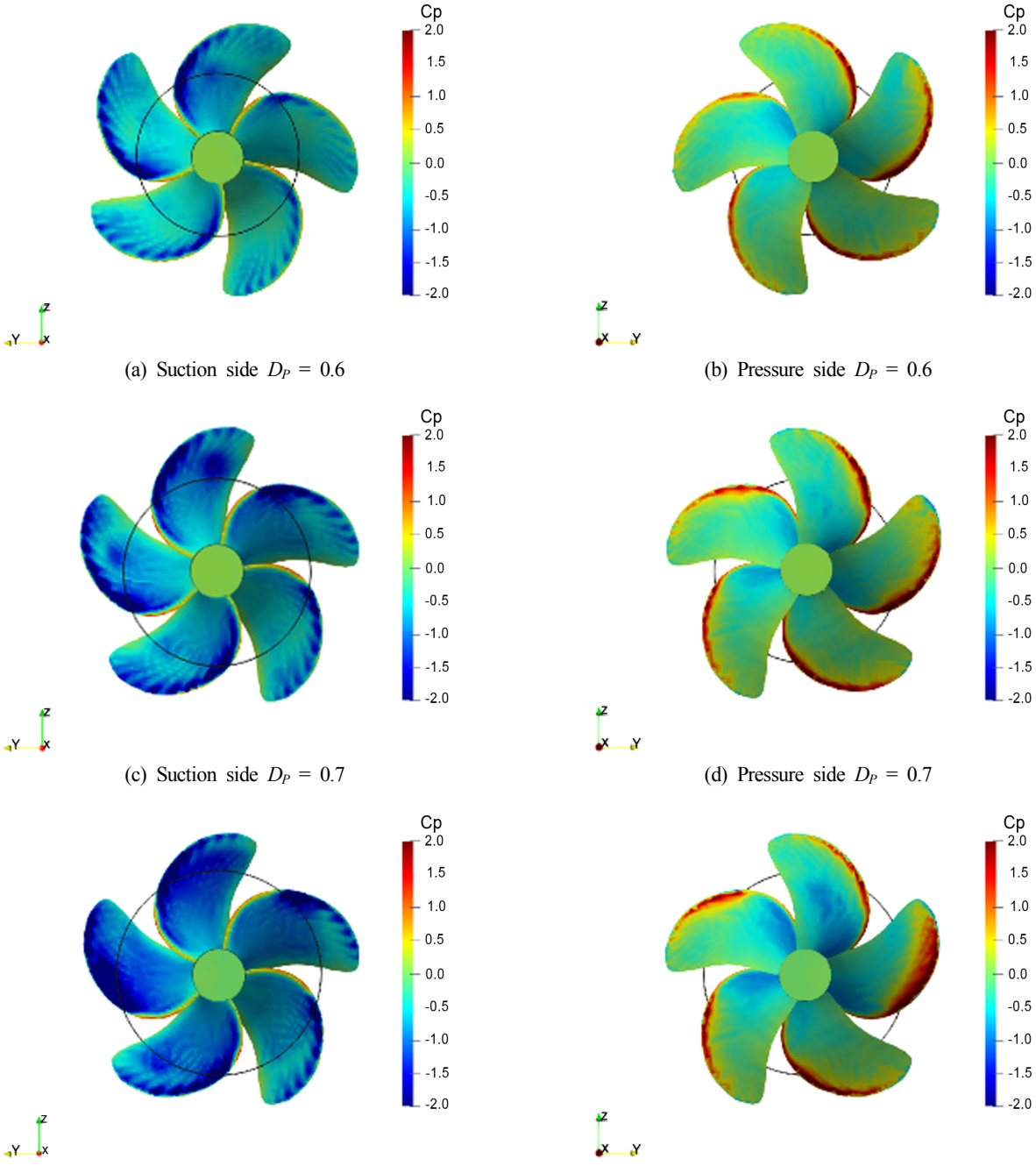

(a) Suction side D_P = 0.6 (b) Pressure side D_P = 0.6

(c) Suction side D_P = 0.7 (d) Pressure side D_P = 0.7

(e) Suction side D_P = 0.8 (f) Pressure side D_P = 0.8

Fig. 11 Pressure coefficient contours on the propeller blades

system using the duct maybe attributed to enhancement of the mass flow rate passing through the propeller disk and the reduction of the drag force on the blades of the propeller.

Fig. 11 shows the pressure contours of the propeller blades for different outlet diameters of the ESD. The pressure of the suction side decreases with the increased diameter of the duct outlet. The pressure distribution on the propeller blade varies with the size of the duct, especially on the suction side. On the pressure side, higher pressure is observed on the tip of the propeller when a larger duct is used. This may lead to undesirable pressure loading on the propeller. The pressure loading on the tips shifted with the duct size, with a large diameter resulting in higher loading at the propeller tip than a smaller diameter.

5. Conclusions

This study presented a computational analysis for a KCS model with an ESD. The computations were done for cases with and without an ESD, and results were compared to study its effectiveness. For the propeller open-water test, the MRF approach was considered, and results were compared with experimental data. The data showed good agreement with the experimental data for the KCS model without the

ESD. In the self-propulsion of KCS, non-dimensionless propulsive factors such as the thrust coefficient, wake fraction, and relative rotative efficiency with and without the ESD were compared.

The performance of the ESD showed some significant improvement in the propulsion. With increased size of the duct, the propeller thrust increased. The pressure loading shifted to the propeller blade tips as the duct size increased. However, there are many points to improve for further development in this case, such as coupling of the ship dynamic motion with the sliding mesh motion. Even though the comparison seems qualitatively promising, there is a need for further study to obtain more consistency, insights, and understanding in the future. In the future, more parameters such as the angle of attack and incorporation of fins should be considered.

Funding

This research was supported by the National Research Foundation of Korea (NRF-2018R1A1A1A05020799, NRF-2021R1I1A3044639).

References

Bart, S., & van Terwisga, T. (2017). Hydrodynamic Working Principle of Energy Saving Devices in Ship Propulsion Systems. International Shipbuilding Progress, 63(3−4), 255−290. https://doi.org/10.3233/ISP-170134

Birk, L. (2019). Fundamentals of Ship Hydrodynamics (1ST ed.). New Jersey, USA: John Wiley & Sons, Ltd.

Gaggero, S., Villa, D., & Viviani, M. (2015). The KRISO Container Ship (KCS) Test Case: An Open-Source Overview. Proceedings of VI International Conference on Computational Methods in Marine Engineering (MARINE 2015), Rome, Italy, 735−749.

Go, J.S., Yoon, H.S., & Jung, J.H. (2017). Effects of a Duct Before a Propeller on Propulsion Performance. Ocean Engineering, 136, 54-66. https://doi.org/10.1016/j.oceaneng.2017.03.012

Henrich, S., & Yan, X.-K. (2017). On the Working Principle of Pre-Swirl Stators and on Their Application Benefit and Design Targets. International Shipbuilding Progress, 63(3−4), 87−107. https://doi.org/10.3233/ISP-170124

Hino, T. (2005), Proceedings of CFD Workshop Tokyo 2005. NMRI report 2005.

Kim, K.S., Kim, Y.C., Kim, J., Lee, Y.Y., Ahn, H., S., Yim, G.T., ... Van, S.H. (2013). Practical Application of CFD for Design of Energy Saving Devices Mounted on Ship stern. Proceedings of Twenty-third International Offshore and Polar Engineering Conference, Anchorage, Alaska.

Koushan, K., Krasilnikov, V., Nataletti, M., Sileo, L., & Spence, S. (2020). Experimental and Numerical Study of Pre-Swirl Stators PSS. Journal Marine Science Engineering, 8(1), 47. https://doi.org/10.3390/jmse8010047

Krol, P., & Tesch, K. (2018). Pre-Swirl Energy Saving Device in Marine Application. Journal of Physics: Conference Series, 1101, 012015. https://doi.org/10.1088/1742-6596/1101/1/012015

Larsson, L., Stern, F., Visonneau, M., Hirata, N., Hino, T., Kim, J. (Eds.). (2015). Tokyo 2015: A Workshop on CFD in Ship Hydrodynamics. 2, Tokyo, Japan: National Maritime Research Institute (NMRI).

Menter, F.R. (1993). Zonal Two Equations k-w Turbulence Models for Aerodynamics Flows. In 23rd Fluid Dynamics, Plasmadynamics, and Lasers Conference, American Institute of Aeronautics and Astronautics, Orlando, USA, AIAA-93-2906. https://doi.org/10.2514/6.1993-2906

Mewis, F., & Guiard, T. (2011). Mewis Duct - New Developments, Solutions, and Conclusions. Proceedings of Second International Symposium on Marine Propulsors, Hamburg, Germany.

Park, S., Park, S.W., Rhee, S.H, Lee, S.B., Choi, J.-E., Kang, S.H. (2013). Investigation on the Wall Function Implementation for the Prediction of Ship Resistance. International Journal of Naval Architecture and Ocean Engineering, 5, 33−46. https://doi.org/10.2478/IJNAOE-2013-0116

Seb, B. (2017). Numerical Characterization of a Ship Propeller (Master Thesis). University of Zagreb, Zagreb, Croatia.

Seo, S., Park, S., & Koo, B. (2017). Effect of Wave Periods on Added Resistance and Motions of a Ship in Head Sea Simulations. Ocean Engineering, 137, 309−327. http://dx.doi.org/10.1016/j.oceaneng.2017.04.009

Shen, Z., Carrica P.M., & Wan, D. (2014). Ship Motions of KCS in Head Waves with Rotating Propeller Using Overset Grid Method. Proceedings of International Conference on Ocean, Offshore and Arctic Engineering, San Francisco, California, USA, OMAE2014-23657, V002T08A043. https://doi.org/10.1115/OMAE2014-23657

van Leer, B. (1979). Towards the Ultimate Conservative Difference Scheme. V. A Second-order Sequel to Godunov's Method. Journal of Computational Physics, 32(1), 101−136. https://doi.org/10.1016/0021-9991(79)90145-1

Author ORCIDs

Author name	ORCID
Ng'aru, Joseph Mwangi	0000-0002-9704-6042
Park, Sunho	0000-0002-0388-2198
Hyun, Beom Soo	0000-0003-4951-6991

KSOE

Journal of Ocean Engineering and Technology 35(4), 257-265, August, 2021
https://doi.org/10.26748/KSOE.2021.014

pISSN 1225-0767
eISSN 2287-6715

Original Research Article

Development of Empirical Formulas for Approximate Spectral Moment Based on Rain-Flow Counting Stress-Range Distribution

Seockhee Jun[1] and Jun-Bum Park[2]

[1]*Team Leader, Floating PV Team, Saemangeum Business Division, Hyundai Global Co., Ltd., Gunsan, Korea*
[2]*Professor, Division of Navigation Science, Korea Maritime and Ocean University, Busan, Korea*

KEY WORDS: Approximate spectral moments, Rain-flow counting distribution, Step-by-step studies, Special parameters, Exponential bandwidth parameters

ABSTRACT: *Many studies have been performed to predict a reliable and accurate stress-range distribution and fatigue damage regarding the Gaussian wide-band stress response due to multi-peak waves and multiple dynamic loads. So far, most of the approximation models provide slightly inaccurate results in comparison with the rain-flow counting method as an exact solution. A step-by-step study was carried out to develop new approximate spectral moments that are close to the rain-flow counting moment, which can be used for the development of a fatigue damage model. Using the special parameters and bandwidth parameters, four kinds of parameter-based combinations were constructed and estimated using the R-squared values from regression analysis. Based on the results, four candidate empirical formulas were determined and compared with the rain-flow counting moment, probability density function, and root mean square (RMS) value for relative distance. The new approximate spectral moments were finally decided through comparison studies of eight response spectra. The new spectral moments presented in this study could play an important role in improving the accuracy of fatigue damage model development. The present study shows that the new approximate moment is a very important variable for the enhancement of Gaussian wide-band fatigue damage assessment.*

1. Introduction

Much research has been performed continuously to fit a stress-range distribution and to predict fatigue damage for a Gaussian wide-band stress response. As a result, approximation models based on an empirical correction factor or numerical simulation have been proposed to solve wide-band spectrum issues. However, they still yield overestimated or underestimated fatigue damages when compared to time-domain rain-flow counting analysis.

The DNV rule (DNV, 2010) recommends cycle counting, an empirical model, and an analytic model for the Gaussian wide-band stress spectrum to carry out spectral fatigue analysis. The rain-flow counting method is mainly used for cycle counting. The Wirsching-Light correction method (Wirsching and Light, 1980), Dirlik model (Dirlik, 1985), and Single Moment method (Larsen and Lutes, 1991) were suggested as empirical models. The analytic model presents the Jiao-Moan model (Jiao and Moan, 1990) whichcan be applied to a narrow-band bi-modal distribution. Lloyd's rule (LR, 2018) recommends a multi-peak short-term spectral calculation method proposed by Park et al. (2014) and Dirlik (1985) in fatigue analysis for dynamic responses such as springing or whipping.

A probability density function (PDF) for the Gaussian wide-band stress spectrum has not been defined theoretically. Instead, several efforts to develop an approximation formula that follows a numerical simulation-based rain-flow counting stress distribution have been carried out (Rychlik, 1987; Zhao and Baker, 1992). Larsen and Lutes (1991) developed The Single Moment model that is applicable to a wide-band spectrum. This model considers the generalized $2/m$-order spectral moment using the slope m of the S-N curve. However, since it cannot reflect the interaction between low-frequency and high-frequency modes, the accuracy of fatigue damage is low.

Recently, a mathematical re-interpretation of a Single Moment model was attempted using a projection by projection (PbP) approach, which is called a nonlinear coupling rule (Benasciutti et al., 2013). This method discretizes a wide-band stress response spectrum into a myriad of small bands. Assuming that each small band is an independent narrow band for the frequency domain, it estimates cumulative fatigue damage using the spectral discretization method

Received 15 March 2021, revised 4 May 2021, accepted 6 July 2021
Corresponding author Jun-Bum Park: +82-51-410-4233, jbpark@kmou.ac.kr

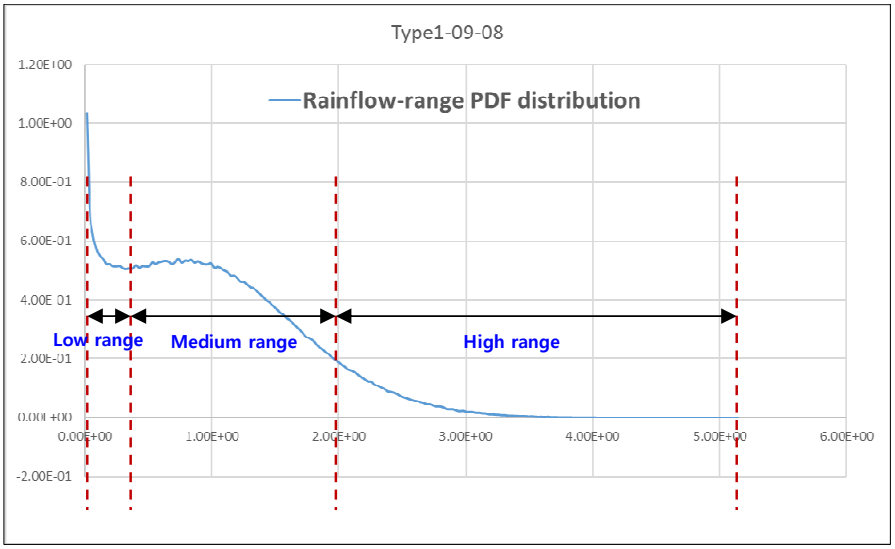

Fig. 1 Stress-range categories in the rain-flow counting distribution

and Rayleigh PDF. Gao and Zheng (2019) derived a quadratic coupling method with three variables through numerical simulation and rain-flow counting to solve the inaccuracy of a bi-modal spectrum sincethe Single Moment model overlooks the interaction between low-frequency and high-frequency modes. Zheng et al. (2020) extended the bi-modal process to a tri-modal process based on a discrete spectral method and coupling coefficient equation.

Research results have recently shown that the accuracy of fatigue damage prediction for a numerical simulation-based approximate empirical model is relatively low. Research works for bi-modal or tri-modal spectra have been actively carried out for the development of a new method. For the Dirlik, Benasciutti, and Park models, associated research for numerical simulation-based approximations has been sluggish for a long time. For this reason, we attempted to develop empirical formulas by adopting new approximate spectral moments to improve the accuracy of prediction of the stress-range distribution and fatigue damages for a wide-band spectrum through analysis of other research, which can be easily applied to actual project engineering.

Fig. 1 shows an example of the rain-flow counting stress-range distribution for a Gaussian wide-band spectrum. As shown in the figure, the stress range is categorized into a low range, medium range, and high range. To enhance the accuracy of fatigue damage assessment, it is necessary to reflect the characteristics of the rain-flow counting distribution very well. First of all, it is necessary to determine the approximate spectral moment that is close to the simulation-based rain-flow counting moment. The new approximate spectral moment is highly important because it is considered as the input variable in the constitutive equation of the fatigue model. So far, no research has been published that defines the rain-flow counting moment as a theoretical solution. From the results of recent research, the rain-flow counting moment is defined as the spectral moment or bandwidth parameter, but it can be seen that there is a limit to increasing the accuracy of fatigue damage.

We developed an empirical formula for an approximate spectral moment that is close to the rain-flow counting stress range ($\triangle\sigma$) distribution. This paper describes the detailed development process and calculation procedure of the step-by-step study and comparison of several candidate formulas. In addition, a special parameter or exponential special parameter and two exponential bandwidth parameters are introduced and are combined to develop approximate spectral moments. Fig. 2 shows the development flowchart of empirical formulas for the approximate spectral moments proposed in this study.

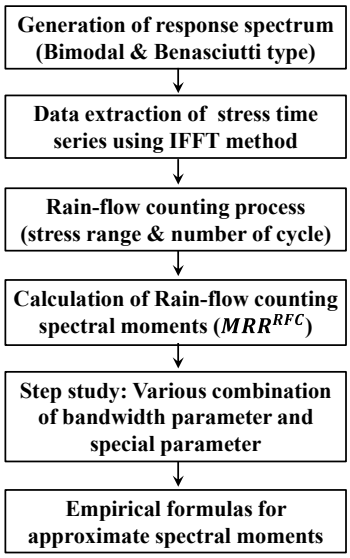

Fig. 2 Flowchart to develop empirical formulas for the approximate spectral moments

2. Data Processing

2.1 Generation of Response Spectrum

Data processing follows the same spectrum models and numerical calculation method as those specified by Park et al. (2014) as the

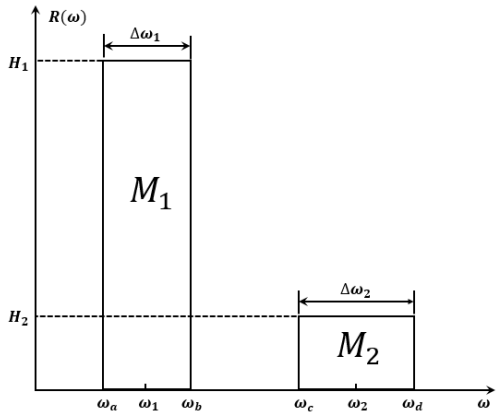

Fig. 3 Bi-modal spectrum for response generation

resultant outputs should be compared under the same input data conditions. Two representative spectra are selected to implement the stress response generation. Fig. 3 shows an ideal bi-modal spectrum proposed by Lutes and Larsen (1990). This spectrum has two peaks with low and high frequencies. Assuming that each spectrum is distributed in a narrow band, the variance is made to be 1,000 and 500 (Park et al., 2014). The spectrum area ratio A_r and frequency ratio F_r are:

$$A_r = \frac{M_2}{M_1} = \frac{H_2(\omega_d - \omega_c)}{H_1(\omega_b - \omega_a)}, \quad F_r = \frac{\omega_c}{\omega_a} = \frac{\omega_d}{\omega_b} \tag{1}$$

Fig. 4 shows the five spectra proposed by Benasciutti (2004) (i.e., constant, linear, double symmetrical, and two kinds of anti-symmetric parabolic). Several assumptions are required to generate a stress response spectrum. The 0-order spectral moment (or variance) of all spectra is 1,000, and two bandwidth parameters α_1 and α_2 are within the range of 0.2−0.9 and 0.1−0.8, respectively (Park et al., 2014). The spectral bandwidth parameter α_n and the *n*th order spectral moment m_n are defined as follows.

$$\alpha_n = \frac{m_n}{\sqrt{m_0 m_{2n}}} \tag{2}$$

$$m_n = \int_0^\infty \omega^n S_a(\omega) d\omega \tag{3}$$

where ω = Wave frequency

$S_a(\omega)$ = Response spectrum of stress amplitude a

Since the stress response spectrum is assumed to be a dimensionless quantity, the resulting stresses become a dimensionless quantity.

2.2 Data Extraction of Stress Time History

Time history data from the stress response is extracted using the Inverse fast Fourier transform (IFFT) method as follows:

$$\sigma(t) = \sum_{i=1}^{n} \sqrt{2R(\omega_i)\Delta\omega_i} \cos(\omega_i t + \phi_i) \tag{4}$$

where, $\Delta\omega_i = \omega_i - \omega_{i-1}$, $\omega_i = \frac{\omega_i + \omega_{i-1}}{2}$

where $R(\omega_i)$ is the response spectrum, ω_i is the angular frequency, ϕ_i is the phase angle, t is time, and n is the number of frequencies. The angular frequency and phase angle are generated by a random number giving an equal distribution within the allowable range. In the process of extracting the time history of stress data, the stresses with the shortest period should be taken into account so as not to miss them. Therefore, it is important to select a reasonable and appropriate time increment in order to accurately capture the maximum and minimum of the stress during the IFFT process.

Fig. 5 shows the numerical procedure for extracting time history data as described in Park et al., (2014). Through this process, it is possible to obtain random time history data with a sufficiently long

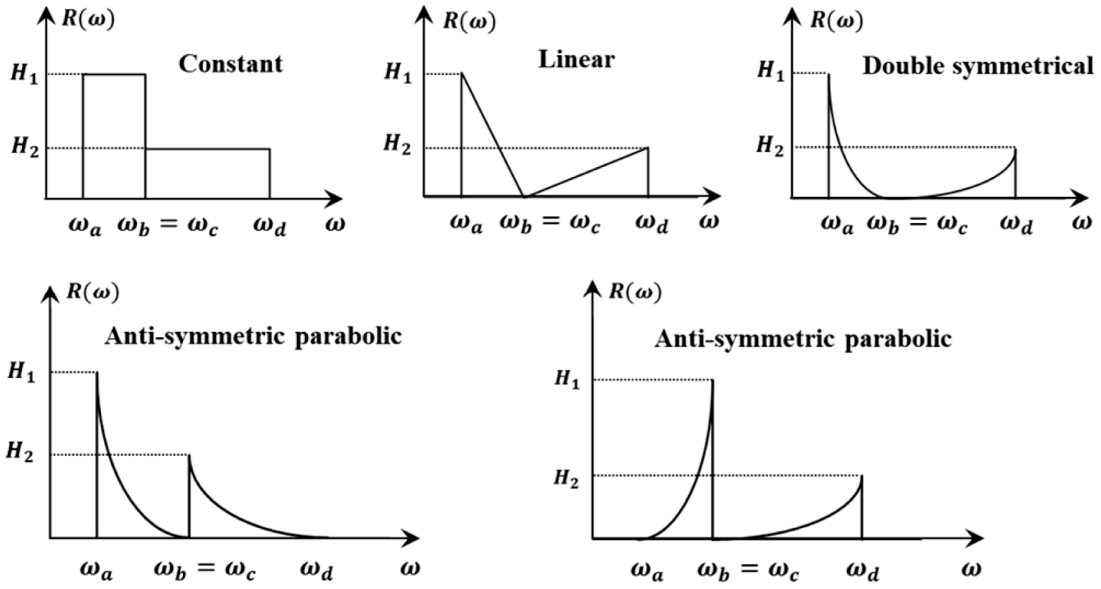

Fig. 4 Benasciutti spectrum for response generation

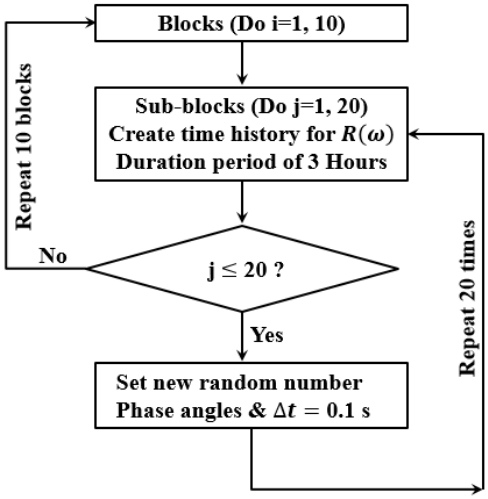

Fig. 5 Numerical simulation flowchart for time history data generation

period in the time domain. In the simulation, 10 blocks are repeatedly considered, and 20 sub-blocks are iteratively processed in one block. The duration period is 3 hours, and the phase angle and frequency interval are set randomly as the sub-block changes.

2.3 Rain-Flow Counting Process

To calculate the stress range and number of cycles from the time history data, we considered the rain-flow counting process according to the standard procedure described in ASTM E1049-85 (ASME, 2005). The PDF can be obtained by performing a rain-flow counting process for the stress range and number of cycles calculated from each block, as shown in Fig. 5. Finally, the PDF is obtained by taking the average of the PDF of 10 blocks.

3. Step Study of Approximate Spectral Moment

3.1 Definition of Rain-Flow Counting Moment

To increase the accuracy of fatigue damage calculation, an approximate PDF with the same distribution as the rain-flow counting PDF must be obtained. For this purpose, it is preferable to obtain the rain-flow counting moment (MRR^{RFC}) through numerical simulation and then to obtain an approximate spectral moment that is close to the rain-flow counting moment. For the response spectrum, the rain-flow counting moment is defined as follows (Dirlik, 1985):

$$MRR^{RFC}(q) = \frac{\int_0^\infty \Delta\sigma^q \, P^{RFC}(\Delta\sigma) d\Delta\sigma}{\int_0^\infty \Delta\sigma^q \, \Delta\sigma \exp\left(-\frac{\Delta\sigma^2}{2}\right) d\Delta\sigma} \tag{5}$$

As can be seen from the equation above, the rain-flow counting moment is a non-dimensional value of the rain-flow counting PDF from a standard Rayleigh PDF. ExistingFatigue models define the rain-flow counting moment using spectral moments or bandwidth parameters (Dirlik, 1985; Park et al., 2014). From the results of recent studies, it can be seen that there is a limit to increasing the accuracy of fatigue damage. In this regard, it is necessary to develop new empirical formulas for approximate spectral moments. If approximate spectral moments can be accurately and efficiently obtained, a stress-range distribution close to the exact value can be obtained, and the accuracy of the fatigue damage prediction can be dramatically improved.

3.2 Existing Approximate Spectral Moment

Dirlik (1985) and Park et al. (2014) presented approximate spectral moments as a combination of bandwidth parameters through a parametric study based on numerical simulation. The first and second-order approximate spectral moments presented by Dirlik (1985) are as follows.

$$MRR_{DK}^{APP}(1) = \alpha_2 \tag{6}$$

$$MRR_{DK}^{APP}(2) = \alpha_1 \alpha_2 \tag{7}$$

where, $\alpha_1 = \frac{m_1}{\sqrt{m_0 m_2}}$, $\alpha_2 = \frac{m_2}{\sqrt{m_0 m_4}}$

The approximate spectral moment suggested by Park et al. (2014) is as follows.

$$MRR_{PK}^{APP}(1) = \alpha_2 \tag{8}$$

$$MRR_{PK}^{APP}(2) = \alpha_{0.95} \alpha_{1.97} \tag{9}$$

$$MRR_{PK}^{APP}(3) = \alpha_{0.54} \alpha_{0.93} \alpha_{1.97} \tag{10}$$

where $\alpha_{0.54} = \frac{m_{0.54}}{\sqrt{m_0 m_{1.08}}}$, $\alpha_{0.93} = \frac{m_{0.93}}{\sqrt{m_0 m_{1.86}}}$

$$\alpha_{0.95} = \frac{m_{0.95}}{\sqrt{m_0 m_{1.9}}}, \alpha_{1.97} = \frac{m_{1.97}}{\sqrt{m_0 m_{3.94}}}$$

Approximate spectral moments have been presented up to the third-order term, and no research has been published for fourth-order or higher terms. Increasing the order of the approximate spectral moment greatly contributes to the accuracy of the stress distribution in the high stress range where the Vanmarcke parameter (Vanmarcke, 1972) is close to 1.0, and eventually, the accuracy of the fatigue damage estimation can be increased. Therefore, several step-by-step studies need to be carried out to develop approximate spectral moments that are close to the rain-flow counting moment.

3.3 Step 1: Combination of Bandwidth Parameter

For the purpose of simply defining the approximate spectral moment so that it can be applied to the actual design, a combination with the constants b and c in the bandwidth parameter is assumed as follows.

$$MRR_{BND}^{APP}(q) = \alpha_1^b \, \alpha_2^c \tag{11}$$

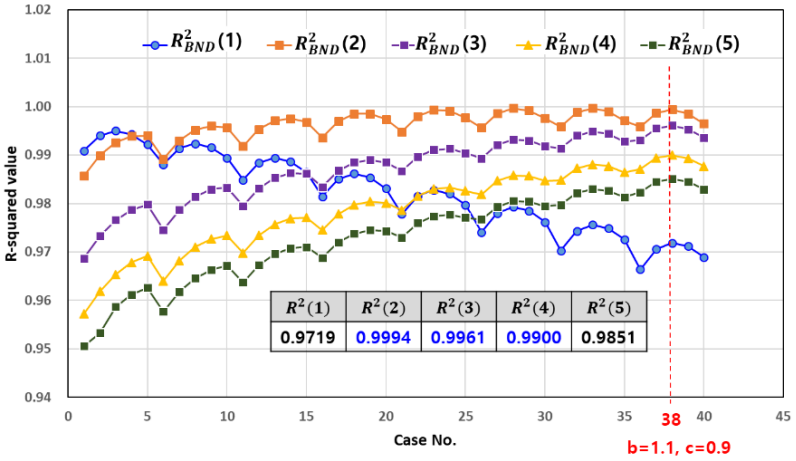

Fig. 6 R-squared value distribution between $MRR^{RFC}(q)$ and $MRR^{APP}_{BND}(q)$

To find the optimal values of b and c using the bandwidth parameter, the range of exponents is determined while excluding the range of low accuracy of the R-squared values through parametric studies:

$$b = 0.4 \text{ to } 1.1, \text{ interval of } 0.1 \tag{12}$$

$$c = 0.7 \text{ to } 1.1, \text{ interval of } 0.1 \tag{13}$$

Regression analysis is performed for 40 cases using $MRR^{RFC}(q)$ obtained from numerical simulation. To show the difference between $MRR^{RFC}(q)$ and $MRR^{APP}_{BND}(q)$, the R-squared values are calculated, and the result is shown in Fig. 6. The case where the R-squared values between two moments are close to 1.0 is case no. 38, and the corresponding exponent values are determined as 1.1 and 0.9, respectively. Therefore, $MRR^{APP}_{BND}(q)$ is determined as follows.

$$MRR^{APP}_{BND}(q) = \alpha_1^{1.1}\,\alpha_2^{0.9} \tag{14}$$

From the R-squared values in Fig. 6, the accuracy of the remaining spectral moments except for both the first and fifth-order spectral moments is above 99%. As the constants b and c increase, the R-squared values of the first spectral moment gradually decrease. On the other hand, the R-squared values of the remaining spectral moment increase until b is 1.1 and c is 0.9. However, it decreases after that. As for the first-order spectral moment, it can be seen that the R-squared value is maximized when b is 0.4 and c is 0.9.

3.4 Step 2: Combination of Special Parameter

Since there is a limit to obtaining the moment equivalent to the $MRR^{RFC}(q)$ by combining only the bandwidth parameters, a special parameter was used (Jun and Park, 2020):

$$\mu_k = \frac{m_{(k+0.01)}}{\sqrt{m_{0.01}\,m_{(2k+0.01)}}} \tag{15}$$

where, m = spectral moment

k = 0.01 to 2.5, 0.01 interval

The range of coefficient k is considered the same as the range of bandwidth parameter α_k. An iterative numerical calculation is performed in consideration of the following three conditions, and the R-squared values are confirmed through regression analysis between the special parameter and $MRR^{RFC}(q)$ using the rain-flow counting moment obtained from the numerical simulation. In this study, the moment $MRR^{APP}_{SPE}(q)$ up to the fourth-order term is defined using a linear combination of special parameters as follows:

$$MRR^{APP}_{SPE}(1) = \mu_{0.12}\,\mu_{1.99} \tag{16}$$

$$MRR^{APP}_{SPE}(2) = \mu_{0.93}\,\mu_{1.96} \tag{17}$$

$$MRR^{APP}_{SPE}(3) = \mu_{0.57}\,\mu_{0.84}\,\mu_{1.96} \tag{18}$$

$$MRR^{APP}_{SPE}(4) = \mu_{0.57}\,\mu_{0.57}\,\mu_{0.63}\,\mu_{1.97} \tag{19}$$

Table 1 shows the R-squared distribution between $MRR^{APP}_{SPE}(q)$ and $MRR^{RFC}(q)$. As shown in the table, excluding the fifth spectral moment, the accuracy of the remaining spectral moments is 99.7% or more. From this result, it is confirmed that the consideration of the special parameter is very appropriate to obtain the approximate spectral moment. However, as the order of the spectral moment is increased, the simple combination formula of the special parameter becomes complicated, so it is difficult to apply it to the actual design.

Table 1 R-squared values between $MRR^{APP}_{SPE}(q)$ and $MRR^{RFC}(q)$

$R^2_\mu(1)$	$R^2_\mu(2)$	$R^2_\mu(3)$	$R^2_\mu(4)$	$R^2_\mu(5)$
1.0000	0.9997	0.9990	0.9970	0.9940

3.5 Step 3: Combination of a Special Parameter and Exponential Bandwidth Parameters

The approximate moment $MRR^{APP}_{CS1}(q)$ is determined by combining a special parameter μ_k and spectral moment $MRR^{APP}_{BND}(q)$ from Eq. (14) as follows.

$$MRR_{CS1}^{APP}(q) = \mu_k \, \alpha_1^{1.1} \, \alpha_2^{0.9} \tag{20}$$

Using $MRR^{RFC}(q)$ obtained from the numerical simulation, the R-squared values between $MRR^{RFC}(q)$ and $MRR_{CS1}^{APP}(q)$ are calculated through regression analysis for 24 cases, and the results are shown in Fig. 7.

In the case of the 1st and 2nd-order spectral moment, the maximum R-squared values are shown when the coefficient k is 0.01. As the coefficient k increases, the R-squared values of the spectral moment decrease. This means that it is more advantageous not to consider the special parameter for the 1st and 2nd-order spectral moments. When the coefficient k is 0.6, the R-squared values of the remaining spectral moments show the maximum values and give more accurate results than the approximate spectral moment $MRR_{BND}^{APP}(q)$ of step 1. When k is greater than 0.6, the R-squared values tend to decrease. From the results of step 3, the approximate spectral moments are summarized below:

$$MRR_{CS1}^{APP}(q) = \alpha_1^{1.1} \, \alpha_2^{0.9} \quad \text{for} \quad q = 1 - 2 \tag{21}$$

$$MRR_{CS1}^{APP}(q) = \mu_{0.6} \, \alpha_1^{1.1} \, \alpha_2^{0.9} \quad \text{for} \quad q = 3 - 5 \tag{22}$$

3.6 Step 4: Combination of an Exponential Special Parameter and Exponential Bandwidth Parameters

The approximate moment $MRR_{CS2}^{APP}(n)$ is determined by combining an exponential special parameter μ_1^a and approximate spectral moment $MRR_{BND}^{APP}(n)$ of step 1 as follows.

$$MRR_{CS2}^{APP}(q) = \mu_1^a \, \alpha_1^{1.1} \, \alpha_2^{0.9} \tag{23}$$

where, $\mu_1 = \dfrac{m_{1.01}}{\sqrt{m_{0.01} \, m_{2.01}}}$

For the purpose of finding the optimal value of the exponent a of the special parameter, the final range below is determined while excluding

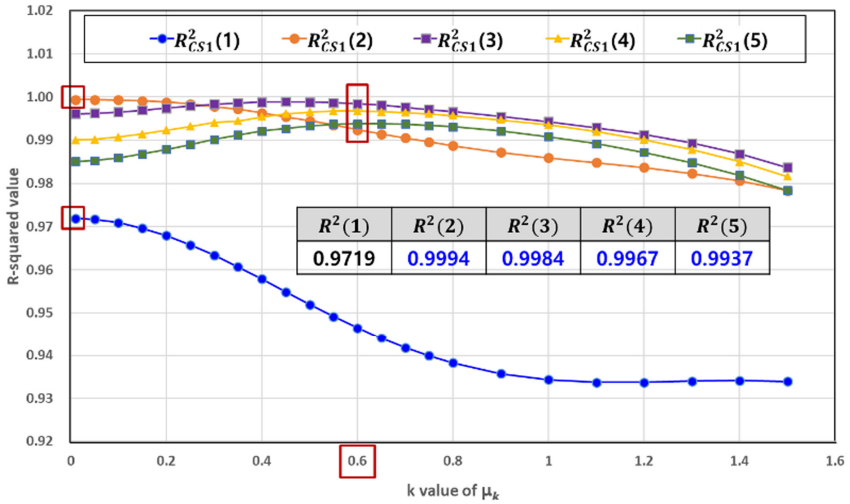

Fig. 7 R-squared value distribution between $MRR^{RFC}(q)$ and $MRR_{CS1}^{APP}(q)$

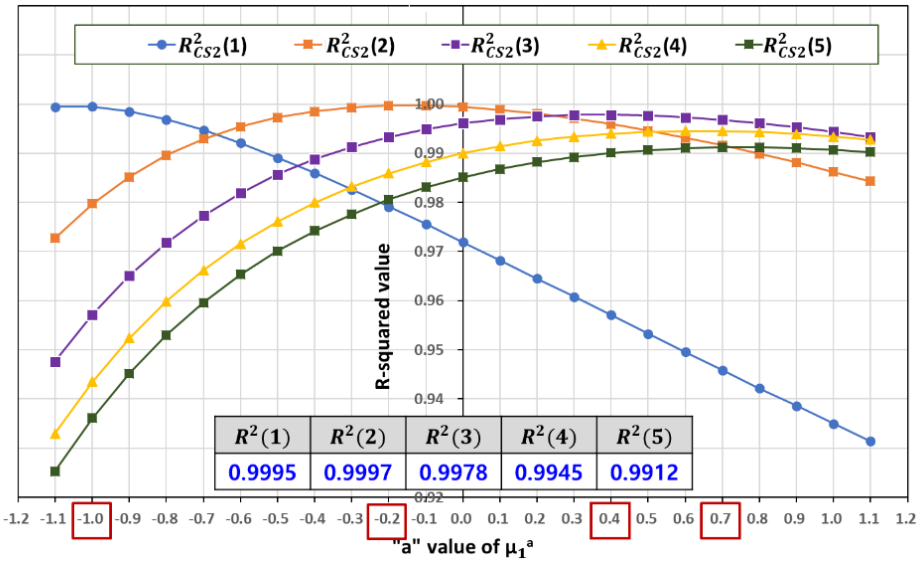

Fig. 8 R-squared value distribution between $MRR^{RFC}(q)$ and $MRR_{CS2}^{APP}(q)$

the range with low accuracy of the R-squared values through a parametric study:

$$a = \text{-1.1 to 1.1, 0.1 interval} \tag{24}$$

Using the $MRR^{RFC}(q)$ obtained from the numerical simulation, the R-squared values that show the difference between $MRR^{RFC}(q)$ and $MRR_{CS2}^{APP}(q)$ are calculated through regression analysis for 23 cases. The results are shown in Fig. 8 and are summarized below:

$$MRR_{CS2}^{APP}(1) = \mu_1^{-1.0}\,\alpha_1^{1.1}\,\alpha_2^{0.9} \tag{25}$$

$$MRR_{CS2}^{APP}(2) = \mu_1^{-0.2}\,\alpha_1^{1.1}\,\alpha_2^{0.9} \tag{26}$$

$$MRR_{CS2}^{APP}(3) = \mu_1^{0.4}\,\alpha_1^{1.1}\,\alpha_2^{0.9} \tag{27}$$

$$MRR_{CS2}^{APP}(4) = \mu_1^{0.7}\,\alpha_1^{1.1}\,\alpha_2^{0.9} \tag{28}$$

$$MRR_{CS2}^{APP}(5) = \mu_1^{0.7}\,\alpha_1^{1.1}\,\alpha_2^{0.9} \tag{29}$$

From the R-squared values in Fig. 8, it can be found that the accuracy of the remaining spectral moments except for both the fourth-order and the fifth-order spectral moments is above 99.7%. As the exponent a increases, the R-squared values of the first spectral moment decrease. On the other hand, the R-squared values of the remaining spectral moment show a tendency of increasing as the exponent a increases and then decreasing as it passes a specific value. As for the spectral moments from the first-order to the fifth-order, it can be seen that the R-squared value is maximized when the exponent a is -1.0, -0.2, 0.4, and 0.7.

4. Comparison

4.1 Four Candidate Formulas

Based on the results obtained from the step-by-step study in the previous section, the rain-flow counting moment $MRR^{RFC}(q)$ and the highest equivalent approximate moment $MRR_{NEW}^{APP}(q)$ are calculated. Several parametric studies were carried out using the best data fitting method and regression analysis. As a result, four final candidate empirical formulas were chosen, as illustrated in Table 2.

Table 2 Four candidate formulas for approximate spectral moments

	MRR(1)	MRR(2)	MRR(3)	MRR(4)
Formula #1	$\mu_1^{-1.0}\,\alpha_1^{1.1}\,\alpha_2^{0.9}$	$\mu_1^{-0.2}\,\alpha_1^{1.1}\,\alpha_2^{0.9}$	$\mu_{0.6}\,\alpha_1^{1.1}\,\alpha_2^{0.9}$	$\mu_{0.6}\,\alpha_1^{1.1}\,\alpha_2^{0.9}$
Formula #2	$\mu_1^{-0.96}\,\alpha_1^{1.1}\,\alpha_2^{0.9}$	$\mu_1^{-0.02}\,\alpha_1^{1.1}\,\alpha_2^{0.9}$	$\mu_{0.52}\,\alpha_1^{1.1}\,\alpha_2^{0.9}$	$\mu_{0.55}\,\alpha_1^{1.1}\,\alpha_2^{0.9}$
Formula #3	$\mu_1^{-0.31}\,\alpha_1^{0.4}\,\alpha_2^{0.9}$	$\mu_1^{0.1}\,\alpha_1^{0.9}\,\alpha_2^{0.9}$	$\mu_{0.52}\,\alpha_1^{1.1}\,\alpha_2^{0.9}$	$\mu_{0.55}\,\alpha_1^{0.4}\,\alpha_2^{0.9}$
Formula #4	$\mu_1^{-0.26}\,\alpha_1^{0.4}\,\alpha_2^{0.9}$	$\mu_1^{0.18}\,\alpha_1^{0.9}\,\alpha_2^{0.9}$	$\mu_{0.52}\,\alpha_1^{1.1}\,\alpha_2^{0.9}$	$\mu_{0.55}\,\alpha_1^{0.4}\,\alpha_2^{0.9}$

4.2 Comparison of Candidate Formulas

The rain-flow counting response distribution calculated from the numerical simulation is regarded as the real value. Several comparison studies were carried out using four empirical equations. Table 3 shows the comparison results of R-squared values between the rain-flow counting moment and approximate spectral moment using four formulas. Fig. 9 shows a comparison of the PDF between empirical formula #2 and the rain-flow counting spectral moment for two representative spectra mentioned in section 2.1.

Fig. 10 shows the comparison of the relative distance from rain-flow counting distribution of four formulas compared with two models (Dirlik model and Park model) to confirm the suitability and accuracy.

Table 3 Comparison of R-squared values using four formulas

Candidate Formula	MRR(1)	MRR(2)	MRR(3)	MRR(4)
Formula #1	0.9995	0.9997	0.9984	0.9967
Formula #2	0.9992	0.9995	0.9988	0.9966
Formula #3	0.9996	0.9997	0.9988	0.9966
Formula #4	0.9993	0.9995	0.9988	0.9966

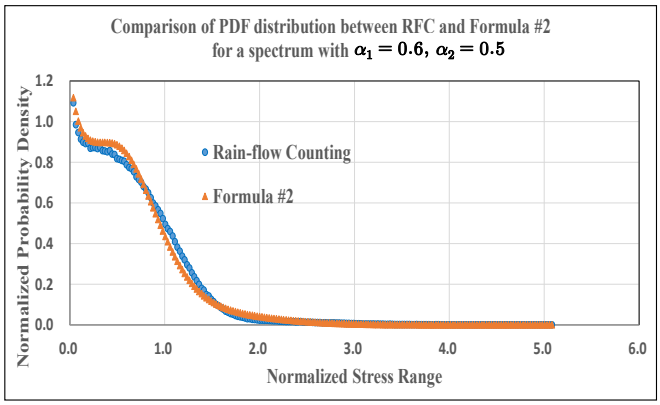

(a) $\alpha_1 = 0.6$, $\alpha_2 = 0.5$

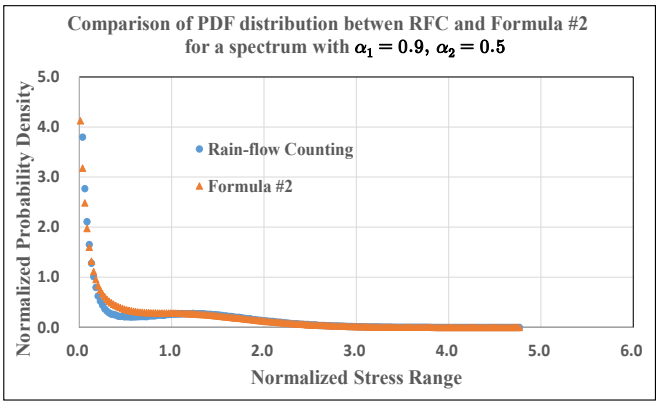

(b) $\alpha_1 = 0.9$, $\alpha_2 = 0.5$

Fig. 9 Comparison of PDF between empirical formula #2 and rain-flow counting moment.

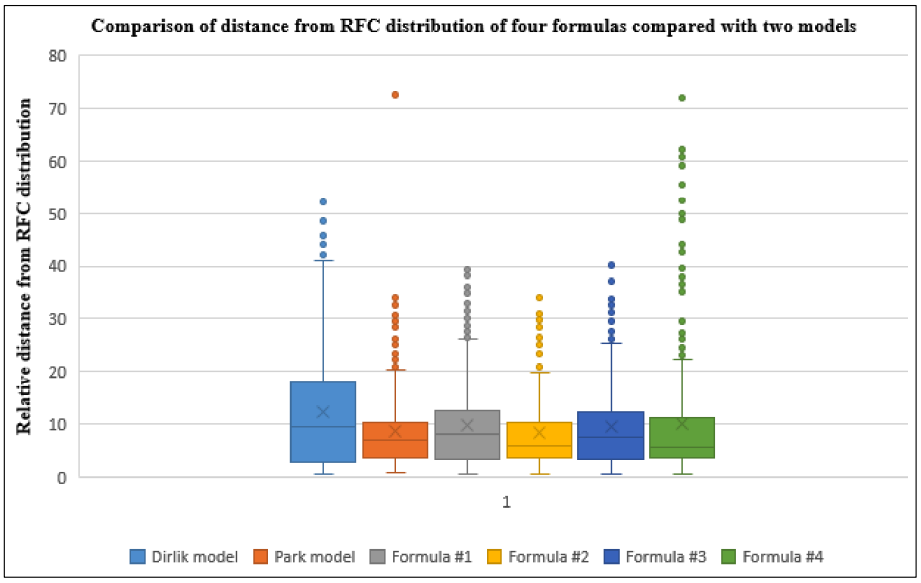

Fig. 10 Comparison of distance from RFC distribution of four formulas compared and two other models

To evaluate the error rates for relative distance, the root mean square (RMS) method was used as shown in Eq. (30).

$$\text{RMS average} = \sqrt{\frac{\Sigma X_i^2}{N}} \tag{30}$$

where, X_i = Relative distance error of i^{th} spectrum

N = Total number of spectra

Table 4 shows a quantitative comparison of distance between the two models and four formulas using the RMS method. As a result, it was confirmed that formula #2 gives the closest distribution to the rain-flow counting distribution.

Table 5 summarizes the comparison results based on the PDF distribution and relative distance error rate between the rain-flow counting distribution and four formulas using eight spectra. By extending to the fourth-order spectral moment that the other model did not consider, the contribution to the rain-flow counting (RFC) distribution in the high range is large, and the fatigue damage accuracy can be improved. The approximate spectral moments obtained from this study can be applied as significant input variables in the constitutive equation of the fatigue model.

Table 4 Comparison of RMS values for relative distance error between existing models and four formulas

	Dirlik model	Park model	Formula #1	Formula #2	Formula #3	Formula #4
RMS value	16.92	12.01	12.88	**11.60**	12.61	16.01

Table 5 Comparison of four formulas using eight spectra

Spectrum	Formula #1	Formula #2	Formula #3	Formula #4
Type1-02-01	Good	**Good**	Good	Good
Type1-05-01	Good	**Good**	Good	Good
Type1-06-05	Bad	**Better**	Bad	Good
Type1-07-06	Good	**Better**	Good	Good
Type1-09-05	Good	**Good**	Good	Good
Type1-09-08	Good	**Good**	Good	Good
Type2-04-03	Bad	**Good**	Bad	Good
Type5-09-08	Good	**Good**	Good	Good

5. Conclusions

From the results of previous studies, when increasing the order of the spectral moment, the PDF distribution in the Gaussian wide-band range close to a Vanmarcke parameter of 1.0 approaches the rain-flow counting distribution, so the accuracy of the fatigue damage assessment can be improved. In this study, we developed a new approximate spectral moment $MRR_{NEW}^{APP}(q)$ that is close to the rain-flow counting distribution by combining special parameters, exponential special parameters, and exponential bandwidth parameters through step-by-step studies using regression analysis. In addition, this paper deals with the full explanation on the basis of study, i.e. detailed development process and calculation procedure of the step-by-step study and comparison study of several candidate formulas, of the approximate spectral moment. Using two representative spectrums such as Benasciutti spectrum and bi-modal spectrum, preliminary data processes, i.e. response spectrum generation, time history data extraction and rain-flow counting execution, were performed to make necessary input data for the development of new approximate spectral moments. The main characteristics of this study that differentiate it from other studies are as follows.

(1) Whereas other studies considered only the 2^{nd} or 3^{rd}-order approximate spectral moments, this study contributed to increasing the accuracy of fatigue damage assessment by extending them to 4^{th}–order terms or higher.

(2) The previous models considered the approximate spectral moment with the spectral moment $m_0 - m_4$ or the linear combination of the bandwidth parameters α_1 and α_2. In this study, a special parameter or exponential special parameter was combined with the bandwidth parameter through a step-by-step study to develop several empirical formulas.

(3) In addition, simplicity and convenience were considered for an actual engineering application, and stability and accuracy of the fatigue analysis solution can be enhanced by applying approximate spectral moments with the R-squared values of more than 97% comparing with rain-flow counting moments.

Funding

This research was supported by the BB21 plus funded by Busan Metropolitan City and Busan Institute for Talent & Lifelong Education (BIT)

References

American Society for Testing and Materials (ASTM). (2005). Standard Practices for Cycle Counting in Fatigue Analysis (ASTM E1049-85).

Benasciutti, D. (2004). Fatigue Analysis of Random Loadings (PhD Thesis). University of Ferrara.

Benasciutti, D., Cristofori, A., & Tovo, R. (2013). Analogies Between Spectral Methods and Multiaxial Criteria in Fatigue Damage Evaluation. Probabilistic Engineering Mechanics, 31, 39–45. https://doi.org/10.1016/j.probengmech.2012.12.002

Det Norske Veritas (DNV). (2010). Recommended Practice for Riser Fatigue (DNV-RP-F204: DNV).

Dirlik, T. (1985). Application of Computers in Fatigue (PhD Thesis). University of Warwick.

Gao, S., & Zheng, X.Y. (2019). An Improved Spectral Discretization Method for Fatigue Damage Assessment of Bimodal Gaussian Processes. International Journal of Fatigue, 119, 268–280. https://doi.org/10.1016/j.ijfatigue.2018.09.027

Jiao, G., & Moan, T. (1990). Probabilistic Analysis of Fatigue Due to Gaussian Load Processes. Probabilistic Engineering Mechanics, 5(2), 76–83. https://doi.org/10.1016/0266-8920(90)90010-H

Jun, S.H., & Park, J.B. (2020). Development of a Novel Fatigue Damage Model for Gaussian Wide Band Stress Responses Using Numerical Approximation Methods. International Journal of Naval Architecture and Ocean Engineering, 12, 755–767. https://doi.org/10.1016/j.ijnaoe.2020.09.005

Larsen, C.E., & Lutes, L.D. (1991). Predicting the Fatigue Life of Offshore Structures by the Single-Moment Spectral Method. Stochastic Structural Dynamics 2, 91–120. https://doi.org/10.1007/978-3-642-84534-5_7

Lloyd's Register (LR). (2018). Fatigue Assessment Including Hull Girder Springing. Global Design Loads of Container Ships and Other Ships Prone to Whipping and Springing, 45-51.

Lutes, L.D., & Larsen, C.E. (1990). Improved Spectral Method for Variable Amplitude Fatigue Prediction. Journal of Structural Engineering, 116(4), 1149–1164. https://doi.org/10.1061/(ASCE)0733-9445(1990)116:4(1149)

Park, J.B., Choung, J.M., & Kim, K.S. (2014). A New Fatigue Prediction Model for Marine Structures Subject to Wide Band Stress Process. Ocean Eng. 76, 144–151. https://doi.org/10.1016/j.oceaneng.2013.11.002

Rychlik, I. (1987). A New Definition of the Rainflow Cycle Counting Method. International Journal of Fatigue, 9(2), 119–121. https://doi.org/10.1016/0142-1123(87)90054-5

Vanmarcke, E.H. (1972). Properties of Spectral Moments with Applications to Random Vibration. Journal of the Engineering Mechanics Division, 98(2), 425–446. https://doi.org/10.1061/JMCEA3.0001593

Wirsching, P.H., & Light, M.C. (1980). Fatigue Under Wide Band Random Stresses. Journal of the Structural Division, 106(7), 1593–1607. https://doi.org/10.1061/JSDEAG.0005477

Zhao, W., & Baker, M.J. (1992). On the Probability Density Function of Rainflow Stress Range for Stationary Gaussian Processes International Journal of Fatigu, 14(2), 121–135. https://doi.org/10.1016/0142-1123(92)90088-T

Zheng, X.Y., Gao, S., & Huang, Y. (2020). Cross-mode Coupling for the Fatigue Damage Evaluation of Trimodal Gaussian Processes. Ocean Engineering, 202, 107177. https://doi.org/10.1016/j.oceaneng.2020.107177

Author ORCIDs

Author name	ORCID
Jun, Seockhee	0000-0001-6104-9973
Park, Jun-bum	0000-0003-1030-9338

KSOE

Journal of Ocean Engineering and Technology 35(4), 266-272, August, 2021
https://doi.org/10.26748/KSOE.2021.009

pISSN 1225-0767
eISSN 2287-6715

Original Research Article

A Study of 100 tonf Tensile Load for SMART Mooring Line Monitoring System Considering Polymer Fiber Creep Characteristics

Joseph Chul Chung[1], Michael Myung-Sub Lee[2] and Sung Ho Kang[3]

[1]*Department of R&D manager, IT convergence Laboratory, CyTroniQ Co. Ltd., Cheon-an, South Korea*
[2]*General manager, Dept. of Businesses, CyTroniQ Co. Ltd., Cheon-an, South Korea*
[3]*Researcher, IT convergence Laboratory, CyTroniQ Co. Ltd., Cheon-an, South Korea*

KEY WORDS: Creep, SMART (Smart Mooring and Riser Truncation) mooring line, Tensile load, Monitoring

ABSTRACT: *Mooring systems are among the most important elements employed to control the motion of floating offshore structures on the sea. Considering the use of polymer material, a new method is proposed to address the creep characteristics rather than the method of using a tension load cell for measuring the tension of the mooring line. This study uses a synthetic mooring rope made from a polymer material, which usually consists of three parts: center, eye, and splice, and which makes a joint for two successive ropes. We integrate the optical sensor into the synthetic mooring ropes to measure the rope tension. The different structure of the mooring line in the longitudinal direction can be used to measure the loads with the entire mooring configuration in series, which can be defined as SMART (Smart Mooring and Riser Truncation) mooring. To determine the characteristics of the basic SMART mooring, a SMART mooring with a diameter of 3 mm made of three different polymer materials is observed to change the wavelength that responds as the length changes. By performing the longitudinal tension experiment using three different SMART moorings, it was confirmed that there were linear wavelength changes in the response characteristics of the 3-mm-diameter SMART moorings. A 54-mm-diameter SMART mooring is produced to measure the response of longitudinal tension on the center, eye, and splice of the mooring, and a longitudinal tension of 100 t in step-by-step applied for the Maintained Test and Fatigue Cycle Test is conducted. By performing a longitudinal tension experiment, wavelength changes were detected in the center, eye, and splice position of the SMART moorings. The results obtained from each part of the installed sensors indicated a different strain measurement depending on the position of the SMART moorings. The variation of the strain measurement with the position was more than twice the result of the difference measurement, while the applied external load increased step-by-step. It appears that there is a correlation with an externally generated longitudinal tensional force depending on the cross-sectional area of each part of the SMART mooring.*

1. Introduction

A ship mooring system is a device that secures a vessel at a berth or during mooring operations to minimize the impact of waves. Offshore mooring lines secure an offshore floating structure during mooring operations, and they are capable of withstanding additional loads from movements due to wind, waves, and currents, with guaranteed durability over long-term use, thus serving as an essential component in offshore operations. Mooring lines are used not only for floating offshore wind turbines, but also for offshore plant equipment, as well as for securing offshore structures such as semi-submersibles, tension leg platforms (TLPs), and floating production storage and offloading (FPSO). With the broad range of potential applications, there has been continuous research on the development of mooring methods worldwide, including in Korea. The main functions for achieving load control of the mooring rope for securing offshore structures include pay out/heave in, auto tension, securing/braking, and in the case of auto-tension, pay out/heave in operations are repeatedly performed to maintain constant tension of the mooring rope (Lee et al., 2012).

According to these operational characteristics, there have been both large- and small-scale incidents and casualties, and there is a pressing need to ensure the safety of equipment as countermeasures against the incidents. To this end, a commonly used method that is employed for the protection of the mooring rope and equipment is to monitor and manage the load using load cells that measure torque and tension such that the tension is kept below a certain level. In the case of a mooring rope, operational problems that may affect safety are mainly known to arise in the areas of the eye and splice, which are the parts that serve

Received 20 January 2021, revised 13 March 2021, accepted 27 May 2021
Corresponding author Joseph Chul Chung: +82-41-522-3253, cytrnd@cytroniq.com

the important function of making a joint for successive ropes, and which are processed manually. In general, when mooring forces are measured using a load cell that measures tension, the load cell is mounted on the top or end of a mooring line to measure the average value; in this way, it is not possible to detect a load that has a concentrated distribution in the center, eye and splice parts of the mooring line.

In terms of the method employed to measure the rope tension using a load cell, the linear stress response characteristics can be used as much as possible in the case of chains and wires made of metals. However, in the case of synthetic mooring ropes, there are changes in stiffness due to the creep phenomenon that occurs when the ropes are used. Therefore, in the conventional load cell method that performs measurements using the linear stress response characteristics, there is a technical limitation in terms of determining the durability. For this reason, in the case of synthetic mooring ropes, they are used by significantly increasing the safety factor, or are discarded after a certain period regardless of the in-service history. Therefore, various approaches in research and development have been made for mooring ropes that allow load detection, and in recent years, there have been new technologies that incorporate mooring ropes/chains using sensor and smart IT technologies for monitoring methods with a load detection function composed of steel wires and chains. In addition, there have been demands for this type of function in the area of offshore wind turbines.

There has been mounting interest in the development of technology that is capable of integrating a number of sensors with smaller sizes, and which perform measurements of physical properties by connecting many sensors to continuous cables that enable the transmission of signals over a long distance between the sections where the sensors are installed. In this study, the use of the proposed sensor enables measurements of most of the physical quantities that need to be measured, as well as a simplification of the system constituting the sensor. For a comprehensive review of the general characteristics of fiber optic sensors, please refer to the (Culshaw et al., 2008). In this case, measuring equipment with sensors was designed, fabricated, and validated in various forms depending on the type of application. The widespread application of fiber optic sensors began after research on fiber Bragg grating (FBG) sensors started in the late 1990s (Meltz et al., 1989; Hill and Meltz, 1997).

In the theory of FBG, the reflected wavelength is determined by the refractive index modulation and of the core and the grating period. Eq. (1) represents this relationship as follows

$$\lambda_B = 2n_{eff}\Lambda \tag{1}$$

where λ_B : the reflected wavelength (called the Bragg wavelength)
n_{eff}: effective refractive index of the grating in the fiber core
Λ: grating period with modulation of the refractive index

When the grating period expressed in Eq. (1) is subject to an external force, linear length changes occur. Accordingly, the Bragg wavelength changes and the applied force are analyzed using the measurement of the changes in the wavelength. External forces are physical quantities composed of various factors such as temperature, pressure, strain, noise (sound), vibration, acceleration, and the slope. The sensor is made in the form of a probe to measure physical quantities with increased sensitivity to show linear changes of the grating period. For the sensor used in this study, a grating was designed by selecting the reflectance and reflected wavelength of a single-mode fiber optic, and the measurement equipment was implemented (Lee and Kim, 2011).

2. Materials and Methods

In previous studies, the applicable range of a mooring line is set by measuring the minimum breaking load (MBL) through a tensile load test by fabricating an actual mooring line after analyzing the material properties. With respect to the form of the mooring line for application in theoretical analysis, different forms of the mooring line are used in actual applications and for theoretical analyses, and it is difficult to apply the result of theoretical analysis to real-life outcomes, indicating a considerable difference between the theoretical analysis and the practical applicability. The mooring lines are often regarded as having a simple structure with several threads twisted, but in practice, the axial stiffness, coupling stiffness, and torsional stiffness of the mooring line exhibit different behaviors depending on the characteristics of the materials or changes in the type and degree of the twisting. The mooring lines are made using processes in the order of yarns-twisted threads-strands-ropes, and the final strength and wear resistance of the mooring line are significantly affected by the method and degree of the twisting in each process (Kim et al., 2018).

In practical applications, when the synthetic mooring ropes made from polymer materials are used to secure a vessel, the above characteristics lead to breaking of the rope; this is not observed in steel wires and chains, and the MBL is gradually reduced owing to non-linear changes in stiffness. The breaking of synthetic mooring ropes significantly affects the service life of the rope, and the main reason for the breaking is fatigue failure. The breaking appears in different patterns depending on the materials of the synthetic mooring rope. The A-type synthetic mooring rope is vulnerable to humidity, the B-type rope is vulnerable to creep, and the C-type rope is vulnerable to compressive fatigue failure; these are the main causes of breakages of ropes, and these factors determine the design and service life of the mooring lines. Creep is a phenomenon in which molecules gradually elongate when a synthetic mooring rope is used for a long time with a constant load applied to the rope made of combinations of polymers. In mooring lines exhibiting the creep phenomenon, it is very important to observe and monitor whether the creep occurs continuously owing to the applied loads, and it can lead to the breaking of the rope. The creep phenomenon leads to the permanent elongation of the synthetic mooring rope owing to temperature, time, and loads, and may occur in

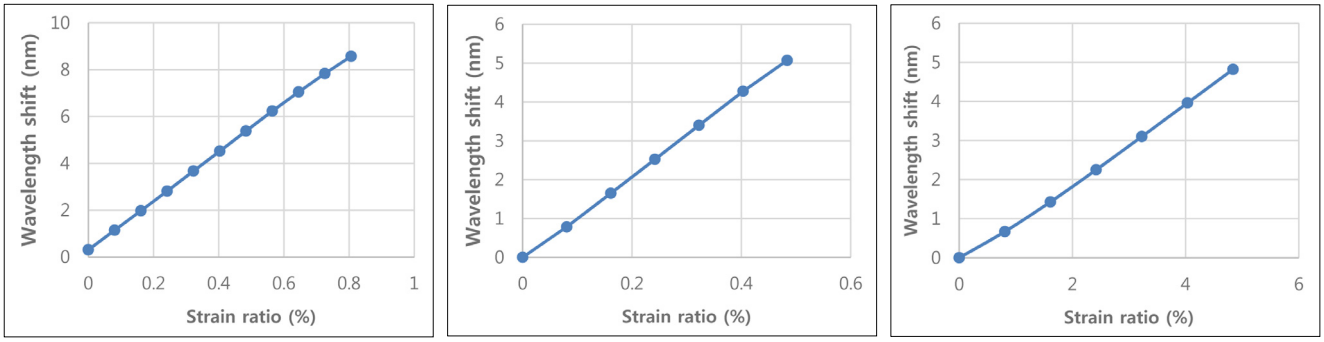

(a) SMART mooring (A-Type) (b) SMART mooring (B-Type) (c) SMART mooring (C-Type)

Fig. 1 Displacement test result for SMART mooring

all synthetic mooring ropes. It has been reported that the pattern of creep occurrence and corresponding result values differ depending on the type of the synthetic mooring ropes (Park et al., 2017).

In order to understand the characteristics of a Smart Mooring and Riser Truncation (SMART) mooring line with fiber optic sensors, basic properties were examined by manufacturing the mooring line with a diameter of about 3 mm. Using the multi-core fiber twisting device manufactured by CyTroniQ, fiber materials of A, B, and C types were integrated with the sensor of CyTroniQ Co., Ltd., which was introduced in the Introduction. The mooring line, which is integrated with the fiber optic sensor, was equipped with a sensor that responds to the external load, and is defined as a SMART mooring line. The developed system is characterized by arranging sensors in series so that the sensors can respond to a load that is applied partially to the mooring line. A strain test was performed on a mooring line with a diameter of 3 mm and a test length of 124 mm, and the following results were obtained. Fig. 1 shows the experimental results that examine the sensor response according to the change in the length of SMART mooring. The polymer materials used for the rope are A-Type, B-Type, and C-Type.

As shown in Fig. 1, with changes in the length of the mooring line, SMART mooring composed of A-Type material exhibited a wavelength shift of 8 nm with changes in length of up to 0.8%. SMART mooring composed of B-Type and C-Type materials exhibited a wavelength shift of 5 nm with a length change of 0.5%. In addition, the variation in the linear response characteristics of thesensors with the given changes in length were confirmed regardless of the materials, and according to the results obtained, the performance of the sensor was sufficient to conduct the breaking load test. Fig. 2 below shows the relationship between the universal test machine (UTM) and SMART mooring made of C-Type material to conduct the breaking load test. The tensile strength test was performed according to the standard of KS K 0412, and according to the change in length at a constant rate, the load was measured and recorded. The result of the tensile breaking load is shown in Fig. 3. From the results in Fig. 3, the increased length was 23.7 mm, exhibiting an elongation of 9.48%, and at this time, the maximum load was 3,145 N.

The SMART mooring fabricated as above was applied after

Fig. 2 Load test setup for UTM and SMART mooring (C-Type, Length 250 mm)

deformation and length design for use in the water basin test under the application of the scaling law. The results obtained from a scaled model experiment for the determination of parameters such as diameter ratio, stiffness, and length for the application of the scaling law to conduct the water basin test at 1/100 scale are discussed in a separate reference. (Bergdahl et al., 2016).

After confirming the potential applicability of the SMART mooring through a preliminary study with designs including smaller diameters as above, the main test was designed by fabricating the SMART mooring on an actual scale. For the B-type synthetic mooring rope, a product made by manufacturer D was used. For use in the mooring system of the offshore plants, Manufacturer D developed a B-type synthetic mooring rope for a mobile offshore drilling unit (MODU) and one for permanent mooring in sequence, with improvement in creep occurrence in the B-type synthetic mooring rope. In this study, because both a temporary mooring system and a permanent mooring

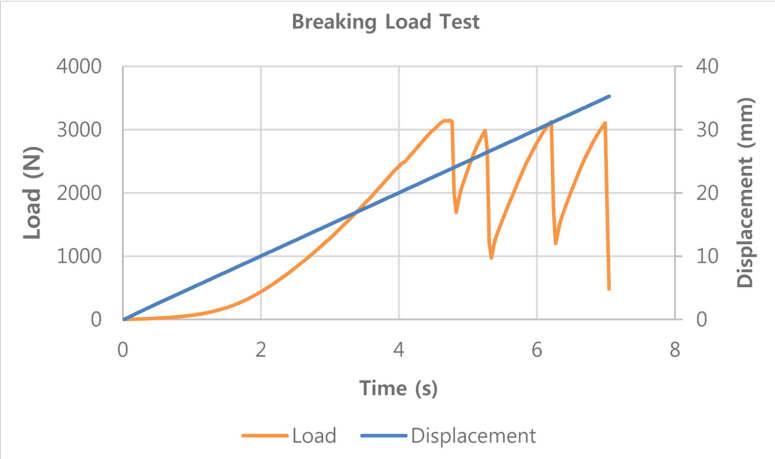

Fig. 3 Breaking load test result of SMART mooring (C-Type)

system are used, the products above were selected accordingly, and the variations in the creep characteristics of the B-type synthetic mooring rope with the experiment are presented in another study (Park et al., 2017).

After implementing the SMART mooring, a red light source was connected to the fiber optic inside the mooring line, and it was possible to examine the characteristics of light transmission to the opposite side. In order to implement the real-world SMART mooring, mooring rope with a diameter of around 54 mm (2-1/8 inch) and MBL at 186 t (411,000 lbs) was used, and the length of the fabricated SMART mooring was 6.33 m. Sensors were installed in key areas to make joints between ropes, namely the eye, splice, and center, to enable us to investigate the characteristics of the developed system. As shown in the picture in Fig. 4, the fiber optic sensors were integrated into the mooring rope, and a dedicated UTM was used for the tensile load test of the mooring rope. A tensile load of up to 100 t was applied, and the results were obtained at this point for analysis. The static tensile load and dynamic fatigue tensile load tests of the mooring rope were conducted according to the test method specified by ISO 2307, and the longitudinal tension and load were controlled using UTM. The test was conducted in the presence of Lloyd's Register. The changes in the wavelength of the SMART mooring connected to the load testing equipment were monitored during the tensile load test using a fiber optic sensor measurement unit (interrogator) (Lee and Kim, 2011).

Fig. 5(a) shows that with the SMART mooring, the longitudinal tension is changed to divide the tensile load into 10 levels, and the tensile load test was conducted with a maximum tensile load at 100 t. The response of the sensor in the mooring rope showed a linear change according to the load, and the linear response of the sensor was also measured in the maintained load state. In addition, it was confirmed that the sensor response changed in the same way with the increase in the load. As the load increased up to 100 t, the wavelength increased by 14 nm according to the sensor response, confirming that the response in the sensor changed in the same way according to the tensile load. Next, the variation of the strain according to the tensile load for the sensor connected to the eye position is depicted in Fig. 5(b).

Next, we present the result of the dynamic tensile load test obtained by measurements with a sensor connected to the eye position. The

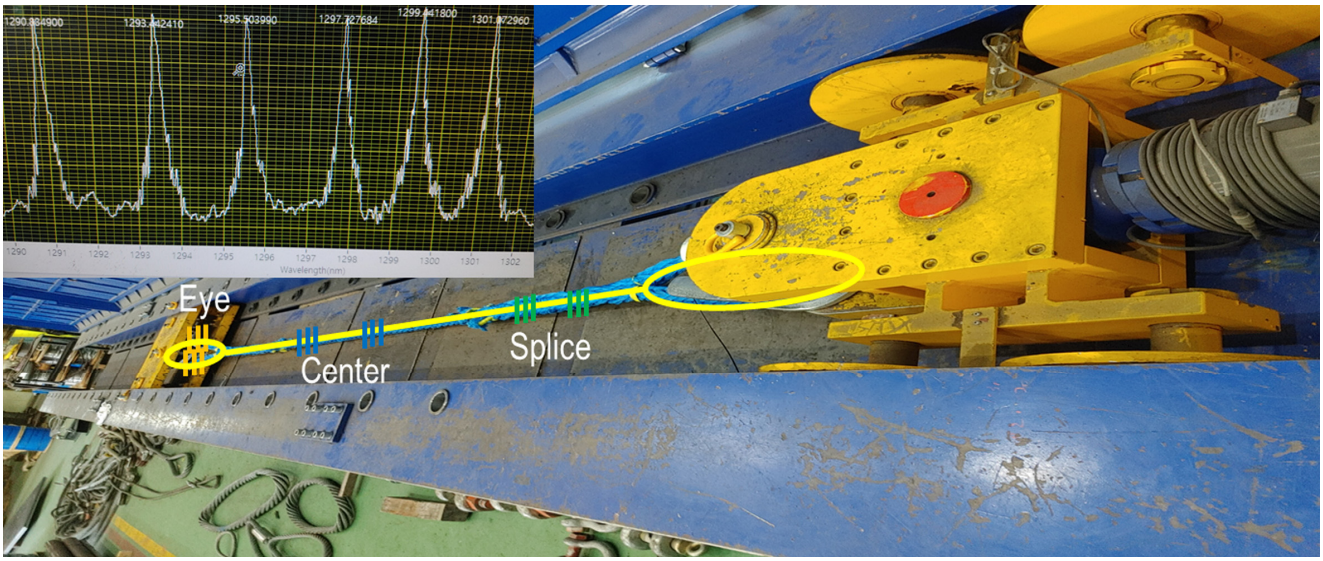

Fig. 4 Load test setup for UTM and SMART mooring (B-type)

cyclic tensile load was applied 100 times from 30 to 100 t, and the wavelength shift generated at this time was measured by the sensor. The results are shown in Fig. 6, which confirmed that with the application of the cyclic tensile load, the initial wavelength value showed a gradual increase. This is a typical characteristic of a mooring rope made of polymer materials, and by reflecting this characteristic, the sensor shows the same typical characteristic. Based on these results, it is expected that the findings of this study are utilized as instrumental data to determine the durability of SMART mooring according to cyclic loading. After the mooring rope is actually installed on-site, it is considered that the load data can be continuously measured to monitor the response of the mooring rope, and with the accumulation of the associated data, the developed technology can be used to determine the remaining service life.

Fig. 7 shows the results of measuring the wavelength shift, that is, the strain, in the eye, center, and splice positions of the SMART mooring during the cyclic tensile load test when a load of 30−100 t is applied 100 times in the time domain. From the results, it was confirmed that sensors show responses according to the cycling loading in the eye, center, and splice positions, respectively. From the results of the measured strain, the magnitude of the strain differed depending on the sensor position. The center position showed the largest strain, followed by the splice position and the eye position with the smallest strain. This is believed to be related to the cross-sectional area of the SMART mooring structure subject to the tensile load. The strain at the center position, which is the position with the smallest cross-sectional area of the SMART mooring subject to the tensile load, was about twice as large as the strain at the eye position, whether the material in the center position was used to make a ring in the eye position, leading to the cross-sectional area for the longitudinal tension being twice as large as that of the center position. Further, in the splice position, the strain slightly smaller than that in the center position was measured. From the values of the strain measured in the eye, center, and splice positions, a gradual wavelength shift to the larger values was observed, and it was possible to differentiate between the loads for each position. It was confirmed that the elongation of the final SMART mooring increased from the initial 6.33 m to 7.08 m, which is an increase of 0.75 m, according to the cyclic tensile load of 30−100 t. The result showed a clear difference from the characteristics of restoring force in general metals.

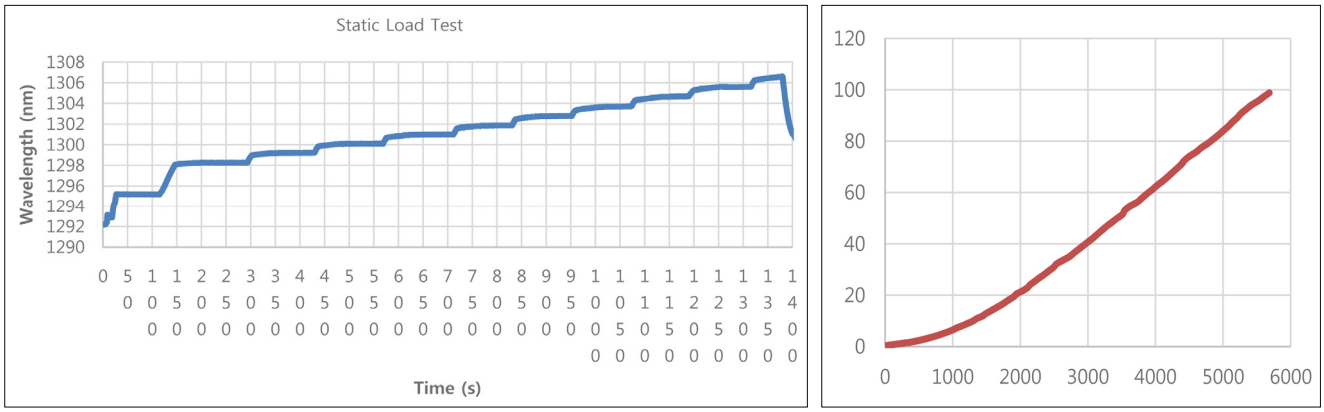

(a) Time history result at center position (b) Tensile load vs strain at eye position

Fig. 5 Static tensile load response of SMART mooring (B-Type)

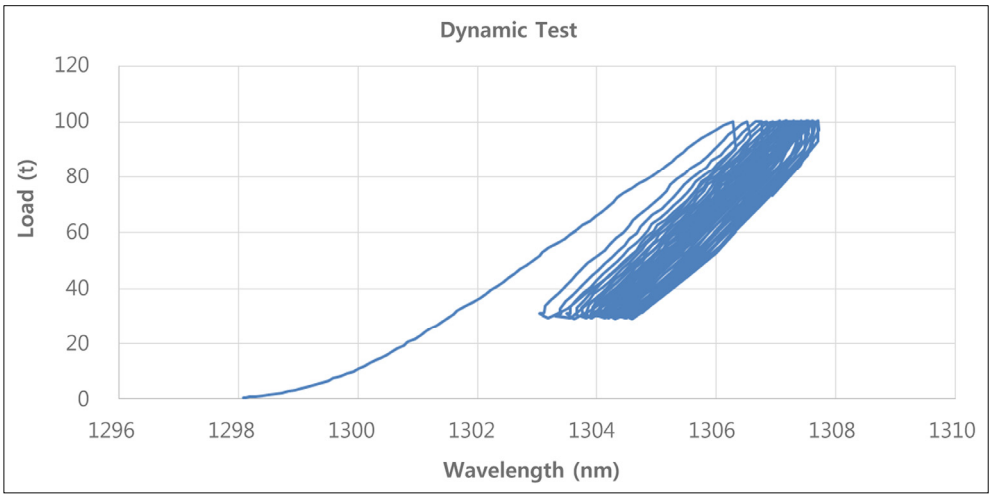

Fig. 6 Dynamic tensile load histogram of SMART mooring (B-Type) at eye position

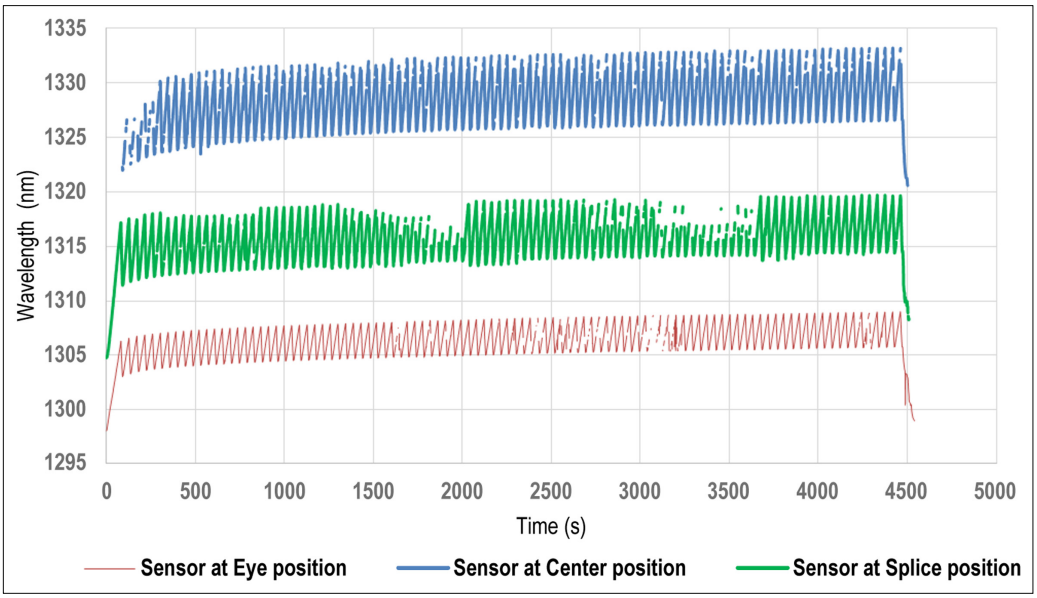

Fig. 7 Dynamic tensile load of SMART mooring (B-Type) at eye/center/splice position

3. Summary and Conclusion

This study focused on an area of research that is different from previous studies, and SMART mooring was designed and implemented. The results of the tests conducted in this study are outlined in Table 1 below.

In the case of mooring lines, operational problems mainly occur in the eye and splice regions, which are the parts that serve an important function of making a joint for successive ropes, and which are processed manually. In a structure characterized by a continuous connection with a single material without interruption, when the local cross-sectional area encounters a change, the suitable load detection in the mooring line was not possible in terms of technology employed to measure the local tension. In order to address this limitation, this study used sensors that are integrated into the mooring line to detect the load transmitted to the eye, splice, and center positions of the mooring line without a separate protective device, unlike in the case of load cell-type sensors used with an electric method. In addition, with the developed system, it is possible to utilize the excellent characteristics of the fiber optic sensor, which is not influenced by external high-power electromagnetic interference. When synthetic mooring ropes are subjected to a tensile load for a long time, a creep phenomenon, which is an increase in permanent elongation, occurs, leading to stress stiffening. Consequently, the stress stiffening affects the mooring line analysis.

For an effective method to determine the service life and the remaining service life according to the service history of the mooring line, the real-time measurement of in-service history plays an important role. By using these measurements to develop a database, it is possible to utilize them as essential elements in a strategic manner, and to realize the analysis and control of realistic problems with enormous potential for the cyber physical system that performs the modeling of realistic values, and which provides the realistic physics value to the computer-based virtual world for prediction and control.

Table 1 Summary of test results for tensile load test of SMART mooring using sensor

	SMART mooring for model test	SMART mooring for real size	Note
SMART mooring Diameter dimension	3 mm	54 mm (2-1/8 inch)	Static/Dynamic tensile load testing
Mooring material type	A, B, C-Type	B-Type	
Measurement speed	100 Hz	100 Hz	
Testing condition	Displacement/Breaking load test	Static load / Dynamic fatigue	
Testing tensile load	3,500 N @ C-Type	0.5−100 t (10 step), 30−100 t, 100 cycle test	
Wavelength shift (strain) of static testing result	Displacement: 5 nm, 8.5 nm Breaking load test: over 50 nm	Center position:14 nm	
Wavelength shift (strain) of cycle testing result	-	Eye position: 3.6−6 nm Center position: 7.5−11.2 nm Splice position: 6.1−8.2 m	

Through this study, it is expected that the developed SMART mooring will be extensively utilized for applications with fiber optic sensors as a useful sensing method in the digital twin system and cyber physical system, advancing beyond the concept of the Internet of Things (IoT).

Funding

This research was supported by Korea Institute for Advancement of Technology (KIAT) grant funded by the Korea Government (MOTIE) (P0004247).

References

Lee, Y.J., Kim, G.S., Kim, H.J., & Lee, G.G. (2012). A Study on the Load Measurement of Ship Mooring Equipment. Proceedings of the Korean Society of Precision Engineering Conference, 867–868.

Culshaw, B., & Kersey, A. (2008). Fiber-Optic Sensing: A Historical Perspective. Journal of Lightwave Technology, 26(9), 1064–1078.

Meltz, G., Morey, W.W., & Glenn, W.H. (1989). Formation of Bragg Gratings in Optical Fibers by Transverse Holographic Method. Optics Letters, 14(15), 823-825. https://doi.org/10.1364/OL.14.000823

Hill, K.O., & Meltz, G. (1997). Fiber Bragg Grating Technology Fundamentals and Overview. Journal of Lightwave Technology, 15(8), 1263–1276. https://doi.org/10.1109/50.618320

Lee, M., & Kim, H. (2011), Latest Development Status of FBG Sensors & Interrogator from Korea & Other Countries. Journal of Korean Society of Civil Engineers, 59(2), 84–90.

Park, S.M., Lee, S.J., & Kang, S.W. (2017). A Study on Creep Effect of Synthetic Fiber Rope Mooring System on Motion Response of Vessel and Tension of Mooring Line. Journal of the Society of Naval Architects of Korea, 54(2), 151–159. https://doi.org/10.3744/SNAK.2017.54.2.151.

Kim, K.-S., Kim, N.-H., Seo, M.-K., Park, E.-J., Kim, D.-K., & Shin, H.-K. (2018). Development of Mooring Rope Using High Density Polyethylene. Journal of the Korean Society of Marine Engineering, 42(4), 338–342. https://doi.org/10.5916/jkosme.2018.42.4.338

Bergdahl, L., Palm, J., Eskilsson, C., & Lindahl, J., (2016). Dynamically Scaled Model Experiments of a Mooring Cable. Journal of Marine Science and Engineering, 4(1), 1–18. https://doi.org/10.3390/jmse4010005

Author ORCIDs

Author name	ORCID
Chung, Joseph Chul	0000-0003-3240-0407
Lee, Michael Myung-Sub	0000-0001-6483-7895
Kang, Sung Ho	0000-0002-5817-0024

KSOE

Journal of Ocean Engineering and Technology 35(4), 273-286, August, 2021
https://doi.org/10.26748/KSOE.2021.019

pISSN 1225-0767
eISSN 2287-6715

Original Research Article

Optimization of SWAN Wave Model to Improve the Accuracy of Winter Storm Wave Prediction in the East Sea

Bongkyo Son[1] and Kideok Do[2]

[1]*Master's Course, Department of Convergence Study on the Ocean Science and Technology, Korea Maritime & Ocean University, Busan, Korea*
[2]*Associate Professor, Department of Ocean Engineering, Korea Maritime & Ocean University, Busan, Korea*

KEY WORDS: East Sea, SWAN, ST6, Model skill assessment, Wind waves

ABSTRACT: *In recent years, as human casualties and property damage caused by hazardous waves have increased in the East Sea, precise wave prediction skills have become necessary. In this study, the Simulating WAves Nearshore (SWAN) third-generation numerical wave model was calibrated and optimized to enhance the accuracy of winter storm wave prediction in the East Sea. We used Source Term 6 (ST6) and physical observations from a large-scale experiment conducted in Australia and compared its results to Komen's formula, a default in SWAN. As input wind data, we used Korean Meteorological Agency's (KMA's) operational meteorological model called Regional Data Assimilation and Prediction System (RDAPS), the European Centre for Medium Range Weather Forecasts' newest 5th generation re-analysis data (ERA5), and Japanese Meteorological Agency's (JMA's) meso-scale forecasting data. We analyzed the accuracy of each model's results by comparing them to observation data. For quantitative analysis and assessment, the observed wave data for 6 locations from KMA and Korea Hydrographic and Oceanographic Agency (KHOA) were used, and statistical analysis was conducted to assess model accuracy. As a result, ST6 models had a smaller root mean square error and higher correlation coefficient than the default model in significant wave height prediction. However, for peak wave period simulation, the results were incoherent among each model and location. In simulations with different wind data, the simulation using ERA5 for input wind datashowed the most accurate results overall but underestimated the wave height in predicting high wave events compared to the simulation using RDAPS and JMA meso-scale model. In addition, it showed that the spatial resolution of wind plays a more significant role in predicting high wave events. Nevertheless, the numerical model optimized in this study highlighted some limitations in predicting high waves that rise rapidly in time caused by meteorological events. This suggests that further research is necessary to enhance the accuracy of wave prediction in various climate conditions, such as extreme weather.*

1. Introduction

Ocean wave predictions are made using numerical wave models that calculate the spectrum changes caused by the growth and dissipation of wave energy, mainly using spatial-temporal wind data as input. Numerical wave models can be divided into first-generation, second-generation, and third-generation models according to the number of source terms in their governing equations. Studies on predicting or simulating waves have mainly used third-generation numerical wave models, such as Simulating Waves Nearshore (SWAN), Wave Watch III, and Wave Model (WAM), which solve an action density balance equation to calculate the wave spectrum. Previous studies have developed more accurate simulations of parameters, such as significant wave height and peak period, and have improved modeling performance. Regarding studies on wave prediction in the waters around Korea, Kang et al. (2015) and Eum et al. (2016) employed the SWAN third-generation numerical wave model to simulate waves in the waters around the Korean peninsula using weather forecasting data provided by the European Centre for Medium Range Weather Forecasts (EMCWF) and Japanese Meteorological Agency (JMA) as input data.

Lee et al. (2010) used SWAN to simulate storm waves occurring on the east coast of Korea during winter, and Chun et al. (2014) developed a modified version of WAM for use in shallow waters and simulate storm waves occurring on the east coast. Do and Kim (2018) and Caires et al. (2018) simulated large-height swell-like waves on the east coast of Korea during winter using SWAN and the energy dissipation term coefficient calibration method for white-capping proposed by

Received 20 April 2021, revised 15 June 2021, accepted 2 July 2021
Corresponding author Kideok Do: +82-51-410-5248, kddo@kmou.ac.kr

Rogers et al. (2003). Large-height swell-like waves occur when strong extratropical cyclones develop in strong winds on the East Sea during winter. As the resulting storm waves approach the coast, they develop into waves with a long period (approximately 9–15 seconds) and large height (3 m or more) (Oh et al., 2010). The wind input data used for this include the spatial-temporal wind data from Weather Research and Forecasting (WRF) the ocean weather forecast system's model (Park et al., 2015), Regional Data-Assimilation, and Prediction System (RDAPS) and Local Data-Assimilation and Prediction System (LDAPS) forecast models used for operational meteorological forecasting by Korean Meteorological Agency (KMA). Lee and Ahn (2018) simulated waves in the Yellow Sea and East China Sea using SWAN's energy dissipation term coefficient calibration method for white-capping. Also, KMA is currently operating a wave forecast system (global, regional, and local coastal model), which was built based on Wave Watch III.

Recently, hazardous large-height swell-like waves have repeatedly struck the east coast of Korea in winter (October–February) and have caused many instances of human and property damage. Since 2005, the number of diseased and missing persons due to large-height swell-like waves has reached 70, and the scale of property damage has exceeded an annual average of 10 billion KRW (Lee et al., 2014; Oh et al., 2010). To improve the forecast accuracy for hazardous waves that occur on the east coast of Korea during winter, this study performed numerical simulation of waves using SWAN, a third-generation numerical wave model that is used worldwide, and the Source Term 6 (ST6) developed by Rogers et al. (2012) by calculating physical coefficients based on recent field observations. The results of this study were compared to results obtained using the existing empirical formula created by Komen et al. (1984). As the input wind data for the numerical wave model, this study used data from RDAPS, which is KMA's operational meteorological model, ECMWF's latest 5th generation re-analysis model (ERA5), and the JMA meso-scale model (JMA-MSM). RDAPS data can be downloaded in real-time through KMA's Open MET Data Portal (http://data.kma.go.kr), and the JMA-MSM data were procured from JMA's database. The ERA5 data were obtained using Python and the application programming interface provided by ECMWF. In this study, the operational meteorological model's results and wind data generated as re-analysis data were used as input to the SWAN to simulate the waves that occurred on the East Sea from November 2016 to February 2017. The model results were compared with wave observation data from 6 locations on the open seas operated by KMA and the Korea Hydrographic and Oceanographic Agency (KHOA), and an optimization study was performed to improve the accuracy of the numerical model through error analysis.

2. Numerical Model

2.1 Simulating Waves Nearshore (SWAN)

This study performed numerical simulation of wave on the East Sea during the winter from November 2016 to February 2017 using SWAN (Booij et al., 1999), a numerical wave model developed at Delft University of Technology in the Netherlands. With its numerical models, SWAN is capable of considering the wave propagation from wind-induced wave growth, refraction, shoaling, reflection, and diffraction. Simultaneously, it can also consider deformation caused by nonlinear wave actions (triad/quadruplet wave–wave interactions) as well as the wave energy dissipation caused by white-capping, breaking, and bottom friction. SWAN's governing equation is a wave action balance equation that expresses waves in the form of a directional wave spectrum and calculates energy spectrum changes in a 2D horizontal space as follows:

$$\frac{\partial N}{\partial t}+\frac{\partial c_x N}{\partial x}+\frac{\partial c_y N}{\partial y}+\frac{\partial c_\sigma N}{\partial \sigma}+\frac{\partial c_\theta N}{\partial \theta}=\frac{S_T}{\sigma} \tag{1}$$

where θ is the direction, and σ represents each frequency, expressed as $2\pi/f$. N is the wave action density spectrum, where the wave energy spectrum is divided by each frequency and is expressed as $N=E(\sigma,\theta)/\sigma$. $c_x, c_y, c_\theta, c_\sigma$ are the wave energy propagation speeds at each phase (x, y, θ, σ). on the right side is a source term that shows the generation and reduction of wave energy density caused by wind, nonlinear wave actions, white-capping, bottom friction, and breaking as follows:

$$S_T = S_{in} + S_{nl3} + S_{nl4} + S_{ds,w} + S_{ds,b} + S_{ds,br} \tag{2}$$

S_{in} is the growth in wave energy caused by the wind. S_{nl3} and S_{nl4} are the terms for energy dissipation caused by triad/quadruplet wave-wave interactions, respectively. $S_{ds,w}$, $S_{ds,b}$, and $S_{ds,br}$ are the terms for energy dissipation caused by white-capping, bottom friction, and depth-induced wave breaking, respectively. White-capping is a breaking phenomenon caused by wave steepness on the open ocean, and it is difficult to describe with an equation due to its strong nonlinear behavior and turbulence phenomena; as such, it is determined by an empirical equation. In SWAN, the term for energy dissipation caused by white-capping ($S_{ds,w}$) is expressed by Hasselmann's (1973) pulse-based model, where the wave number (k) becomes a variable, as shown in Eq. (3) (WAMDI Group, 1988):

$$S_{ds}(\sigma,\theta) = -\Gamma\tilde{\sigma}\frac{k}{\tilde{k}}E(\sigma,\theta) \tag{3}$$

where $\tilde{\sigma}$ and $\tilde{k}$ are the mean of each frequency and mean wave number, respectively, and Γ is the coefficient resulting from the total wave steepness, as shown in Eq. (4):

$$\Gamma = \Gamma_{KJ} = C_{ds}((1-\delta)+\delta\frac{k}{\tilde{k}})(\frac{\tilde{s}}{\tilde{s}_{PM}})^p \tag{4}$$

where C_{ds} is the energy dissipation coefficient, δ is the white-capping

weight value with respect to the wave number, $\tilde{s}$ is the total wave steepness, $\tilde{s}_{PM}$ is the total wave steepness of the Pierson–Moskowitz spectrum, which is $\sqrt{3.02\times10^{-3}}$, and p is the exponent of the value of $\tilde{s}$ normalized by $\tilde{s}_{PM}$. In SWAN, the C_{ds}, δ, and p terms are tunable coefficients , and $C_{ds}=2.36\times10^{-5}$, $\delta=0$ and $p=4$ were used as default values. When these values were used, there was a problem with underestimating the wave periods by approximately 10–20%. To improve on this, Rogers et al. (2003) modified δ from 0 to 1. Do and Kim (2018) used this to successfully simulate the large-height swell-like waves that occurred on the east coast of Korea in the winter of 2015. Since SWAN version 40.91A, $C_{ds}=2.36\times10^{-5}$, $\delta=1$, and $p=2$ have been used as default values. ST6's term for energy dissipation caused by white-capping is expressed as two phases, as shown in Eq. (5):

$$S_{ds}(f,\theta)=[T_1(f,\theta)+T_2(f,\theta)]N(f,\theta) \tag{5}$$

$$T_1(f,\theta)=a_1A(f)f[\frac{\triangle(f)}{\tilde{E}(f)}]^L E(f,\theta) \tag{6}$$

$$T_2(f,\theta)=a_2[\int_0^k A(f')[\frac{\triangle(f')}{\tilde{E}(f')}]^M df']E(f,\theta) \tag{7}$$

where T_1 is the local dissipation term, and T_2 is the cumulative dissipation term, as given by Eqs. (6) and (7), respectively. This study's numerical wave model used a combination of 4 parameters (DL1M1, UL1M4, UL2M2, and UL4M4) that were verified by Rogers et al. (2012) through white-capping energy dissipation term coefficient calibration. The quantitative values for these parameters are listed in Table 1, where $\tilde{E}(f)$ is the total density spectrum, L and M are the exponents that modify energy dissipation, and a_1 and a_2 are constants that adjust the local and cumulative dissipation terms, respectively.

Table 1 ST6 parameters (Rogers et al., 2012)

Parameter	$\tilde{E}(f)$	L	M	a_1	a_2
DL1M1	$E(f)$	1	1	2.0×10^{-4}	1.6×10^{-3}
UL1M4	$E_T(f)$	2	2	8.8×10^{-6}	1.1×10^{-4}
UL2M2	$E_T(f)$	1	4	5.7×10^{-5}	3.2×10^{-6}
UL4M4	$E_T(f)$	4	4	5.7×10^{-7}	8.0×10^{-6}

For detailed information on the aforementioned equations and parameters, see Rogers et al. (2012) and Wave Watch III (The WAVEWATCH III Development Group, 2016). These are used in the same manner in SWAN.

2.2 Sea Surface Wind Data

Numerical wave models use spatial-temporal sea surface wind data as input. Because data for the entire scope of the ocean are required, the results of numerical weather forecast models are used. As input wind data for its numerical simulation of waves on the East Sea, this study used wind data from RDAPS, which is operated by KMA, JMA-MSM, and ERA5. The ERA-Interim data provided by ECMWF have a temporal resolution of 6 h, which is considered limited for simulating waves that occur during rapidly changing severe weather (Do and Kim, 2018). The ERA5 single-level sea surface wind data, which have a temporal resolution of 1 h, were used for the input conditions of the numerical simulation of waves. RDAPS uses four-dimensional variational data assimilation (4D-Var) and is operated alongside LDAPS. Although LDAPS has a higher spatial-temporal resolution than RDAPS at 1.5 km and 3 h, it has limitations regarding numerical simulation of waves on the East Sea because its modeling area is limited to the area around the Korean peninsula, and it does not include the entire East Sea. Also, according to Do and Kim (2018), there is no great difference between the wave simulation results obtained by combining the results of LDAPS and RDAPS and the wave simulation results obtained using results of RDAPS alone; therefore, this study used RDAPS. The JMA-MSM (Saito et al., 2006) wind data are the product of a meso-scale weather forecast model operated by JMA and have a high spatial-temporal resolution. As such, these data have been used as input data in previous studies on numerical simulation of waves in the waters around Korea (Kim et al., 2020; Kwon et al., 2020; Yoon et al., 2020). Table 2 lists the spatial-temporal resolution, area, and data provision period for the 3 models used as input wind data in this study. To summarize the characteristics of each set of wind data, the RDAPS data have better spatial resolution than ERA5; however, at 3 h, its temporal resolution is lower than that of ERA5 and JMA-MSM. ERA5 has fairly poor spatial resolution, but it has a temporal resolution of 1 h, which allows for the analysis of rapidly changing weather conditions during severe weather, making it highly useful. JSM-MSM has a higher spatial

Table 2 Input wind data information

	RDAPS	ERA5	JMA-MSM
Provided by	KMA	ECMWF	JMA
Type	Forecasting data	Re-Analysis data	Forecasting data
Analysis period	2011–Present	1979–Present	2004–Present
Spatial resolution	12 km	31 km	5 km
Temporal resolution	3 Hourly-Data	Hourly-Data	Hourly-Data
Area	12.2 °N ~ (12 km × 491) 101.5 °E ~ (12 km × 419)	Global	22.4–47.6 °N 120–150 °E

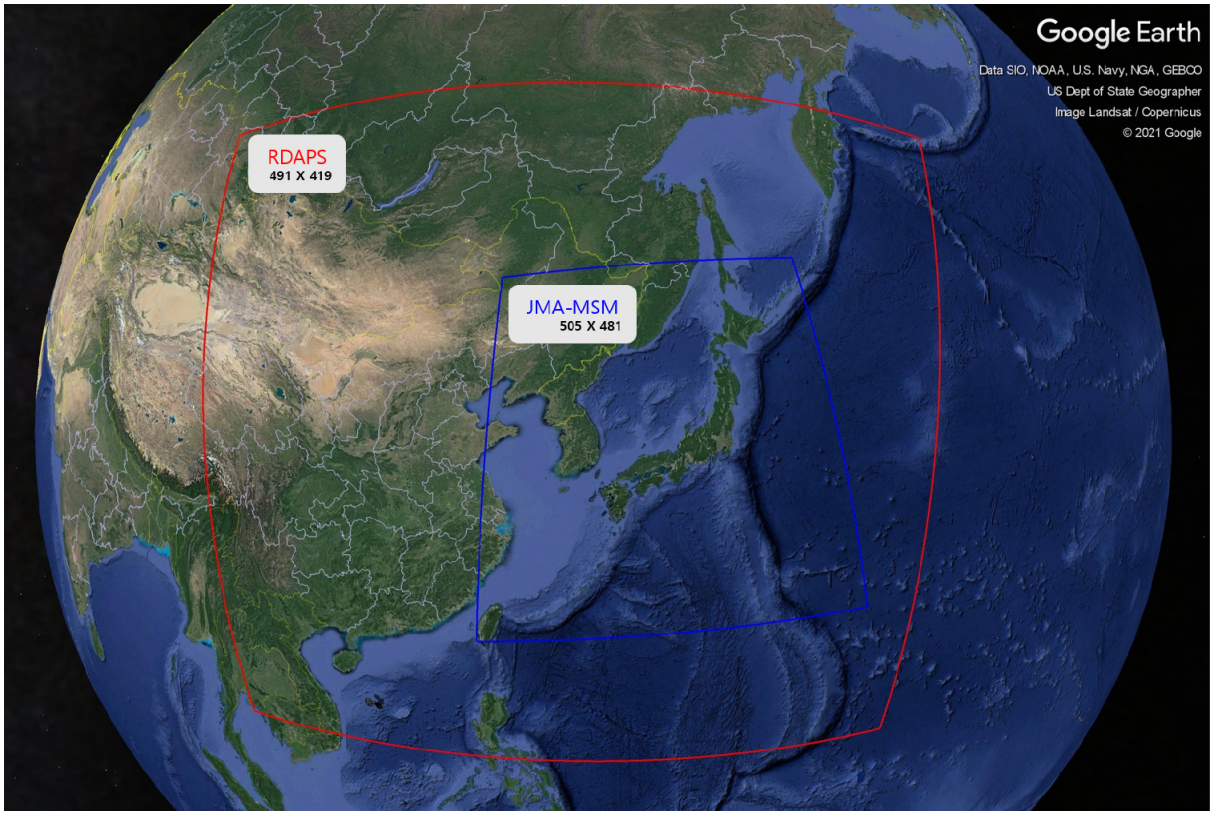

Fig. 1 Domain grids of RDAPS and JMA-MSM

resolution (5 km) than the other two models, and it has the advantage of providing the same 1 h temporal resolution as ERA5. Fig. 1 shows the operating range and grid numbers for the RDAPS and JMA-MSM input wind data used in this study. ERA5 is not shown as it is a global model.

2.3 Physical Coefficients, Grid, and Water Depth

The calculation area of the model constructed in this study was set as an equidistant grid with a 0.05° × 0.05° resolution containing the entire East Sea, including the Sea of Okhotsk, to model the development, propagation, and dissipation of storm waves caused by

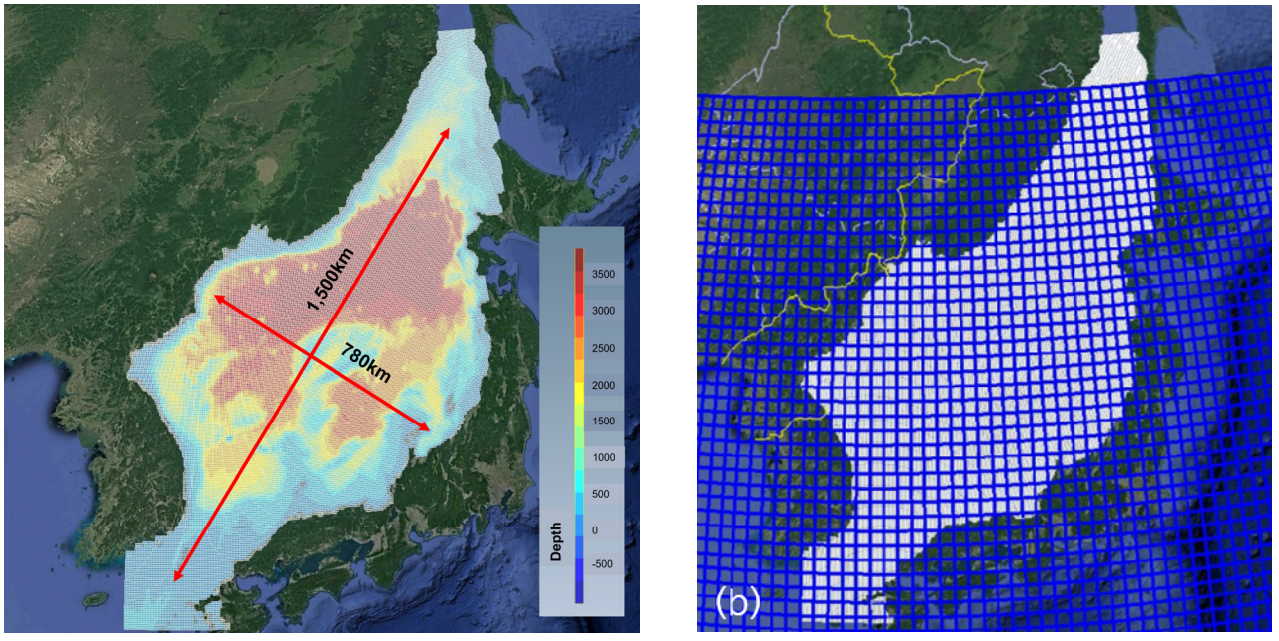

(a) Bottom topography of model computational area (ETOPO1)

(b) Domain grids of model's computational area (white) and JMA-MSM (blue)

Fig. 2 Computational domains of East Sea wave numerical modeling

Table 3 Physical parameter settings of SWAN model

Parameters	Contents
Frequency space	41 bins from 0.03 to 1.5 Hz (33-0.67 s)
Directional space	48 bins with 7.5° intervals (48 × 7.5° = 360°)
Bottom friction	0.038 m^2/s^3 (Zijlema et al., 2012)
Water density	1,025 kg/m^3
Gravitational acceleration	9.81 m/s^2
Accuracy	criteria = 99% (maximum of 99 iterations per time step)
Integration time step	20 min (Fixed)

wind. The numerical model's water depths are based on ETOPO1 (https://www.ngdc.noaa.gov/mgg/global/), which are satellite bathymetry data provided by the United States' National Oceanic and Atmosphere Administration (Fig. 2(a)). When the model's grid was generated, the range of the weather data provided by JMA-MSM did not include the northern part of the Sea of Okhotsk, and the model grid for this area was modified as shown in Fig. 2(b).To closely model the periodic components of long-period waves, such as large-height swell-like waves, this study divided the wave energy spectrum frequency into 41 parts from 0.03 to 1.5 Hz and divided the wave direction into 48 parts in 7.5° intervals to calculate the wave energy spectrum. Also, the additional physical parameters required to operate the SWAN model were set as listed in Table 3.

3. Numerical Wave Model Scenarios and Model Parameters

This study analyzed wave observation data with a focus on the winter season, in which large-height swell-like waves occur with great frequency. The numerical simulation period was set as November 2016 to February 2017, a period when a large number of large-height swell-like waves occurred.

For the numerical simulation of waves method, the ST6 proposed by Rogers et al. (2012) was applied to the East Sea numerical wave model. For the parameters in the model, combinations of the 4 parameters listed in Table 1 were used to simulate large-height swell-like waves, and these were compared with observation data for validation. Also, research was performed on optimizing the numerical wave model by comparing its results with the results of a simulation that uses an empirical equation by Komen et al. (1984), which is currently the default setting for SWAN. In this study, the model results were divided according to the parameter settings and the input wind data provided by each different organization (RDAPS, ERA5, and JMA-MSM). Table 4 gives an overview of the names, input wind data, model settings, and parameters of the simulation scenarios considered in this study.

As the wave observation data for validating and optimizing the numerical model, this study used data from the KHOA's ocean observation buoys (Northeast of Ulleungdo, E01; Northwest of Ulleungdo, E02) and KMA's open sea buoys (East Sea, DH; Ulleungdo, URD; Pohang, PH; Uljin, UJ), and Fig. 3 shows the locations and water depths of each observation buoy. In this study, the significant wave height and peak wave period data observed at each location were used to analyze the accuracy of the numerical wave model. To judge the model accuracy in detail, this study used wave observation data that had undergone primary data quality validation by Wave Information Network of Korea (Jeong et al., 2018).

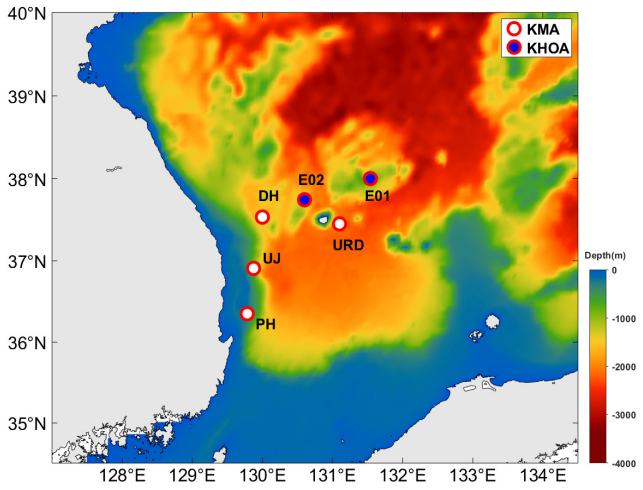

Fig. 3 Locations of wave and wind observation sites from KMA & KHOA

Table 4 Abbreviation of parameter settings of East Sea wave numerical modeling

Input wind			RDAPS	ERA5	JMA-MSM
Physics	ST6 Rogers et al. (2012)	DL1M1	RDAPS-DL1M1	ERA5-DL1M1	JMA-DL1M1
		UL1M4	RDAPS-UL1M4	ERA5-UL1M4	JMA-UL1M4
		UL2M2	RDAPS-UL2M2	ERA5-UL2M2	JMA-UL2M2
		UL4M4	RDAPS-UL4M4	ERA5-UL4M4	JMA-UL4M4
	Komen et al. (1984)	Komen	RDAPS-Komen	ERA5-Komen	JMA-Komen

4. Validation and Analysis of Numerical Model Results

In this study, the ST6 and parameter settings, which were developed to improve the numerical wave model proposed by Rogers et al. (2012), were used in simulation of winter waves occurring on the East Sea, and the forecast accuracy regarding significant wave height and peak wave period was evaluated. As mentioned previously, data provided from Korea, Japan, and Europe were used to verify the consistency of the model's results according to the spatial-temporal input wind data. The results were compared with the results of simulations that use the empirical equation by Komen et al. (1984), which is the default setting of the SWAN model. In addition, the simulation results using the wind data provided by different organizations were compared to evaluate the simulation results regarding their input wind data. To quantitatively verify the simulation results, a statistical analysis of the difference between the model results and observation data was performed. The model evaluation items used for this analysis included the bias, root mean square error (RMSE), correlation coefficient (ρ), and index of agreement (IOA), as given by Eqs. (8)–(11), respectively:

$$\text{Bias} = \frac{1}{n}\sum_{i=1}^{n}(M_i - O_i) \tag{8}$$

$$\text{RMSE} = \sqrt{\frac{1}{n}\sum_{i=1}^{n}(M_i - O_i)^2} \tag{9}$$

$$\rho = \frac{\sum_{i=1}^{n}(M_i - \overline{M})(Oi - \overline{O})}{\sqrt{(M_i - \overline{M})^2 (O_i - \overline{O})}} \tag{10}$$

$$\text{IOA} = 1 - \frac{\sum_{i=1}^{n}(M_i - O_i)^2}{\sum_{i=1}^{n}(|M_i - \overline{O}| + |O_i - \overline{O}|)^2} \tag{11}$$

where n is the number of observation data, M is the model's result value, O is the observed value, $\overline{M}$ and $\overline{O}$ are the respective mean values of M, O. In the statistical analysis, a comparison was made between the observed values and model results over a 1 h interval only in cases where the values in the observed significant wave height time series data during the interval were $\geq$1.0 m. This was done to systematically evaluate the actual prediction accuracy by removing the observation data error that occurs when wave height is low.

First, to evaluate the accuracy of the weather forecast data used as input to the numerical wave model, the wind speed and wind direction observed at the locations in Fig. 3 were compared to the input wind data, and the RMSE values for each weather model were plotted in a bar graph (Fig. 4). In the comparison process, the 2017 wind data from the KHOA-operated ocean observation buoys E01 and E02 were missing, and the data from the KMA-operated weather observation buoys DH, PH, URD, and UJ were used. When the data were analyzed, the ERA5 wind speed and wind direction had high overall accuracy, but the RDAPS forecast model had the lowest error at the DH. In the case of wind direction, there was no great difference in accuracy between the wind data produced by JMA-MSM and ERA5. In the case of wind speed, the accuracy of JMA-MSM was found to be excellent considering that it is a forecast model (Fig. 4 shows that JMA-MSM's wind speed had a higher RMSE of approximately 0.5 m/s than ERA5, which is re-analysis data.).

To find the input wind data and model composition that are most suitable for simulating large-height swell-like waves on the east coast of Korea in winter, significant wave height results for each simulation scenario were quantitatively analyzed, and the error statistics are listed in Table 5. It can be seen that the significant wave height simulation results from the ST6 configured with the UL4M4 parameter combination had the lowest error (RMSE of 0.02–0.18 m) and the highest correlation coefficient and IOA, regardless of the input wind data. In contrast, when the DL1M1 parameter combination was used with the ST6, the simulation accuracy was the lowest. Fig. 5 shows a time series of the observation data and the significant wave height simulation results for each location predicted using the UL4M4

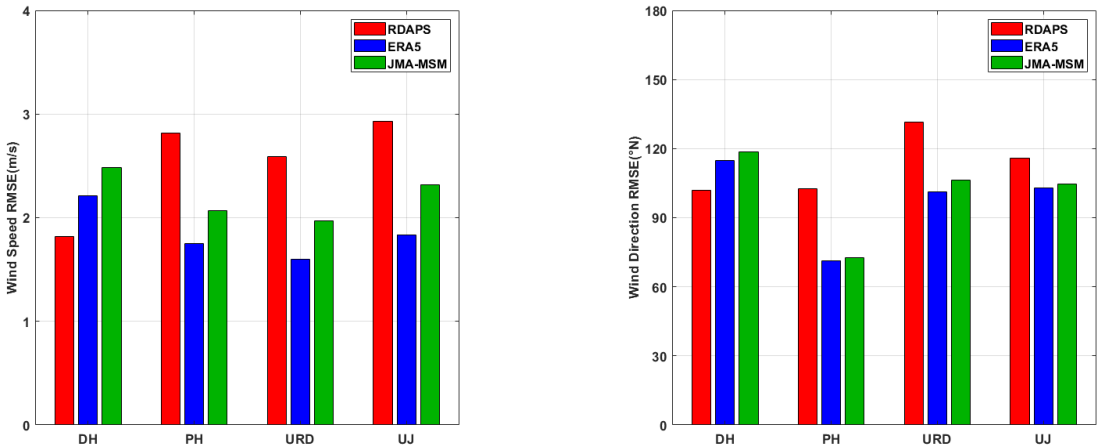

Fig. 4 Bar graphs of RMSE of input wind data (wind speed and direction) at 4 locations

parameters, which had the highest accuracy of all parameter settings (RDAPS/ERA5/JMA-MSM-UL4M4). To evaluate the forecast accuracy for hazardous waves that occur during severe weather, the ST6's significant wave height simulation results using 4 parameter settings (DL1M1, UL1M4, UL2M2, UL4M4) were divided up according to the input wind data for December 19−31, 2016, which was a period when the significant wave height observed values were 4 m or greater and the numerical model's error was high, and this is shown in Fig. 6. Here, there was no great difference in the error values between the model and observation data for each of the observation locations; therefore, the E01 and DH were selected as representatives from among the KHOA and KMA observation locations, and their data are shown as time series. It can be seen that there was no great difference between the simulation results that used the 3 parameter combinations UL1M4, UL2M2, and UL4M4, excluding DL1M1. However, as Table 5 shows, the results using the UL4M4 parameters, which produced the best statistics, had the largest significant wave height estimates, and these results were close to the observed values. In contrast, the results obtained using the DL1M1 parameters, which showed the worst model results in Table 4, estimated the waves to be lower than for other settings. Looking at the significant wave height results for December 23 and 24 at E01 and December 28 at DH in Fig. 6, the results obtained using the 3 parameter settings UL1M4, UL2M2, and UL4M4 all showed the significant wave heights to be approximately 0.1−0.2 m higher than when using DL1M1, regardless of the input wind data. However, looking at the results for December 22, when the observed significant wave height rapidly increased, the wave height estimated by the DL1M1 settings was the largest, contrary to the previous results. It is believed that this is because the DL1M1 parameter combination does not use the ST6, which employs the new

Table 5 Skill assessment of East Sea wave model results for significant wave height

				RDAPS				ERA5				JMA-MSM			
Location	n	Mean	Physics	Bias	RMSE	ρ	IOA	Bias	RMSE	ρ	IOA	Bias	RMSE	ρ	IOA
E01	2314	2.27	DL1M1	0.25	0.60	0.85	0.90	0.41	0.57	0.92	0.91	0.19	0.50	0.89	0.94
			UL1M4	0.10	0.53	0.86	0.92	0.25	0.44	0.93	0.94	0.03	0.42	0.90	0.95
			UL2M2	0.10	0.52	0.86	0.92	0.24	0.44	0.93	0.94	0.02	0.42	0.90	0.95
			UL4M4	0.06	0.50	0.87	0.93	0.20	0.41	0.93	0.95	-0.01	0.41	0.91	0.95
			Komen	0.26	0.59	0.85	0.90	0.37	0.52	0.93	0.92	0.18	0.45	0.90	0.94
E02	2246	2.14	DL1M1	0.13	0.57	0.82	0.90	0.36	0.51	0.91	0.91	0.06	0.47	0.88	0.93
			UL1M4	-0.01	0.51	0.84	0.91	0.21	0.39	0.92	0.94	-0.08	0.42	0.90	0.94
			UL2M2	-0.01	0.50	0.84	0.91	0.20	0.39	0.93	0.94	-0.08	0.42	0.90	0.94
			UL4M4	-0.03	0.49	0.84	0.92	0.16	0.37	0.93	0.95	-0.11	0.41	0.90	0.95
			Komen	0.15	0.53	0.83	0.90	0.32	0.46	0.92	0.92	0.06	0.40	0.90	0.95
DH	2228	2.06	DL1M1	0.35	0.50	0.91	0.92	0.58	0.74	0.85	0.80	0.28	0.53	0.86	0.90
			UL1M4	0.23	0.40	0.92	0.94	0.46	0.64	0.86	0.84	0.16	0.45	0.87	0.93
			UL2M2	0.23	0.39	0.92	0.94	0.46	0.64	0.86	0.84	0.16	0.44	0.87	0.93
			UL4M4	0.20	0.37	0.93	0.95	0.43	0.62	0.86	0.84	0.13	0.43	0.88	0.93
			Komen	0.35	0.47	0.93	0.92	0.52	0.68	0.87	0.82	0.26	0.48	0.88	0.91
PH	2112	1.92	DL1M1	0.33	0.61	0.78	0.84	0.52	0.67	0.86	0.78	0.11	0.55	0.76	0.89
			UL1M4	0.21	0.52	0.81	0.88	0.42	0.56	0.89	0.84	0.03	0.46	0.82	0.90
			UL2M2	0.21	0.51	0.82	0.89	0.41	0.55	0.89	0.84	0.03	0.45	0.82	0.90
			UL4M4	0.18	0.49	0.83	0.89	0.38	0.53	0.90	0.86	0.01	0.43	0.84	0.91
			Komen	0.30	0.55	0.82	0.86	0.45	0.59	0.89	0.83	0.12	0.44	0.84	0.90
URD	2416	2.17	DL1M1	0.26	0.60	0.84	0.89	0.44	0.59	0.90	0.89	0.25	0.51	0.89	0.92
			UL1M4	0.13	0.52	0.85	0.92	0.29	0.46	0.91	0.93	0.11	0.41	0.90	0.95
			UL2M2	0.13	0.51	0.85	0.92	0.28	0.46	0.92	0.93	0.10	0.41	0.90	0.95
			UL4M4	0.09	0.49	0.86	0.92	0.24	0.43	0.92	0.94	0.07	0.39	0.91	0.95
			Komen	0.27	0.57	0.85	0.90	0.40	0.54	0.92	0.90	0.24	0.45	0.90	0.93
UJ	2250	2.01	DL1M1	0.27	0.68	0.75	0.84	0.58	0.72	0.89	0.80	0.23	0.57	0.82	0.88
			UL1M4	0.16	0.58	0.79	0.87	0.45	0.60	0.91	0.86	0.11	0.48	0.85	0.91
			UL2M2	0.15	0.57	0.79	0.88	0.44	0.59	0.91	0.86	0.10	0.48	0.85	0.92
			UL4M4	0.13	0.55	0.80	0.89	0.41	0.56	0.92	0.87	0.08	0.46	0.86	0.92
			Komen	0.27	0.61	0.79	0.86	0.51	0.65	0.91	0.83	0.21	0.50	0.86	0.90

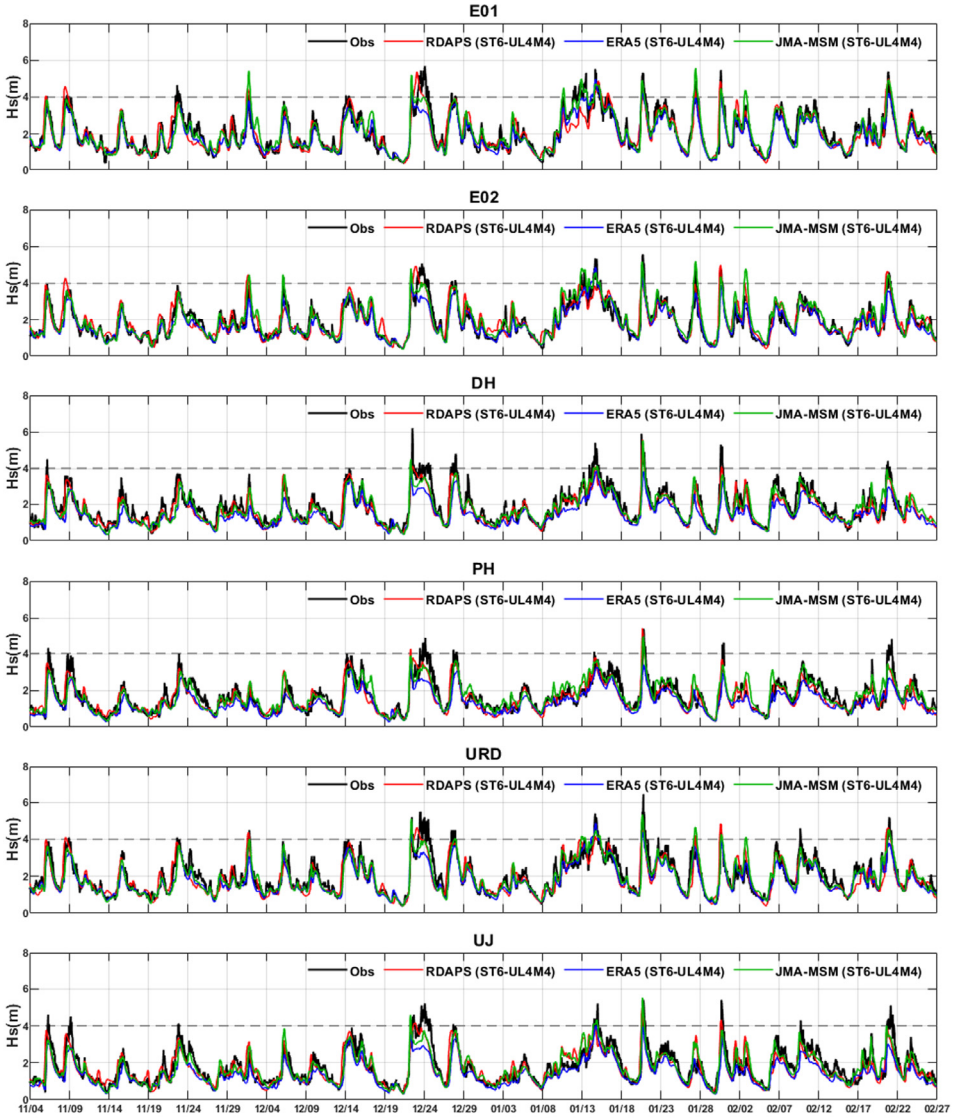

Fig. 5 Time series of observation data and ST6 (UL4M4) simulation results for significant wave height (Hs) using 3 input wind data sources (RDAPS, ERA5, and JMA-MSM) at 6 locations

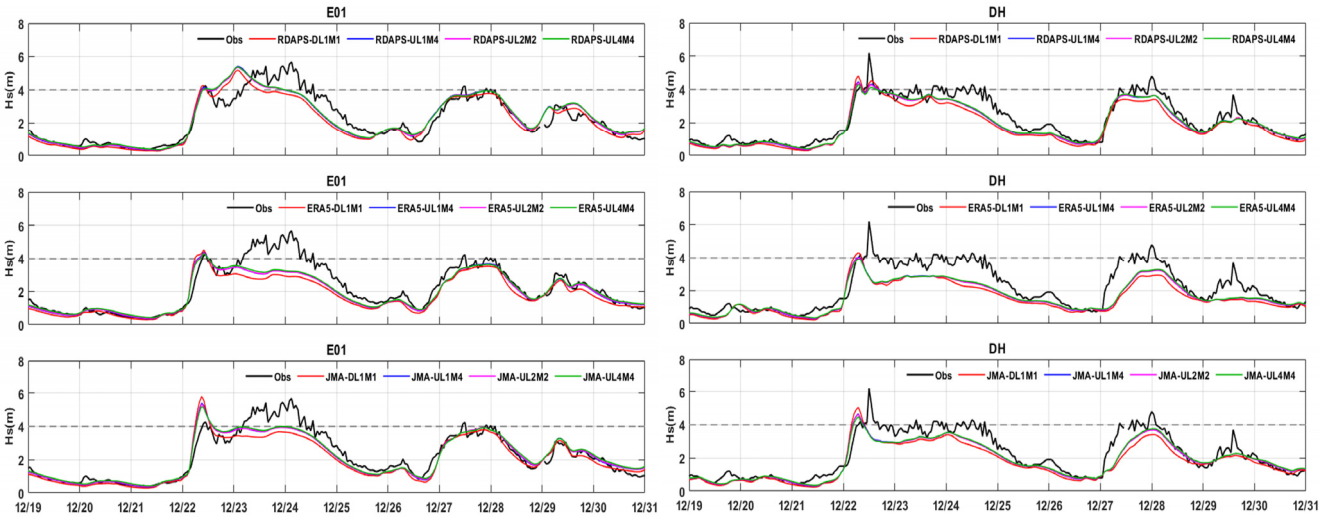

Fig. 6 Time series of observation data and ST6 simulation results for significant wave height (Hs) with 3 input wind data sources at E01 and DH (12.19.2016–12.31.2016)

value for calculating the coefficient of energy dissipation due to white-capping, and therefore DL1M1 shows somewhat different characteristics in the predicted process of wave development.

To analyze the simulation accuracy regarding wave period, Table 6 lists the statistics for error between the peak wave period results of this study's numerical wave model and the observation data. From the simulation result statistics, it can be seen that there was poor consistency in the statistical comparative analysis results for the four ST6 models (DL1M1, UL1M4, UL2M2, UL4M4) for each combination of input data and observing locations used, and it is difficult to distinguish the model with the best results. All of the peak wave period model results for the KMA observing location UJ had very poor reproducibility, with a correlation coefficient of less than 0.51. Fig. 7 shows the peak wave period simulation results at each observing location for the ST6 models that showed the best reproducibility for significant wave height (RDAPS/ERA5/JMA-MSM-UL4M4) along with the observation results in a time series. As can be seen in the figure, the model was not able to simulate the observed peak wave periods at UJ from December 20, 2016 to January 18, 2017. It is believed that an observation error occurred because the peak wave period values observed at UJ at that time were somewhat smaller than at other observing locations, and in the future, it will be necessary to examine the wave data quality management and data analysis methods to identify the cause of the error.

To examine the ST6's wave prediction improvement effect, this study compared ST6's simulation results to simulation results that use the empirical equation by Komen et al. (1984), which is the default setting for the SWAN model. Time series data for December 19 and

Table 6 Skill assessment of East Sea wave model results for peak wave period

				RDAPS				ERA5				JMA-MSM			
Location	n	Mean	Physics	Bias	RMSE	ρ	IOA	Bias	RMSE	ρ	IOA	Bias	RMSE	ρ	IOA
E01	2314	2.27	DL1M1	-0.31	0.95	0.82	0.89	-0.03	0.65	0.89	0.94	-0.54	0.96	0.86	0.89
			UL1M4	-0.42	0.97	0.82	0.88	-0.20	0.67	0.90	0.94	-0.67	1.02	0.87	0.88
			UL2M2	-0.38	0.95	0.82	0.89	-0.18	0.67	0.90	0.94	-0.64	1.00	0.87	0.88
			UL4M4	-0.40	0.94	0.83	0.89	-0.22	0.68	0.90	0.94	-0.67	1.01	0.87	0.88
			Komen	-0.45	0.97	0.83	0.88	-0.28	0.69	0.90	0.94	-0.73	1.06	0.87	0.87
E02	2246	2.14	DL1M1	-0.46	1.00	0.82	0.88	-0.22	0.72	0.89	0.93	-0.69	1.08	0.86	0.87
			UL1M4	-0.56	1.04	0.83	0.86	-0.39	0.78	0.89	0.92	-0.82	1.14	0.87	0.86
			UL2M2	-0.53	1.02	0.83	0.87	-0.36	0.77	0.88	0.92	-0.79	1.12	0.87	0.86
			UL4M4	-0.55	1.01	0.83	0.87	-0.40	0.79	0.89	0.92	-0.82	1.13	0.87	0.86
			Komen	-0.59	1.08	0.82	0.86	-0.46	0.83	0.89	0.91	-0.87	1.18	0.87	0.85
DH	2228	2.06	DL1M1	-0.09	1.10	0.79	0.88	0.20	1.31	0.72	0.84	-0.27	1.30	0.73	0.85
			UL1M4	-0.22	1.09	0.80	0.89	0.01	1.24	0.74	0.86	-0.44	1.31	0.74	0.85
			UL2M2	-0.20	1.08	0.80	0.89	0.02	1.23	0.75	0.86	-0.42	1.30	0.74	0.85
			UL4M4	-0.22	1.07	0.81	0.89	-0.02	1.22	0.75	0.86	-0.44	1.30	0.75	0.85
			Komen	-0.24	1.13	0.79	0.88	-0.03	1.26	0.75	0.86	-0.47	1.33	0.75	0.85
PH	2112	1.92	DL1M1	-0.13	1.45	0.68	0.81	0.21	1.24	0.78	0.88	-0.08	1.37	0.74	0.86
			UL1M4	-0.26	1.44	0.68	0.82	-0.03	1.23	0.78	0.88	-0.33	1.32	0.76	0.86
			UL2M2	-0.24	1.43	0.69	0.82	-0.02	1.22	0.78	0.88	-0.29	1.33	0.76	0.86
			UL4M4	-0.27	1.43	0.69	0.82	-0.06	1.23	0.77	0.87	-0.36	1.34	0.75	0.86
			Komen	-0.31	1.50	0.67	0.81	-0.07	1.24	0.78	0.88	-0.34	1.42	0.73	0.85
URD	2416	2.17	DL1M1	0.05	1.20	0.72	0.85	0.32	1.00	0.81	0.89	-0.18	1.11	0.77	0.87
			UL1M4	-0.06	1.17	0.73	0.86	0.15	0.95	0.82	0.90	-0.33	1.12	0.78	0.87
			UL2M2	-0.03	1.16	0.73	0.86	0.18	0.96	0.82	0.90	-0.29	1.11	0.78	0.87
			UL4M4	-0.05	1.15	0.74	0.86	0.14	0.94	0.82	0.90	-0.32	1.11	0.78	0.87
			Komen	-0.10	1.18	0.73	0.85	0.06	0.93	0.83	0.90	-0.39	1.13	0.79	0.88
UJ	2250	2.01	DL1M1	-0.72	2.23	0.36	0.61	-0.59	1.95	0.50	0.69	-0.98	2.24	0.42	0.64
			UL1M4	-0.85	2.25	0.37	0.61	-0.76	2.02	0.49	0.68	-1.11	2.29	0.43	0.63
			UL2M2	-0.83	2.24	0.37	0.61	-0.74	2.00	0.49	0.68	-1.09	2.28	0.43	0.63
			UL4M4	-0.86	2.23	0.38	0.61	-0.79	2.03	0.49	0.67	-1.12	2.29	0.43	0.63
			Komen	-0.87	2.26	0.38	0.61	-0.85	2.05	0.51	0.69	-1.16	2.30	0.45	0.64

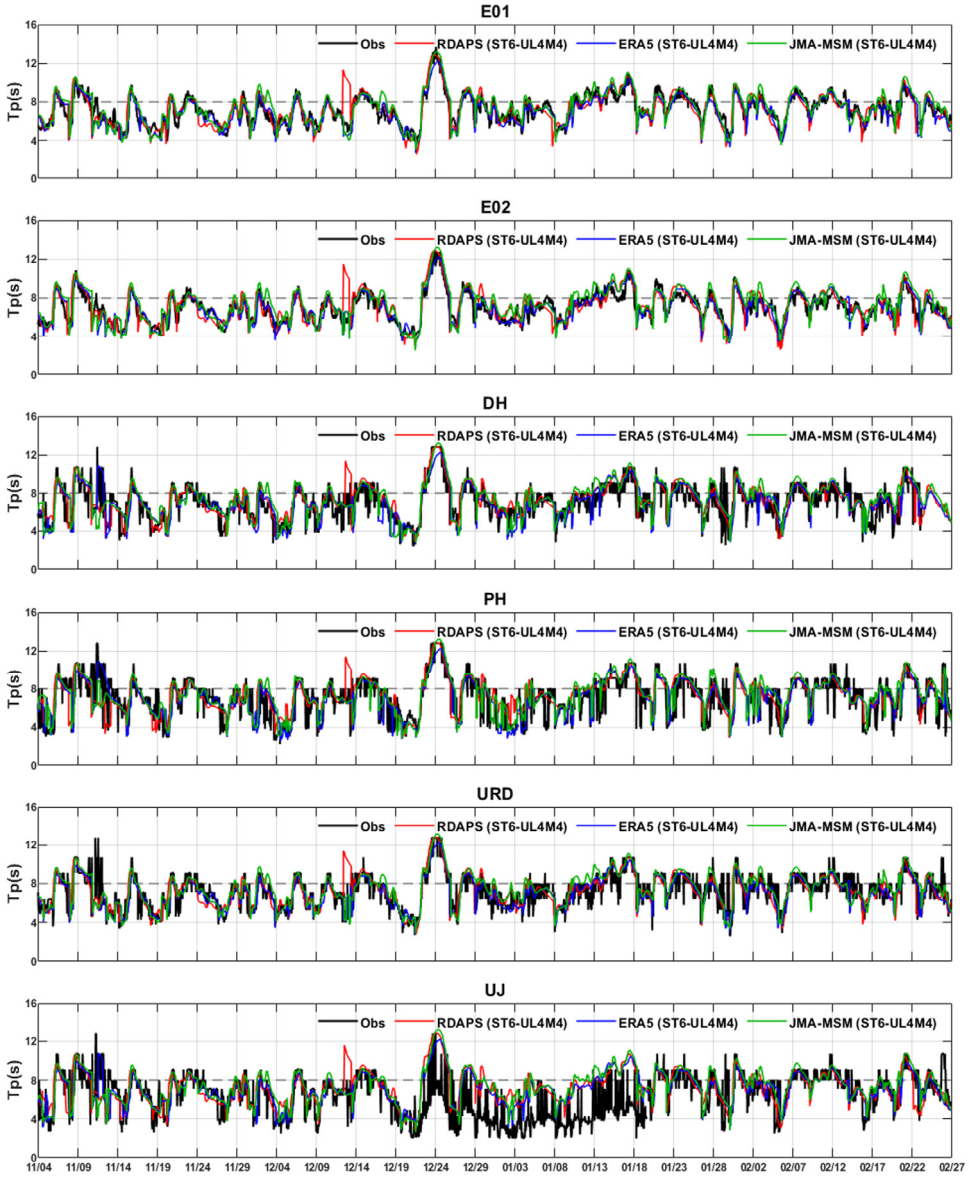

Fig. 7 Time series of observation data and ST6 (UL4M4) simulation results for peak wave period (Tp) using 3 input wind data sources (RDAPS, ERA5, and JMA-MSM) at 6 locations

31, 2016 at E01 and DH are shown in Fig. 8. It can be seen that the two simulation results show no great difference in terms of peak wave period; however, in the case of significant wave height, ST6 predicted the wave height to be somewhat higher overall compared to the results obtained using the empirical equation by Komen et al. (1984). The difference between the two methods' results is clear between December 22 and 24, when a large significant wave height occurred and temporal variability was high. Looking at the statistical analysis values listed in Table 4, it can be seen that RDAPS/ERA5/JMA-UL4M4 had an RSME that was lower by a maximum of 0.1 m and a lower deviation than RDAPS/ERA5/JMA-Komen, and the IOA and correlation coefficient were the same, or slightly higher for UL4M4. Thus, the simulation results using the empirical equation by Komen et al. (1984) were more accurate than the results of the ST6 using the DL1M1 setting; still, they were less accurate than when using the other settings, i.e., UL1M4, UL2M2, and UL4M4. This shows that, depending on the settings, the ST6 can predict significant wave height more accurately than the empirical equation by Komen et al. (1984). However, this study targeted only some periods when swell-like waves occurred. As such, it will be necessary to examine the numerical wave model's suitability for waves that occur in various weather conditions (large-height swell-like waves, storm waves, etc.), and it is believed that the wave prediction accuracy can be improved further by providing optimal parameters based on such an examination.

This study used various numerical simulation scenarios to find that the ST6's UL4M4 parameter setting had the highest reproducibility for large-height swell-like waves that occur on the East Sea. Ultimately, this study evaluated the accuracy of numerical wave models according to the input wind data provided different organizations. Fig. 9 shows

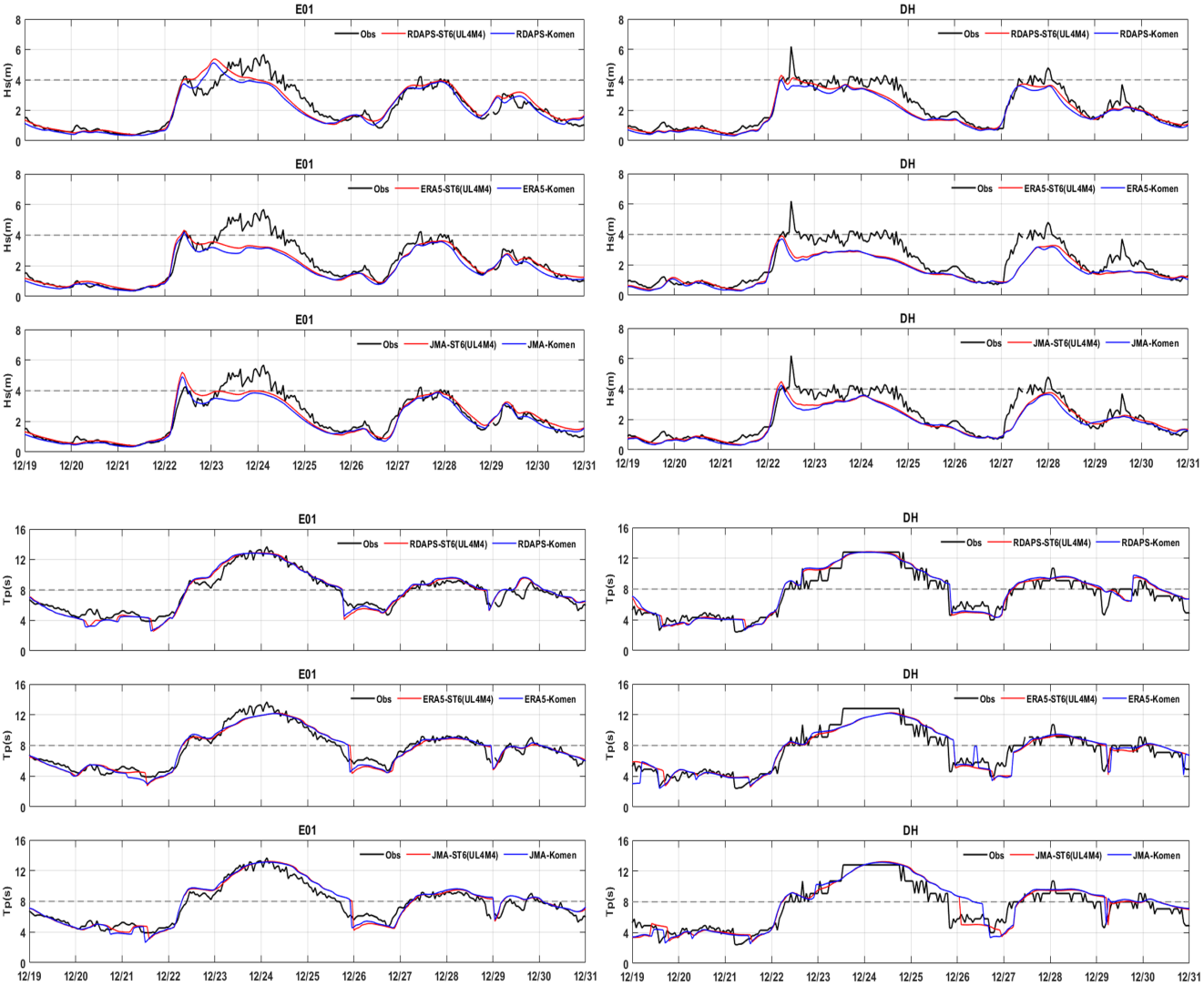

Fig. 8 Time series of observation data, ST6 (UL4M4) simulation results, and Komen et al. (1984) formula-based model prediction for significant wave height (Hs) and peak wave period (Tp) at E01 and DH (12.19.2016–12.31.2016)

bar graphs of the RMSEs and correlation coefficients of the significant wave height and peak wave period simulation results of the model with UL4M4 settings using the wind data provided by RDAPS, ERA5, and JMA-MSM. These graphs examine the accuracy of the numerical simulation of waves according to the input wind data. It can be seen that the simulation results for significant wave height using the ERA5 wind data as input had the highest correlation coefficient, except in the case of the location DH. This is because the ERA5 wind data were created through later re-analysis, unlike the other wind data, which shows that the accuracy of the input wind data plays an important role in the simulation of significant wave height. However, the ERA5 simulation results had a higher RMSE than the simulation results from JMA-MSM at all other locations except for E01 and E02, and they had a higher RMSE than the simulation results from RDAPS at the DH, PH, and UJ. It can be said that when the ERA5 wind data were used as the input wind data, the overall significant wave height reproducibility was excellent, but accuracy was poor when simulating large-height waves with great temporal variability. This can be seen in Fig. 6, which shows Fig. 5's simulation results in detail around both February 22 and December 24 at E01 and DH. The wind data provided by the ERA5 model are based on a global model, and while their temporal resolution is excellent compared to the RDAPS and JMA-MSM data, their spatial resolution is poor. Therefore, it is believed that the spatial resolution of the input wind data plays an important role in simulating hazardous large-height waves that rapidly increase and change during severe weather. Looking at the simulation results for peak wave period, except at the UJ, which had a correlation coefficient of less than 0.5, it can be seen that the lowest RMSE and highest correlation coefficient were obtained when using the ERA5 wind data, which had a high overall accuracy. Also, the RMSE for the peak wave period simulation results appears to be similar to the wind speed and wind direction RMSEs in Fig. 4, and it is believed that the accuracy of the wind speed and wind direction prediction has a large effect on predicting the periodic components of waves.

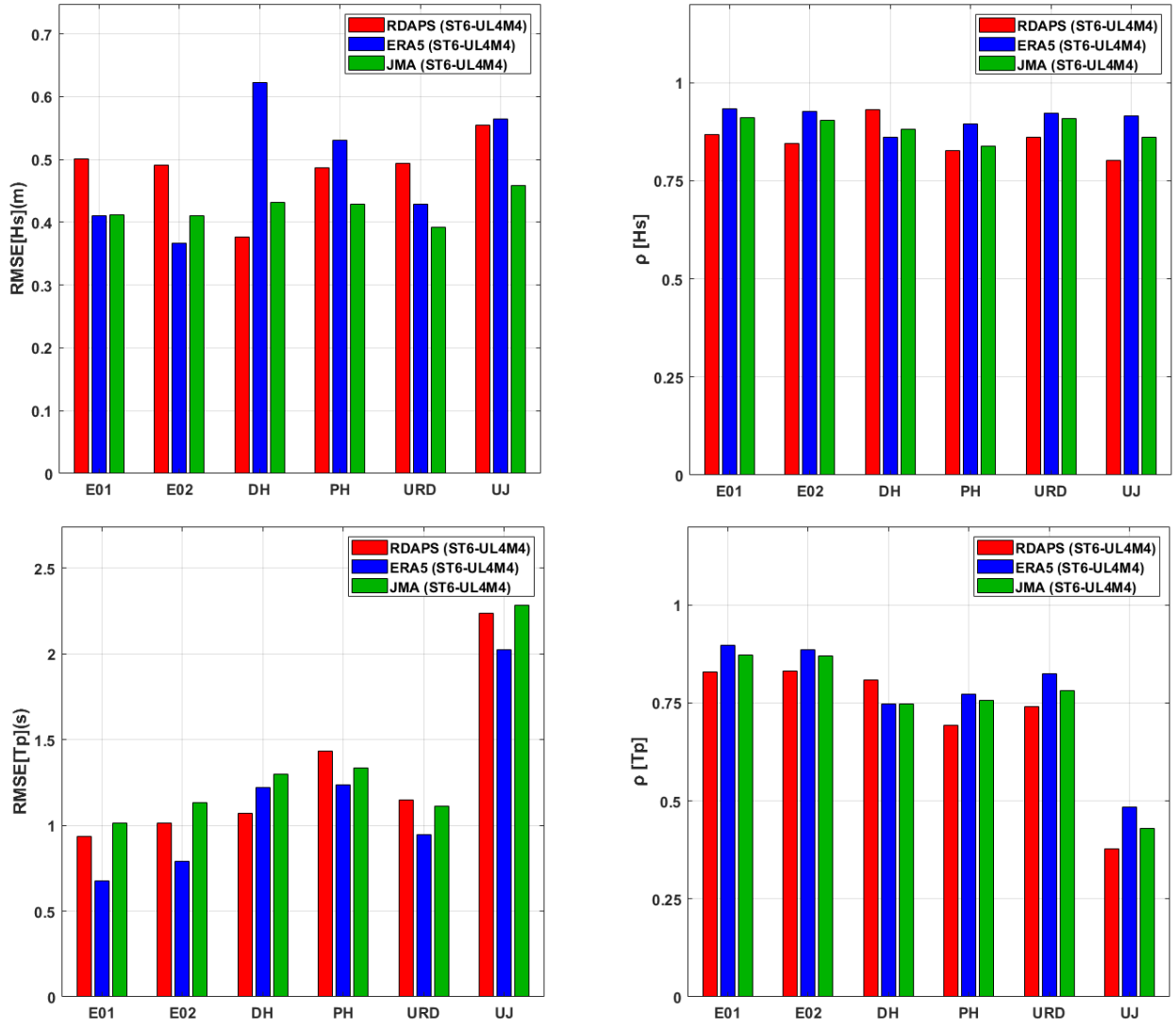

Fig. 9 Bar graphs of (a) RMSE and (b) correlation coefficient of wave simulation results for significant wave height (Hs) and peak wave period (Tp) during the simulation period (11.01.2016–02.28.2017)

5. Conclusions

This study used SWAN, a third-generation numerical wave model that is the most widely-used model in the field of coastal engineering, and ST6, which incorporates physical coefficients created based on observational research, to build and optimize a numerical wave model that can be applied to the East Sea during winter. To evaluate the reproducibility of the ST6, the numerical wave model was run using 4 different parameter combinations (DL1M1, UL1M4, UL2M2, and UL4M4) that were verified by Rogers et al. (2012) and spatial-temporal wind data (RDAPS, ERA5, and JMA-MSM) provided by various organizations as input, and the parameter settings with the best reproducibility were found. The results were compared to those obtained using the empirical equation by Komen et al. (1984), which is the default option in the SWAN model. In addition, a comparison was made between the simulation results obtained using the spatial-temporal wind data provided by each organization, and the reproducibility of the simulation results was evaluated according to the input wind data.

Looking at the ST6 models with the 4 different parameter settings, it was found that the significant wave height reproducibility was best when using the UL4M4 parameters, and it was possible to obtain higher reproducibility by adjusting the parameters compared to using the empirical equation by Komen et al. (1984). In the case of peak wave period, there was poor consistency in the results according to each model, observing locations, and evaluation item, and it was difficult to evaluate reproducibility. When looking at the simulation results obtained by using each organization's wind data, which had different characteristic, it was found that the best simulation results for significant wave height and peak wave period were obtained by using the ERA5 wind data. However, when predicting hazardous waves with great temporal variability, large wave heights were better simulated by

RDAPS and JMA-MSM wind data, which are forecast models with worse wind speed accuracy but better spatial resolution than ERA5. This confirmed that the input wind data's spatial resolution quality has a greater effect on wave prediction than wind speed accuracy when predicting large-height waves great temporal variability.

Ultimately, it was confirmed that ST6 can simulate the waves that occur in the East Sea to a certain extent by using various parameter settings instead of the empirical equation by Komen et al. (1984) used in existing numerical wave models. Also, it is believed that wind data with excellent spatial resolution quality are required to predict hazardous waves, which are characterized by large heights and occurrence during severe weather. Therefore, it will be possible to build a numerical wave model that can be applied to the entire East Sea by using a nesting method on the coastal areas. However, this study was not able to properly simulate significant wave heights that rapidly increased by more than 4 m and which occurred on December 19–31, 2016, January 8–18, 2017, or around February 21, 2017. There was an error of approximately 1 m in the simulation results for the location URD around January 20 and at locations DH, PH, and UJ around January 30. This means that third-generation numerical models, which calculate the wave energy spectrum using a wave action density equilibrium equation, are limited in predicting hazardous waves, such as storm waves and large-height swell-like waves that occur during typhoons and periods of severe weather. As such, it will be necessary to continue studying simulations for waves that occur in various environments, including severe weather conditions, and it will be necessary for data assimilation, which are used to increase prediction accuracy in the field of meteorology, to be applied to wave predictions to overcome the limitations of hazardous wave prediction.

Funding

This study was supported by a National Research Foundation of Korea grant funded by the Korea government (NRF-2019R1C1C 1003160), and by the project titled "Establishment of the Ocean Research Station in the Jurisdiction Zone and Convergence Research" funded by the Ministry of Oceans and Fisheries in Korea.

References

Booij, N., Ris, R.C., & Holthuijsen, L.H. (1999). A Third-generation Wave Model for Coastal Regions: 1. Model Description and Validation. Journal of Geophysical Research: Oceans, 104(C4), 7649–7666. https://doi.org/10.1029/98JC02622

Caires, S., Kim, J., & Groeneweg, J. (2018). Korean East Coast Wave Predictions by Means of Ensemble Kalman Filter Data Assimilation. Ocean Dynamics, 68, 1571–1592. https://doi.org/10.1007/s10236-018-1214-0

Chun, H., Kang, T.-S., Ahn, K., Jeong, W.M., Kim, T.-R., & Lee, D.H. (2014). A Study on the Statistical Characteristics and Numerical Hindcasts of Storm Waves in East Sea. Journal of Korean Society of Coastal and Ocean Engineers, 26(2), 81–95. https://doi.org/10.9765/kscoe.2014.26.2.81

Do, K., & Kim, J. (2018). A Study on the Predictability of Eastern Winter Storm Waves Using Operational Wind Forecasts of KMA. Journal of Korean Society of Coastal and Ocean Engineers, 30(5), 223–233. https://doi.org/10.9765/kscoe.2018.30.5.223

Eum, H.-S., Kang, T.-S., Nam, S.-Y., & Jeong, W.-M. (2016). Wave Modeling Considering Water Level Changes and Currents Effects. Journal of Korean Society of Coastal and Ocean Engineers, 28(6), 383–396. https://doi.org/10.9765/kscoe.2016.28.6.383

Hasselmann, K., Barnett, T.P., Bouws, E., Carlson, H., Cartwright, D.E., Enke, K., ... Walden, H. (1973) Erganzungsheft zur Deutschen Hydrographischen Zeitschrift, Reihe A (8°), 12, Hambur: Deutsches Hydrographisches Institut.

Jeong, W.-M., Oh, S.-H., Ryu, K.-H., Back, J.-D., & Choi, I.-H. (2018). Establishment of Wave Information Network of Korea (WINK). Journal of Korean Society of Coastal and Ocean Engineers, 30(6), 326–336. https://doi.org/10.9765/kscoe.2018.30.6.326

Kang, T.-S., Park, J.-J., & Eum, H.-S. (2015). Coastal Wave Hind-Casting Modelling Using ECMWF Wind Dataset. Journal of the Korean Society of Marine Environment and Safety, 21(5), 599–607. https://doi.org/10.7837/kosomes.2015.21.5.599

Kim, G.H., Ryu, K.H., & Yoon, S.B. (2020). Numerical Simulation of Storm Surge and Wave due to Typhoon Bolaven of 2012. Journal of Korean Society of Coastal and Ocean Engineers, 32(4), 273–283. https://doi.org/10.9765/kscoe.2020.32.4.273

Komen, G.J., Hasselmann, S., & Hasselmann, K. (1984). On the Existence of a Fully Developed Wind-sea Spectrum. Journal of Physical Oceanography,14(8), 1271–1285. https://doi.org/10.1175/1520-0485(1984)014<1271:OTEOAF>2.0.CO;2

Kwon, K.K., Jho, M.H., Ryu, K.H., & Yoon, S.B. (2020). Analysis of Reliability of Weather Fields for Typhoon Sanba (1216). Journal of Korean Society of Coastal and Ocean Engineers, 32(6), 465–480. https://doi.org/10.9765/kscoe.2020.32.6.465

Lee, B., & Ahn, S. (2018). Improved Reproducibility of the Yellow and East China Sea Wave Model by Adjusting Parameter of SWAN. Journal of the Korean Society for Marine Environment & Energy, 21(3), 207–215. https://doi.org/10.7846/jkosmee.2018.21.3.207

Lee, C., Ahn, S. J., Lee, B. W., Kim, S. W., & Kwon, S.J. (2014). Prediction of Swell-like High Waves Using Observed Data on the East Coast of Korea. Journal of Korean Society of Coastal and Ocean Engineers, 26(3), 149–159. https://doi.org/10.9765/kscoe.2014.26.3.149

Lee, H.S., Kim, K.O., Yamashita, T., Komaguchi, T., & Mishima, T. (2010). Abnormal Storm Waves in the Winter East/Japan Sea: Generation Process and Hindcasting Using an Atmosphere-wind Wave Modelling System. Natural Hazards and Earth System

Science, 10(4), 773−792. https://doi.org/10.5194/nhess-10-773-2010

Oh, S.-H., Jeong, W.M., Lee, D.Y., & Kim, S.I. (2010). Analysis of the Reason for Occurrence of Large- Height Swell-like Waves in the East Coast of Korea Analysis of the Reason for Occurrence of Large-Height Swell-like Waves in the East Coast of Korea. Journal of Korean Society of Coastal and Ocean Engineers, 22(2), 101−111.

Park, K.S., Heo, K.Y., Jun, K., Kwon, J.I., Kim, J., Choi, J.Y., ... Jeong, S.H. (2015). Development of the Operational Oceanographic System of Korea. Ocean Science Journal, 50(2), 353−369. https://doi.org/10.1007/s12601-015-0033-1

Rogers, W.E., Babanin, A.V., & Wang, D.W. (2012). Observation-consistent Input and Whitecapping Dissipation in a Model for Wind-generated Surface Waves: Description and Simple Calculations. Journal of Atmospheric and Oceanic Technology, 29(9), 1329−1346. https://doi.org/10.1175/JTECH-D-11-00092.1

Rogers, W.E., Hwang, P.A., & Wang, D.W. (2003). Investigation of Wave Growth and Decay in the SWAN Model: Three regional-scale Applications. Journal of Physical Oceanography, 33(2), 366−389. https://doi.org/10.1175/1520-0485(2003)033<0366:IOWGAD>2.0.CO;2

Saito, K., Fujita, T., Yamada, Y., Ishida, J.I., Kumagai, Y., Aranami, K., ... Yamazaki, Y. (2006). The Operational JMA Nonhydrostatic Mesoscale Model. Monthly Weather Review, 134(4), 1266−1298. https://doi.org/10.1175/MWR3120.1

WAVEWATCH III Development Group. (2016). User Manual and System Documentation of WAVEWATCH III Version 5.16 (Technical Note 329). USA: NOAA/NWS/NCEP/MMAB.

WAMDI Group. (1988). The WAM Model—A Third Generation Ocean Wave Prediction Model. Journal of Physical Oceanography, 18(12), 1775−1810. https://doi.org/10.1175/1520-0485(1988)018<1775:TWMTGO>2.0.CO;2

Yoon, S.B., Jeong, W.M., Jho, M.H., & Ryu, K.H. (2020). Analysis of Reliability of Weather Fields for Typhoon Maemi (0314). Journal of Korean Society of Coastal and Ocean Engineers, 32(5), 351−362. https://doi.org/10.9765/kscoe.2020.32.5.351

Zijlema, M., Van Vledder, G.P., & Holthuijsen, L.H. (2012). Bottom Friction and Wind Drag for Wave Models. Coastal Engineering, 65, 19−26. https://doi.org/10.1016/j.coastaleng.2012.03.002

Author ORCIDs

Author name	ORCID
Son, Bongkyo	0000-0002-6328-7286
Do, Kideok	0000-0001-7364-8375

KSOE

Journal of Ocean Engineering and Technology 35(4), 287-295, August, 2021
https://doi.org/10.26748/KSOE.2021.018

pISSN 1225-0767
eISSN 2287-6715

Original Research Article

Fault Classification of a Blade Pitch System in a Floating Wind Turbine Based on a Recurrent Neural Network

Seongpil Cho[1], Jongseo Park[2] and Minjoo Choi[3]

[1]*Senior Research Scientist, Alternative Fuels and Power System Research Center, Korea Research Institute of Ships and Ocean Engineering, Daejeon, Korea*
[2]*Graduate Student, Division of Naval Architecture and Ocean Systems Engineering, Korea Maritime and Ocean University, Busan, Korea*
[3]*Assistant Professor, Division of Naval Architecture and Ocean Systems Engineering, Korea Maritime and Ocean University, Busan, Korea*

KEY WORDS: Floating wind turbine, Blade pitch system, Fault diagnosis, Machine learning, Gated recurrent units

ABSTRACT: *This paper describes a recurrent neural network (RNN) for the fault classification of a blade pitch system of a spar-type floating wind turbine. An artificial neural network (ANN) can effectively recognize multiple faults of a system and build a training model with training data for decision-making. The ANN comprises an encoder and a decoder. The encoder uses a gated recurrent unit, which is a recurrent neural network, for dimensionality reduction of the input data. The decoder uses a multilayer perceptron (MLP) for diagnosis decision-making. To create data, we use a wind turbine simulator that enables fully coupled nonlinear time-domain numerical simulations of offshore wind turbines considering six fault types including biases and fixed outputs in pitch sensors and excessive friction, slit lock, incorrect voltage, and short circuits in actuators. The input data are time-series data collected by two sensors and two control inputs under the condition that of one fault of the six types occurs. A gated recurrent unit (GRU) that is one of the RNNs classifies the suggested faults of the blade pitch system. The performance of fault classification based on the gate recurrent unit is evaluated by a test procedure, and the results indicate that the proposed scheme works effectively. The proposed ANN shows a 1.4% improvement in its performance compared to an MLP-based approach.*

1. Introduction

Offshore wind turbines are prone to unexpected faults as they are often operated in a harsher environments compared to turbines on land. Accordingly, there has been a growing interest toward developing technologies for detecting and diagnosing faults in advance for the effective maintenance and operation of these turbines. Unexpected faults influence system components, actuators, sensors, and controllers, which may result in the inoperability of a turbine in case of serious failures. Moreover, faults can lead to economic losses by inducing changes in the system characteristics, operation safety, and power efficiency of a wind turbine. Maintenance costs account for approximately 25%–30% of the life-cycle cost of an offshore wind power plant (Dinwoodie et al., 2013), and therefore, the reliability of such a wind turbine is critical.

Among the components of an offshore turbine, the blade pitch system has the highest downtime and failure rate (Gayo, 2011; Carroll et al., 2016; NordzeeWind, 2010). A system fault affects the aerodynamic loads of a blade, the power generation output, and the behavior of substructures. Therefore, it is crucial to diagnose faults at the early stage in a blade pitch system to protect a turbine and prevent downtime of the entire system (Cho et al., 2018). Early fault diagnosis can reduce risks and prevent accidents by raising alarms at appropriate times, thus enabling wind power plant operators to effectively operate and maintain a turbine (Isermann, 2006). It can also prevent long-term damage to turbines and provide a reliable technological guarantee for the further development of the wind power generation industry.

Up to recently, classical fault diagnosis methods with statistical classification, approximation methods, and density-based methods has been used. Deep learning methods, which are a type of machine learning algorithm, have emerged in recent years; they have been used for learning or training the complex structures of an actual large-scale dataset continuously collected by sensors in various applications including computer vision, object classification, voice recognition,

Received 7 April 2021, revised 28 May 2021, accepted 8 June 2021
Corresponding author Minjoo Choi: +82-51-410-4304, minjoo.choi@g.kmou.ac.kr

natural language processing, and robots (Wason, 2018).

A method for diagnosing faults through a series of measurement data can be learned by applying a deep learning algorithm. When diagnosing faults in the components of a wind turbine, a machine learning-based method can detect state changes of a system. Such machine learning methods include wavelet analysis, Support vector machines (SVN), Bayesian networks, and artificial neural networks (ANNs) (Blanke et al., 2006). Faults have been detected and diagnosed using support vector machines (Santos et al., 2015; Zeng et al., 2013; Laouti et al., 2011) and fuzzy clustering methods (Badihi et al., 2014; Simani et al., 2014) based on data collected by various sensors such as force sensors, accelerometers, speed sensors, and tower tops located on the blade route as well as the generator of wind turbine control systems.

In particular, researchers have used use neural network theories based on multilayer perceptron (MLP) (Kusiak and Li, 2011; Wang et al., 2016; Zaher et al., 2009; Kusiak and Verma, 2012; Cho et al., 2021), convolutional neural networks (CNNs) (Bach-Andersen et al., 2015; Bach-Andersen et al., 2018), and autoencoders (AEs) (Dervilis et al., 2014; Jiang et al., 2017) in order to develop reliable fault diagnosis systems for the components of wind turbines including the main bearing, gearbox, and generator. In particular, Cho et al. (2021) used an MLP-based ANN technique to perform fault diagnosis of a blade pitch system. This technique is, however, unsuitable for processing time-series data during training, and therefore, a recurrent neural network (RNN) that is apt for processing time-series data is required. Among various RNNs that have been proposed, long-short term memory (LSTM) and gated recurrent unit (GRU) (Cho et al., 2014) techniques are considered to be suitable for processing time-series data as they are capable of linking previous information with the current task during training. The GRU used in this paper exhibits a level of performance similar to that of LSTM networks but can be trained at a faster speed owing to its simple architecture.

For the effective fault diagnosis of a blade pitch system in a floating wind turbine, this paper proposes a fault classification model that employs a GRU-based ANN, which is suitable for processing time-series data. The modeling and control techniques for a wind turbine are detailed in Section 2; the data collection procedure as well as the steps and structure of the proposed method are described in Section 3. In Section 4, the performance of the proposed algorithm is compared with that of conventional MLP models. Future research directions are discussed in the last section.

2. Modeling and Control Method of a Wind Turbine

2.1 Floating Wind Turbine Model

The floating wind turbine model in this paper is designed based on an NREL 5 MW offshore wind turbine, OC3-Hywind floater (spar-type), and three catenary mooring cables, as illustrated in Fig. 1 (Jonkman et al., 2009; Jonkman, 2010).

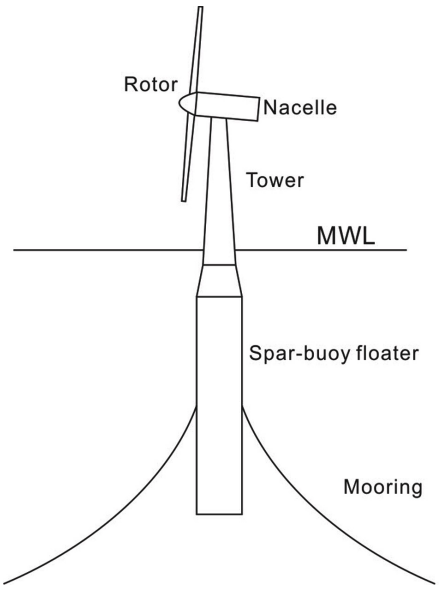

Fig. 1 Schematic view of a spar-type floating wind turbine (Cho et al., 2020)

2.2 Hydraulic Blade Pitch System

The hydraulic pitch system has a pump, fluid control valve, fluid reservoir, and a hydraulic cylinder (Cho et al., 2020). The hydraulic cylinder positioned in a turbine hub controls the blade pitch angle. The pump directly operates the cylinder using fluid pressure. The directional control valve effectively adjusts the flow rate and direction of the fluid into the cylinder, thus controlling the blade pitch angle. Fig. 2 shows the blade pitch system that consists of a pump with a certain level of pressure, a hydraulic cylinder, a directional control valve, an accumulator, and a fluid reservoir. In addition, an encoder and a linear variable differential transformer (LVDT) measure the blade pitch angle and valve spool position that are used as input variables of the controller.

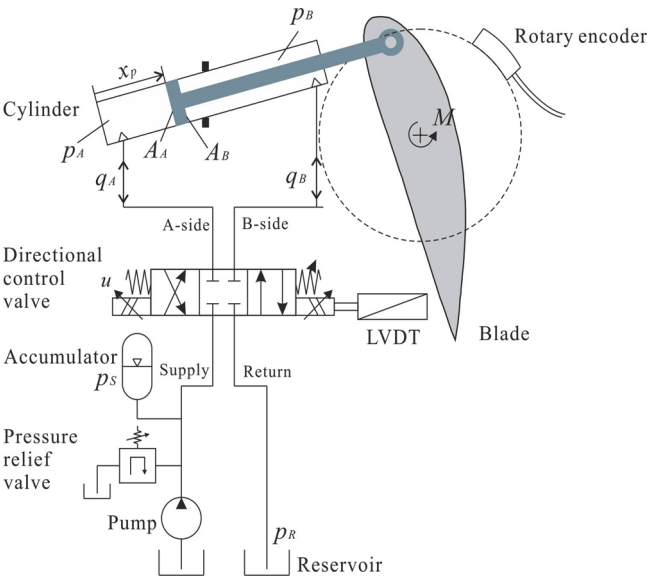

Fig. 2 Schematic view of a hydraulic blade pitch system (Cho et al., 2020)

2.3 Baseline Control System

The baseline control system comprises a generator torque and blade pitch controller (Cho et al., 2020). In the below-rated wind region, the torque controller regulates the generator torque in order to keep the optimal tip-speed ratio, thus generating the maximum power. The blade pitch controller controls the angle of the blade pitch to lower the aerodynamic forces applied on the blade while generating rated power in the above-rated wind region. A floating wind turbine can improve system response and reduce the motion of a floater by using a wind turbine controller.

The blade pitch angle β is determined by the position of the piston in the hydraulic cylinder x_p, based on the geometrical relationship explained in Eq. (1). Fig. 3 shows the geometrical relationship of the blade pitch system.

$$x_p(\beta) = \sqrt{L_p^2 + r_p^2 - 2L_p r_p \cos(\alpha_0 - \beta)} - l_p/2 \tag{1}$$

The position of the piston in the cylinder x_p is determined by the valve spool position x_{vs}, which is controlled by the control input voltage u_{vs} in Eq. (2). A proportional-integral controller (PI controller) is used in this case, wherein the directional control valve is effectively controlled by calculating the control input voltage u_{vs} after providing feedback on the piston position error $e(t)$, which is expressed using Eq. (3).

$$u_{vs}(t) = k_p\left(e(t) + \frac{1}{T_i}\int_0^t e(\tau)d\tau\right) \tag{2}$$

$$e(t) = (x_p(\beta) - x_p(\beta_C)) \tag{3}$$

Here, k_p is the proportional gain and T_i is the integral time. The valve spool position error $e(t)$ is determined by the function of the blade pitch angle β and the blade pitch command β_c of the pitch controller, as shown in Fig. 3. Detailed equations of the blade pitch system have been provided in a study by Cho et al. (2020).

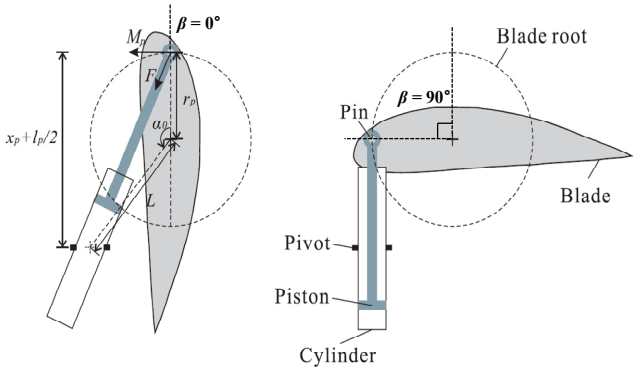

(a) (b)

Fig. 3 Geometry of the blade pitch actuator: (a) β = 0° and (b) β = 90° (Cho et al., 2020)

2.4 Fully Coupled Numerical Simulation

For the analysis of the dynamic response of a floating wind turbine, Simo-Riflex (SINTEF Ocean, 2018a; SINTEF Ocean, 2018b), an aero-hydro-servo-elastic simulation tool, was used to perform numerical simulations. Simo calculates the fluid dynamic force and moment applied to the substructures based on the potential flow theory and a Morison-type viscous drag force. Riflex performs an structural analysis of the blade, shaft, tower, and mooring system based on the finite element method (FEM). Moreover, Riflex also calculates the aerodynamic force and moment applied to the blade using the blade element momentum (BEM) theory. Thus, Simo-Riflex performs a numerical analysis linking the baseline control system based on structural dynamic, fluid dynamic, and aerodynamic models. Fig. 4 shows the data transmission between Simo-Riflex and the control algorithm.

Six ocean environmental load cases with related wind and wave conditions for simulations of dynamic responses of a floating wind turbine are presented in Table 1. In terms of wind loads, turbulence modeling was performed using TurbSim (Jonkman and Kilcher, 2012) based on the Kaimal turbulence model according to IEC 61400-1 (IEC, 2005a) and 3 (IEC, 2005b). For irregular wave loads, the JONSWAP spectrum was used (Hasselmann et al., 1973). Peak wave period (T_p) and significant wave height (H_s) were determined based on their correlation with the wind speed of the Statfjord field in the North Sea (Johannessen et al., 2002).

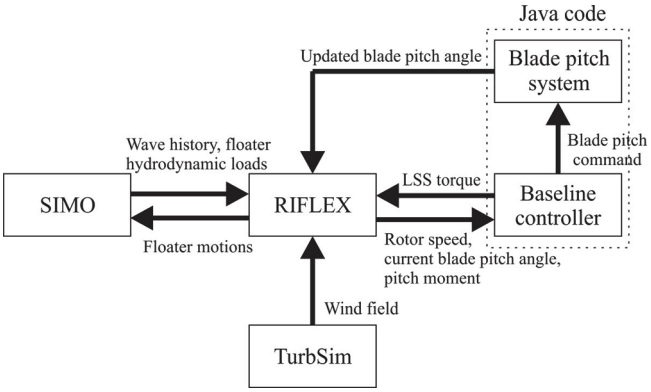

Fig. 4 Data transmission between Simo-Riflex and controller (Cho et al., 2020)

Table 1 Ocean environmental load cases based on winds and waves (Cho et al., 2021)

Load cases	U_w (m/s)	Turbulence model	H_s (m)	T_p (s)
1	14	IEC class C	3.58	10.27
2	16		3.97	10.44
3	17		4.17	10.53
4	19		4.58	10.72
5	20		4.8	10.82
6	22		5.23	11.02

3. Fault Classification Method

The first step of fault diagnosis is to discern the actual occurrence of a fault. In general, a model-based or signal-based detection method is used to discern the occurrence of a fault in a system. In particular, a model-based method can detect faults in real time by assessing the system status using a mathematical model. A typical model-based method involves using the Kalman filter often used in various fields such as global positioning systems, computer vision, and computer games. In a study by Cho et al. (2018), the Kalman filter was used to detect sensor and actuator faults of a blade pitch system in a floating wind turbine. If faults are successfully detected, a fault classification technique is required to classify the types of faults. In this paper, fault classification is performed under the assumption that faults are properly detected.

An ANN is used in this paper for classifying the faults of a floating wind turbine. The ANN extracts the features of each fault from the training data and learns their patterns to generate a prediction model, thus accurately classifying six types of faults. The forms of feature extraction for each type of fault are presented in a study by Cho et al. (2021). The proposed ANN consists of an encoder and a decoder and has the structure shown in Fig. 5. The encoder consists of an RNN; it is used to reduce data dimensionality while maintaining the features contained in the information of the input data. The decoder consists of MLPs; it is used to classify faults based on the processed data received from the encoder. More details on the encoder and the decoder are provided in Sections 3.3 and 3.4.

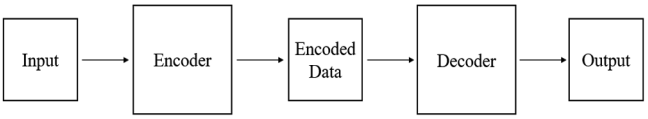

Fig. 5 Encoding-decoding process

3.1 Fault description of a Hydraulic Blade Pitch System

Faults in a blade pitch system can be classified into sensor and actuator faults. Faults in a sensor or an actuator cause a rotor imbalance and blade asymmetry. With respect to the faults in a pitch actuator, faults related to oil, valve, and sludge constitute a high percent (37.3%) of the total faults of a hydraulic pitch system (Carroll et al., 2016). Furthermore, a fault in the valve of a pitch actuator changes the system characteristics and affect the dynamic responses of a wind turbine in a transient or steady state conditions.

In this paper, six types of faults that occur in a pitch sensor and an actuator of a hydraulic blade pitch system are considered (Cho et al., 2021). Table 2 presents these different types of faults.

Faults in a blade pitch system can be classified into those occurring in a sensor and those occurring in a control valve in an actuator. Among pitch sensor faults, fault 1 refers to the case in which a consistent bias value is observed in a pitch sensor, while fault 2 refers to the case in which one value of a sensor is consistently repeated.

Table 2 Description of faults (Cho et al., 2021)

Fault number	Fault name	Fault occurrence location
1	Bias value	Pitch sensor
2	Fixed output	
3	Excessive friction	Directional control valve
4	Slit lock on spool	
5	Wrong voltage	
6	Short circuit	

A control valve fault is commonly caused by fluid contamination in a hydraulic actuator or problems in the filter. When excessive sludge is found in a valve spool, the clearance between the valve and spool is reduced, which results in increased frictional force. This is referred to as fault 3. Fault 4 occurs when the valve is locked due to the hardened sludge from fault 3.

Moreover, fault 5 occurs when excessive current is introduced due to a problem in the magnetic field of the valve solenoid, which leads to an incorrect voltage being applied to the solenoid. Fault 6 occurs when the solenoid is burned due to the excessive current. The fault phenomena are explained in detail by Cho et al. (2018) and Cho et al. (2020) using mathematical modeling and figures. The specific characteristics of fault phenomena are reflected in a simulation through mathematical modeling to obtain relevant data, which are then used to train the ANN.

3.2 Data

Fault data are required for training the ANN prior to performing fault classification. Fault data were generated using the Simo-Riflex (SINTEF Ocean, 2018a; SINTEF Ocean, 2018b) simulator. Different fault types (six types as presented in Table 2), ocean environmental load cases (six cases as presented in Table 1), and fault occurrence times (10 values) were combined to perform 360 times of simulations; multiple data were collected during one simulation session by varying the data collection starting time. The fault occurrence time was categorized into 10 values ranging from 75 s to 300 s at intervals of 25 s. A total of 116,330 data points were collected, which were then classified into training data (80,000), validation data (20,000), and test data (16,330). The validation data were used to evaluate the final model recording during training. The test data were used to evaluate the final performance check of the final model. One piece of data consists of data collected during 17 s from a randomly selected observation starting point as shown in Fig. 6. The time step of the simulation Δt_i was 0.1 s. Four pieces of data were collected per time step; these included including the blade pitch sensor, blade pitch command, valve spool position sensor, and valve control input values, as shown in Fig. 6.

The data were normalized as four different units were included in the data. In this paper, min–max normalization was performed as described in Eq. (4) in which outliers were excluded when determining

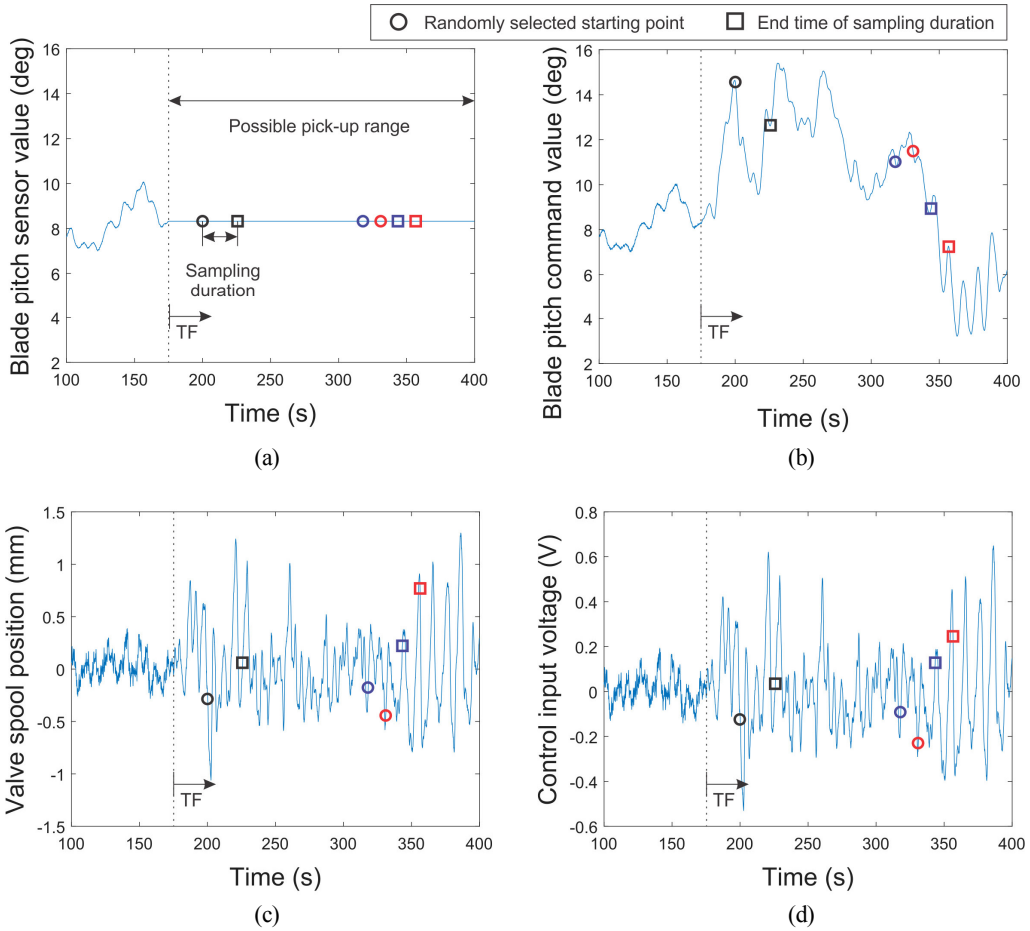

Fig. 6 Data sampling processes from simulations: (a) blade pitch sensor value, (b) blade pitch command value, (c) valve spool position, and (d) control input voltage (Cho et al., 2021)

the minimum and maximum values.

$$x_{i,normalized} = \frac{x_i - \min(x_i)}{\max(x_i) - \min(x_i)} \tag{4}$$

A label was represented with one-hot encoding, where one value is 1 and the remaining values are 0. Considering the labels used in this paper as an example, the data label related to fault type 1 has a vector value of [1 0 0 0 0 0].

One piece of data has a total of 686 values including 680 values collected from four data types ((1) blade pitch sensor value, (2) pitch command value, (3) valve spool position sensor value, and (4) valve control input value) for 17 s at intervals of 0.1 s, and six label values. Fig. 7 shows the constitution of 80,000 pieces of training data set. A

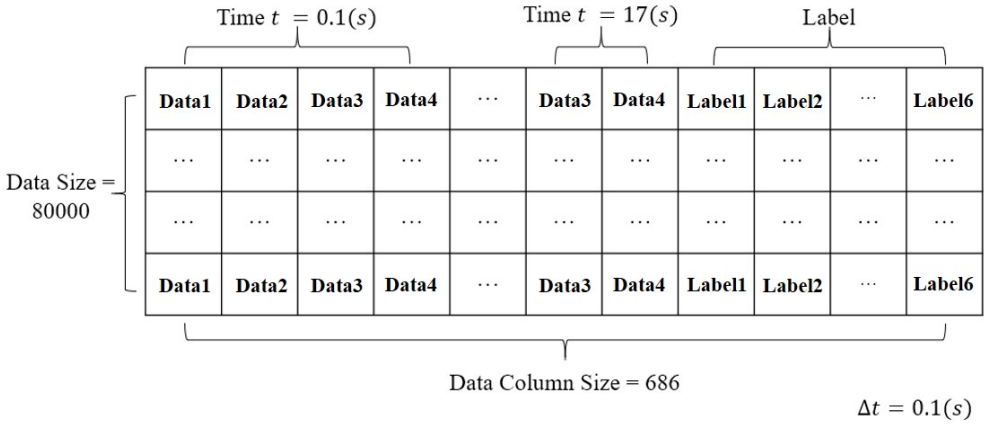

Fig. 7 Dimensions of training data according to blade pitch sensor value (data 1), blade pitch command value (data 2), valve spool position (data 3), and control input voltage (data 4)

GRU was employed by rearranging 680 pieces of data into 4 × 170 arrays.

3.3 Encoder

An encoder uses a GRU having a recursive connection structure and plays a role in reducing data dimensionality while maintaining the major features of time-series data. The GRU responds to the external input value of every time step and gradually updates a hidden state, which is an internal variable. The final hidden state generated preserves only the major features of the continuously input values in a compressed form, thus being capable of representing time-series data effectively. Effective data representation using a GRU reduces the size of the ANN and increases the efficiency of training the model. Eqs. (5)–(8) show the process of updating a hidden state.

$$r_t = \sigma(W_{ir}x_t + b_{ir} + W_{hr}h_{(t-1)} + b_{hr}) \tag{5}$$

$$z_t = \sigma(W_{iz}x_t + b_{iz} + W_{hz}h_{(t-1)} + b_{hz}) \tag{6}$$

$$n_t = \tanh(W_{in}x_t + b_{in} + r_t * (W_{hn}h_{(t-1)} + b_{hn})) \tag{7}$$

$$h_t = (1-z_t) * n_t + z_t * h_{(t-1)} \tag{8}$$

Here, h_t is the hidden state at time t, whereas x_t is the external input value at time t. h_{t-1} is the initial hidden state when time t is 0, or the hidden state at time $t-1$. Moreover, r_t, z_t, and n_t are the reset, update, and new gates, respectively. σ is the sigmoid function, while $*$ represents the Hadamard product. The above equation can be graphically represented as shown in Fig. 8.

If the number of data used for training is referred to as batch_size, the dimension of the input value for a decoder is batch_size × 170 × 4. If the size of the hidden state is referred to as hidden_size, the dimension of the output value, which is the set of hidden states generated during 170 time steps, is batch_size × 170 × hidden_size. In general, only the final hidden state, which is the last updated hidden state that best represents the features of all the values, is used. When the batch size is batch_size, the dimension of the final hidden state is batch_size × 1 × hidden_size.

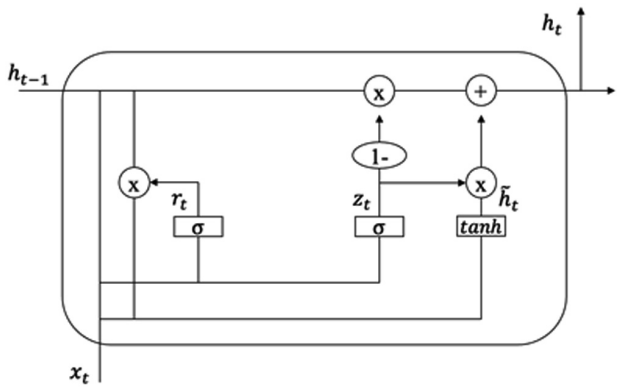

Fig. 8 Structure of a gated recurrent unit (Cho et al., 2014)

Considering one piece of data, the dimension of the input value for the encoder is 1 × 680 while the dimension of the output value is 1 × 80 if the hidden_size is 80. Specifically, the data size is reduced from 680 to 80. A comparison of the performance with respect to the reduction in dimensions is presented in Section 4.

3.4 Decoder

A decoder classifies faults when the final hidden state is input using an MLP. An MLP consists of an input layer, a hidden layer, and an output layer in that order, and output values are deduced through the matrix operations between each layer. In this study, the numbers of hidden layers and neurons (nodes in the hidden layer) were set to 1 and 100, respectively. The MLP used in this study is configured as shown in Fig. 9.

The ANN has a non-linear form between each layer of the MLP, and a rectified linear activation function (ReLU) is used to improve training efficiency. The ReLU returns 0 if the value is 0 or returns the value itself if greater than 0.

The output layer consists of six values, and the softmax function is used as the activation function. The softmax function creates all values to be between 0 and 1 and expresses the probability of their sum being 1. The decoder determines that a fault has occurred in the turn with the highest probability. For example, if the output values are 0.001, 0, 0.997, 0.0005, 0.001, and 0.0005, fault type 3, or excessive friction, is judged to have occurred because the third output is the largest.

The softmax cross-entropy function, often used in classification problems, was used as the loss function. Cross-entropy returns the loss value according to the difference between the predicted value and the answer, based on the value derived by the softmax function. The model was evaluated through the loss function and improved through optimization. The Adam optimizer based on a gradient descent was used as the optimization technique, and the learning rate was set to 0.01.

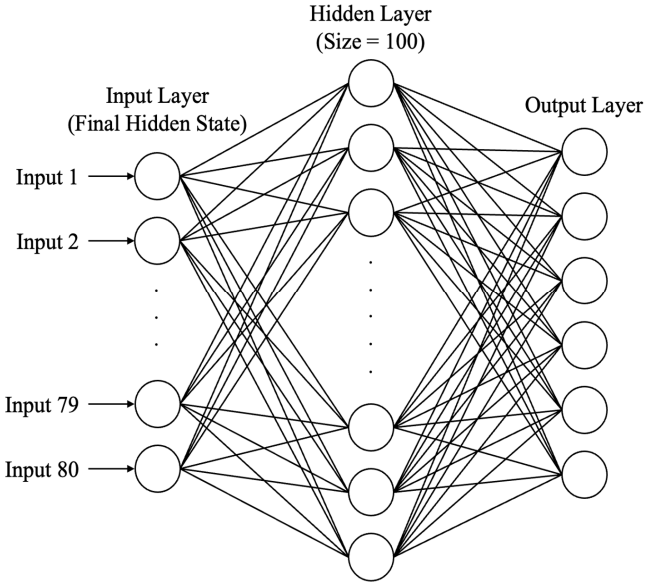

Fig. 9 Structure of the multilayer perceptron

4. Comparative Test

To determine the optimal hyperparameters of the ANN, its performance was compared by combining different hyperparameter values into sets as shown in Table 3. Overfitting occurred when the number of epochs exceeded 100; therefore, the final number of epochs was set to 100 in this study.

A total of nine hyperparameter sets were considered, and each set was trained 10 times for a total of 90 times. The performance of the ANN considering validation and test data with respect to each hyperparameter set is illustrated in Figs. 10 and 11, respectively. Its overall performance was fairly consistent, but the changes in its performance varied significantly depending on the learning rate and batch size.

Based on the results in Figs. 10−11, the average performance of the network using validation data and test data is presented in Figs. 12−13, respectively. The bar marked with slashes exhibits the best performance among the nine hyperparameter sets. The average success rate using validation data and test data in the second hyperparameter set is 99.927% and 99.612%, respectively; these values are the highest. Thus, the second hyperparameter set was adopted in this study.

Table 3 Hyper parameter sets

Set No.	Batch size	Hidden layer size	Hidden state size	Learning Rate
1	4000	100	80	0.01
2	2000	100	80	0.01
3	2000	100	80	0.001
4	2000	150	80	0.01
5	2000	250	80	0.01
6	2000	100	100	0.005
7	2000	100	80	0.01
8	1000	100	80	0.01
9	2000	100	60	0.01

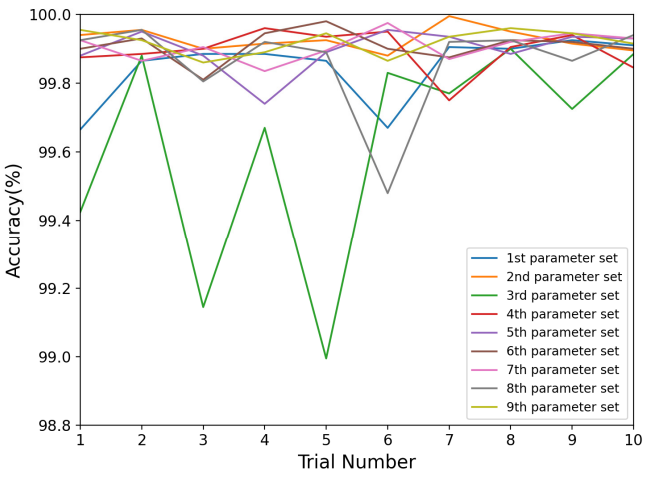

Fig. 10 Performance on validation data using different sets of hyperparameters

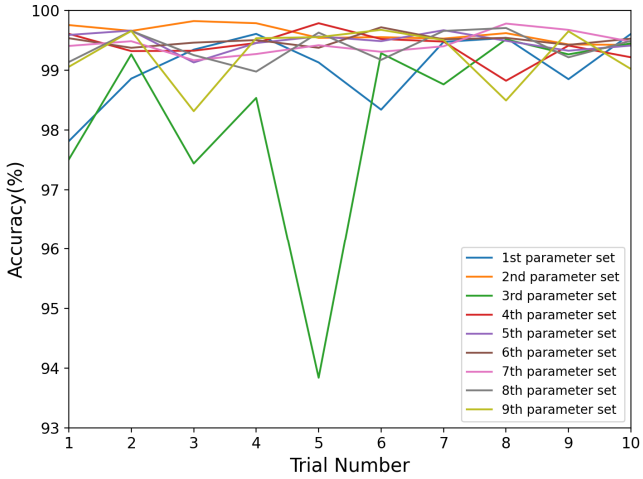

Fig. 11 Performance on test data using different sets of hyperparameters

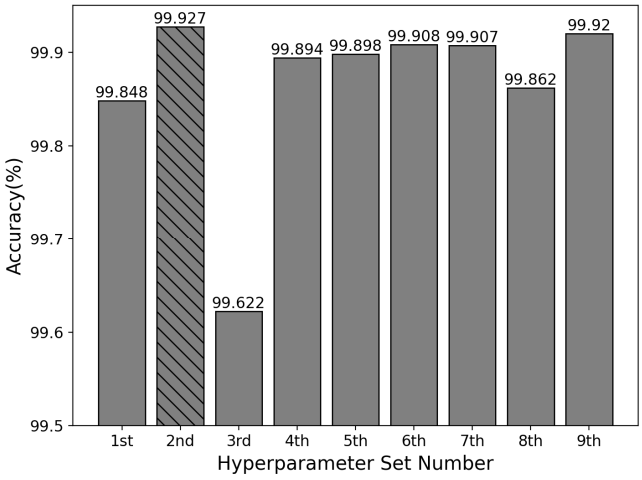

Fig. 12 Average performance on validation data using different sets of hyperparameters

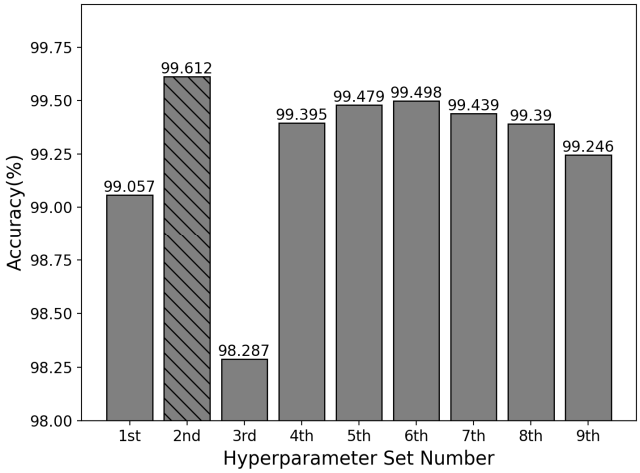

Fig. 13 Average performance on test data using different sets of hyperparameters

The proposed model could reduce the dimension of the input value from 680 to 80 as it used a GRU that could reflect the features of time-series data. Reducing the dimension of the input data facilitates

training by reducing the complexity of the ANN. The performance of the proposed model improved by approximately 1.4% in compared to the model proposed by Cho et al. (2021), which consisted only of MLPs using the same test data. The fault classification success rate is directly related to maintenance cost from the perspective of operating wind turbines and thus should be near 100%. Therefore, an increase of 1.4% in the success rate of fault classification using the GRU proposed in this paper implies almost 100% fault classification performance from the perspective of wind turbine operation, which is a significant improvement in fault classification.

5. Conclusion

This paper proposed a GRU based fault classification scheme of a blade pitch system in a floating wind turbine. GRU can quickly train a mathematical model based on previous training models and it processes time-series data by updating new information in real time. Based on various sets of hyperparameters, the proposed model achieved 99.927% and 99.612% successful classification on validation data and test data, respectively. The model also achieved a 1.4% improvement in its classification performance compared to other models that used MLP.

The proposed method only considered one type of fault that occurs independently in a system. In the future, the algorithm needs to be improved to be able to classify multiple faults occurring simultaneously. In addition, the proposed method should be applied to other components such as the generator, gearbox, and yaw system of a wind turbine.

Funding

This work was supported by “The development of a fully electrified car ferry and a removable power supply system (Project No. 20200469-01, PMS4700) funded by a national R&D project of the Ministry of Oceans and Fisheries. The authors gratefully would like to express our sincere gratitude for the research fund granted.

References

Bach-Andersen, M., Rømer-Odgaard, B., & Winther, O., (2015). Scalable Systems for Early Fault Detection in Wind Turbines: A Data Driven Approach. Proceedings of the Annual Conference of the European Wind Energy Association, Paris, France.

Bach-Andersen, M., Rømer-Odgaard, B., & Winther, O. (2018) Deep Learning for Automated Drivetrain Fault Detection. Wind Energy, 21(1), 29–41. https://doi.org/10.1002/we.2142

Badihi, H., Zhang, Y., & Hong, H. (2014). Wind Turbine Fault Diagnosis and Fault-Tolerant Torque Load Control Against Actuator Faults. IEEE Transactions on Control Systems Technology, 23(4), 1351–1372. https://doi.org/10.1109/TCST.2014.2364956

Blanke, M., Kinnaert, M., Lunze, J., Staroswiecki, M., & Schroder, J. (2006). Diagnosis and Fault-Tolerant Control (2nd ed.). Germany: Springer.

Carroll, J., McDonald, A., & McMillan, D. (2016). Failure Rate, Repair Time and Unscheduled O&M Cost Analysis of Offshore Wind Turbines. Wind Energy, 19, 1107–1119. https://doi.org/10.1002/we.1887

Cho, K.H., Merrienboer, B.V., Gulcehre, C., Bahdanau, D., Bougares, F., Schwenk, H., & Bengio, Y. (2014). Learning Phrase Representations using RNN Encoder-Decoder for Statistical Machine Translation. Proceedings of the 2014 Conference on Empirical Methods in Natural Language Processing, Doha, Qatar, 1724–1734. https://doi.org/10.3115/v1/D14-1179

Cho, S., Gao, Z., & Moan, T. (2018). Model-based Fault Detection, Fault Isolation and Fault-tolerant Control of a Blade Pitch System in Floating Wind Turbines. Renewable Energy, 120, 306–321. https://doi.org/10.1016/j.renene.2017.12.102

Cho, S., Bachynski, E.E., Nejad, A.R., Gao, Z., & Moan, T. (2020). Numerical Modeling of Hydraulic Blade Pitch Actuator in a Spar-type Floating Wind Turbine Considering Fault Conditions and Their Effects on Global Dynamic Responses. Wind Energy, 23(2), 370–390. https://doi.org/10.1002/we.2438

Cho, S., Choi, M.J., Gao, Z., & Moan, T. (2021). Fault Detection and Diagnosis of a Blade Pitch System in a Floating Wind Turbine Based on Kalman Filters and Artificial Neural Networks. Renewable Energy, 169, 1–13. https://doi.org/10.1016/j.renene.2020.12.116

Dervilis, N., Choi, M., Taylor, S.G., Barthorpe, R.J., Park, G., Farrar, C.R., & Worden, K. (2014). On Damage Diagnosis for a Wind Turbine Blade Using Pattern Recognition. Journal of Sound and Vibration, 333(6), 1833–1850. https://doi.org/10.1016/j.jsv.2013.11.015

Dinwoodie, I., McMillan, D., Revie, M., Lazakis, I., & Dalgic, Y. (2013). Development of a Combined Operational and Strategic Decision Support Model for Offshore Wind. Energy Procediam, 35, 157–166. https://doi.org/10.1016/j.egypro.2013.07.169

Gayo, J.B. (2011). Reliability-focused Research on Optimizing Wind Energy System Design, Operation and Maintenance: Tools, Proof of Concepts, Guidelines & Methodologies for a New Generation (FP7-Energy-2007-1-RTD). ReliaWind.

Hasselmann, K., Barnett, T.P., Bouws, E., Carlson, H., Cartwright, D.E., Enke, K., ... Meerburg, A., (1973). Measurements of Wind-wave Growth and Swell Decay During the Joint North Sea Wave Project (JONSWAP). Ergänzungsheft zur Deutschen Hydrographischen Zeitschrift, Reihe A, 12.

IEC (2005a). Wind Turbines — Part 1: Design Requirements (IEC 61400-1). International Electrotechnical Commission.

IEC (2005b). Wind Turbines — Part 3: Design Requirements for Offshore Wind Turbines (IEC 61400-3). International

Electrotechnical Commission.

Isermann, R. (2006). Fault-Diagnosis Systems: An Introduction from Fault Detection to Fault Tolerance. Germany: Springer.

Jiang, G., Xie, P., He, H., & Yan, J. (2017). Wind Turbine Fault Detection Using a Denoising Autoencoder with Temporal Information. IEEE/ASME Transactions on Mechatronics, 23(1), 89−100. https://doi.org/10.1109/TMECH.2017.2759301

Johannessen K, Meling T.S., Haver S. (2002). Joint Distribution for Wind and Waves in the Northern North Sea. International Journal of Offshore and Polar Engineering, 12(1), ISOPE-02-12-1-001.

Jonkman, J., Butterfield, S., Musial, W., & Scott, G. (2009). Definition of a 5-MW Reference Wind Turbine for Offshore System Development (Technical Report NREL/TP-500-38060). USA: National Renewable Energy Lab.

Jonkman, J. (2010). Definition of the Floating System for Phase IV of OC3 Technical Report NREL/TP-500-47535 USA.

Jonkman, J., & Kilcher, L. (2012). TurbSim User's Guide Technical Report NREL USA.

Kusiak, A., & Li, W. (2011). The Prediction and Diagnosis of Wind Turbine Faults. Renewable Energy, 36(1), 16−23. https://doi.org/10.1016/j.renene.2010.05.014

Kusiak, A., & Verma, A. (2012). Analyzing Bearing Faults in Wind Turbines: A Data-mining Approach. Renewable Energy, 48, 110−116. https://doi.org/10.1016/j.renene.2012.04.020

Laouti, N., Sheibat-Othman, N., & Othman, S. (2011). Support Vector Machines for Fault Detection in Wind Turbines. Proceedings of 18th IFAC World Congress, Milano, Italy, 44(1), 7067−7072. https://doi.org/10.3182/20110828-6-IT-1002.02560

NordzeeWind. (2010). Operations Report 2009 (Technical Report OWEZ_R_000_20101112). NordzeeWind.

Santos, P., Villa, L.F., Reñones, A., Bustillo, A., & Maudes, J. (2015). An SVM-based Solution for Fault Detection in Wind Turbines. Sensors, 15(3), 5627−5648. https://doi.org/10.3390/s150305627

SINTEF Ocean. (2018a). SIMO 4.15.0 User Guide.

SINTEF Ocean. (2018b). RIFLEX 4.14.0 User Guide.

Simani, S., Farsoni, S., & Castaldi, P. (2014). Fault Diagnosis of a Wind Turbine Benchmark via Identified Fuzzy Models. IEEE Transactions on Industrial Electronics, 62(6), 3775−3782. https://doi.org/10.1109/TIE.2014.2364548

Wang, L., Zhang, Z., Long, H., Xu, J., & Liu, R. (2016). Wind Turbine Gearbox Failure Identification with Deep Neural Networks. IEEE Transactions on Industrial Informatics, 13(3), 1360-1368. https://doi.org/10.1109/TII.2016.2607179

Wason, R. (2018). Deep Learning: Evolution and Expansion. Cognitive Systems Research, 52, 701−708. https://doi.org/10.1016/j.cogsys.2018.08.023

Zaher, A., McArthur, S.D.J., Infield, D.G., & Patel, Y. (2009). Online Wind Turbine Fault Detection Through Automated SCADA Data Analysis. Wind Energy, 12(6), 574−593. https://doi.org/10.1002/we.319

Zeng, J., Lu, D., Zhao, Y., Zhang, Z., Qiao, W., & Gong, X. (2013). Wind Turbine Fault Detection and Isolation Using Support Vector Machine and a Residual-based Method. 2013 American Control Conference, Washington, DC, USA, 3661−3666. https://doi.org/10.1109/ACC.2013.6580398

Author ORCIDs

Author name	ORCID
Cho, Seongpil	0000-0002-6613-4592
Park, Jongseo	0000-0003-2706-2802
Choi, Minjoo	0000-0001-6797-0210

KSOE

Journal of Ocean Engineering and Technology 35(4), 296-304, August, 2021
https://doi.org/10.26748/KSOE.2021.020

pISSN 1225-0767
eISSN 2287-6715

Original Research Article

Numerical Analysis of Wave Energy Extraction Performance According to the Body Shape and Scale of the Breakwater-integrated Sloped OWC

Hyunjai Yang[1], Eun-Hong Min[1] and WeonCheol Koo[2]

[1]*Graduate Student, Department of NAOE, Inha University, Incheon, Korea*
[2]*Professor, Department of NAOE, Inha University, Incheon, Korea*

KEY WORDS: Sloped oscillating water column, Wave energy converter, Numerical wave tank, Boundary element method, Wave energy extraction

ABSTRACT: *Research on the development of marine renewable energy is actively in progress. Various studies are being conducted on the development of wave energy converters. In this study, a numerical analysis of wave-energy extraction performance was performed according to the body shape and scale of the sloped oscillating water column (OWC) wave energy converter (WEC), which can be connected with the breakwater. The sloped OWC WEC was modeled in the time domain using a two-dimensional fully nonlinear numerical wave tank. The nonlinear free surface condition in the chamber was derived to represent the pneumatic pressure owing to the wave column motion and viscous energy loss at the chamber entrance. The free surface elevations in the sloped chamber were calculated at various incident wave periods. For verification, the results were compared with the 1:20 scaled model test. The maximum wave energy extraction was estimated with a pneumatic damping coefficient. To calculate the energy extraction of the actual size WEC, OWC models approximately 20 times larger than the scale model were calculated, and the viscous damping coefficient according to each size was predicted and applied. It was verified that the energy, owing to the airflow in the chamber, increased as the incident wave period increased, and the maximum efficiency of energy extraction was approximately 40% of the incident wave energy. Under the given incident wave conditions, the maximum extractable wave power at a chamber length of 5 m and a skirt draft of 2 m was approximately 4.59 kW/m.*

1. Introduction

Climate change has triggered the increase in the global temperature and subsequent sea level rise, causing significant damage, including drought, flood, and cold-weather damages. As part of multilateral cooperation and efforts to address the aforementioned problems, active international responses against climate change have materialized into the United Nations Framework Convention on Climate Change, Kyoto Protocol, and Paris Agreement. In line with the global trend, Korea has established a national target to reduce greenhouse gas (GHG) emissions by 2030, based on the principle of the nationally determined contribution (NDC) (Heo, 2016; Bae, 2021).

Accordingly, to reduce GHG emissions, there has been active research on new and renewable energy worldwide. Wave energy is an energy source with the highest energy density per unit area among marine energy sources, and is a highly promising resource that enables infinite sustainability with substantial potential. However, there are limitations to the utilization of wave energy: wave energy is subject to severe levels of seasonal and climatic variability, its various energy extraction methods and equipment are still under development, and a standardized power generation model for wave energy is yet to be established. The development of wave energy converters (WECs) has experienced steady advancements globally, and for some wave energy models, considerable progress has been made in commercialization, especially in the UK. Therefore, there is a significant demand for more active R&D, including more research ideas and technical progress, as well as the commercialization and development of maintenance and operation methods.

The European Marine Energy Center Limited (EMEC), a world-leading marine energy research and development center in the UK, categorized WECs into oscillating water column (OWC), movable body type, and overtopping/terminator type WECs, according to the type of their primary energy conversion (EMEC, 2018). Among the various types of WEC, OWC is a method in which incident waves trigger the movement of the water surface inside the air chamber, which then causes the resulting surface elevation to generate airflow;

Received 3 May 2021, revised 14 June 2021, accepted 14 July 2021
Corresponding author Weoncheol Koo: +82-32-860-7348, wckoo@inha.ac.kr

then, the generated airflow rotates the air turbine to extract energy. This generation method may be less efficient compared to the methods of converting wave energy into primarily usable energy; however, it has the advantage of easy maintenance because the air turbine for energy extraction is located above the water surface.

The OWC WEC can be divided into fixed and floating types, depending on the motion constraints of the structure. Various studies have been conducted on the fixed OWC WEC discussed in this study, and the findings of recent existing works have been reviewed in brief.

Koo et al. (2010) simulated the flow inside the OWC chamber of a general vertical chamber WEC using the 2D fully nonlinear numerical wave tank method. In addition, they analyzed the wave energy conversion efficiency in the time domain. Through the 2D wave tank experiment, the research was conducted with varying shape parameters of the chamber (ratios of the chamber and duct sizes) (Koo et al., 2012). Liu et al. (2010) compared the numerical results of 2D OWC WEC based on Desingularized boundary integral equation method (DBIEM) using the mixed Eulerian-Lagrangian method and the analytic results obtained by Sarmento and Falcao (1985). Subsequently, they analyzed the energy extraction efficiency according to the skirt draft of the structure. A number of studies have also been reported to analyze OWC WEC via the higher-order boundary element method (HOBEM), which considers the nonlinearity of each boundary element (Ning et al., 2015; Ning et al., 2020). Ning et al. (2016) compared the results of numerical analysis using HOBEM and the results obtained from water tank experiments. Kim et al. (2021) calculated the energy extraction efficiency of OWC WEC by applying the air damping coefficient in the chamber obtained by the theoretical solution, and compared their results with the results of previous studies with the application of the air damping coefficient.

In recent years, studies have been conducted on a sloped chamber WEC that can be installed via the connection to a breakwater built in a port or coast, by modifying a general vertical wall-type OWC. The sloped OWC has an energy extraction performance similar to that of the vertical OWC device, and its installation on the slope of the bottom-mounted breakwater, the existing onshore structure, is advantageous. As a recent study on the sloped OWC chamber, Park, et al. (2018b) measured the relative wave elevation inside the chamber, according to the change in skirt and width of a sloped OWC chamber, via a 2D wave tank experiment. In addition, by performing computational fluid dynamics (CFD) analysis, the wave elevation was calculated in two OWC chamber conditions: one with the chamber open, where the chamber pneumatic pressure is equal to the atmospheric pressure, and the other where the duct is installed above the chamber, such that chamber pneumatic pressure exists. The results obtained from the calculations were compared with those of the 2D water tank experiment. Via CFD analysis (using FLUENT), Gaspar et al. (2020) compared wave shapes inside vertical and 40°-sloped chambers. In the sloped chamber, run-up/down and sloshing were more dominantly observed than in the vertical chamber, and it was verified that the energy extraction efficiency of the sloped chamber was higher than that of the vertical chamber in terms of the wave period with the highest energy source.

The backward bent duct buoy (BBDB) type WEC is well-known as the floating OWC WEC. To examine the validity of the numerical modeling pneumatic damping coefficient, Kim et al. (2006) conducted a model test and measured the motion responses of BBDB in waves. In addition, the improvement in energy extraction efficiency was investigated by proposing a BBDB with rounded corners, which can reduce the viscous effect, via 2D wave tank experiments and numerical wave tank calculations (Kim et al., 2012; Lee et al., 2013; Kim et al., 2015).

In this study, a 2D fully nonlinear numerical wave tank method based on potential flow for a sloped-fixed OWC WEC was developed. Using the mixed Eulerian-Lagrangian method, numerical simulation was performed on the time domain for the nonlinear wave motion of the free surface inside and outside the sloped chamber. To consider the viscous effect in the analysis of potential flow based on non-viscous fluid, a viscous damping coefficient was added to the free surface boundary condition, and the flow change inside the chamber was calculated, considering the interactions with pneumatic pressure generated because of the free surface elevations in the OWC chamber, following the installation of a duct at the top of the chamber. The numerical results of this study were compared to the experimental results of previous studies (Park et al., 2018a, 2018b) to ensure reliability. The validated fully nonlinear numerical wave tank method can be calculated by selecting linear or nonlinear time domain analysis, and the proposed numerical method has the advantage of being relatively fast to obtain calculations, without having to conduct experiments for the investigation of wave steepness effect on the nonlinearity of the free surface. Using this study, each energy component of the sloped OWC WEC was calculated and compared with the incident wave energy, and it was verified that the energy of the entire WEC system was conserved. Finally, to elucidate the energy extraction and efficiency of the sloped OWC in the environment of real seas, the model size was increased by approximately 20 times, and the resulting changes in the viscous damping coefficient of the chamber were comparatively analyzed.

2. Mathematical Formulation

In this study, numerical modeling was performed for a sloped fixed OWC WEC, with the assumption that the fluid in the computational domain was an inviscid, incompressible, and irrotational potential fluid. The velocity potential representing the ideal fluid flow is defined as expressed in Eq. (1).

$$V = \nabla \phi \tag{1}$$

where V and ϕ denote the velocity of the fluid particle and velocity potential, respectively. The velocity potential can easily represent a complex fluid flow phenomenon as a scalar value, and when the fluid

flow satisfies the continuity equation and is an incompressible flow, the governing equation of the fluid domain can be represented using the Laplace equation:

$$\nabla^2\phi = 0 \tag{2}$$

The Laplace equation can be expressed as a boundary integral equation using Green's 2nd identity, as expressed in Eq. (3).

$$\alpha\phi_i = \iint_{\Omega} \left(G_{ij}\frac{\partial\phi_j}{\partial n} - \phi_j\frac{\partial G_{ij}}{\partial n} \right) ds \tag{3}$$

where Ω denotes the fluid domain in which the calculation is performed. The solid angle α at the boundary is 0.5, and the two-dimensional Green's function is $G_{ij} = -(1/2\pi)\ln R_1$. Here, R_1 represents the distance between the source point and the field point at the boundary of the computation domain.

The free surface boundary condition is divided into two: kinematic and dynamic conditions, and it can be expressed as a nonlinear free surface boundary equation by taking the total derivative ($\delta/\delta t$). In addition, under the assumption that the node points located on the free surface move in the same manner as the water particles (Material node approach, $\vec{\nu} = \nabla\phi$), they can be defined as expressed in Eqs. (4) and (5).

$$\frac{\delta\eta}{\delta t} = \frac{\partial\phi}{\partial z} \tag{4}$$

$$\frac{\delta\phi}{\delta t} = -g\eta + \frac{1}{2}|\nabla\phi|^2 - \frac{P_a}{\rho} \tag{5}$$

where η, g, ρ, and P_a denote the free surface elevation, gravity, fluid density, and pneumatic pressure on the free surface, respectively. Outside the chamber, the pneumatic pressure is zero, based on atmospheric pressure, and when pneumatic pressure is present inside the chamber, its value changes in real time, according to the volume of the OWC chamber and the size of the nozzle (duct).

For the boundary condition of the incident wave, the propagating wave was generated by substituting the incident wave component into the boundary surface at the left end of the numerical wave tank, and the impermeable rigid boundary condition of Eq. (6) was applied to the boundary conditions of the tank bottom, right wall, and fixed structure. This indicates that the fluid velocity in the direction perpendicular to the boundary is zero.

$$\frac{\partial\phi}{\partial n} = 0 \tag{6}$$

When the incident wave enters inside the OWC chamber, energy loss occurs at the end of the chamber skirt owing to fluid viscosity. Considering this energy loss, in general, the equation for reduced pressure in the flow, which is proportional to the square of the fluid velocity, is expressed in Eq. (7).

$$\triangle P = K_L\frac{1}{2}\rho\tilde{V}^2 \tag{7}$$

where K_L and $\tilde{V}$ represent the loss coefficient and flow velocity, respectively. This equation can be expressed as Eq. (8), under the assumption that the water particle velocity ($\partial\phi/\partial n$) is linearly proportional to the average vertical velocity of the water column ($\bar{\dot{\eta}}$). The viscous damping effect, which can occur when the incident wave enters the chamber, can be represented using the viscous damping coefficient (ν). By applying Eq. (8) to the dynamic free surface boundary condition in the chamber ($\delta\eta/\delta t = \partial\phi/\partial z$), the energy reduction of the incident wave owing to fluid viscosity can be expressed as a viscous damping pressure term (Yang et al., 2019).

$$P_\nu(t) = K_L^*\bar{\dot{\eta}}(t) = \nu\frac{\partial\phi(t)}{\partial n} \tag{8}$$

where K_L^* and $\bar{\dot{\eta}}$ represent the modified loss coefficient and average velocity of the surface elevation inside the OWC chamber, respectively. Inside the OWC chamber where the duct is installed, the pneumatic pressure is generated by the free surface elevation, and this is represented by assuming a linear relationship between the pneumatic pressure (P_{ac}) in the OWC chamber and the velocity of the air flowing through the duct (Ning et al., 2015; Yang and Koo, 2020).

$$P_{ac}(t) = C_{dm}U_d(t) \tag{9}$$

where C_{dm} denotes a linear pneumatic damping coefficient and $U_d(t) = U_0\sin\omega t$ represents a relationship between air flow rate with time. The air flow rate through the duct is determined by the ratios of the chamber and duct sizes. Therefore, the pneumatic pressure inside the chamber is defined as:

$$P_{ac}(t) = \frac{C_{dm}\Delta V}{A_d\Delta t} \tag{10}$$

where A_d represents the area of the duct, $\Delta V/\Delta t$ is the rate of volume change inside the chamber, and the free surface boundary condition inside the OWC chamber, considering both the viscous damping effect and the pneumatic pressure effect (extractable by energy) owing to the duct, can be expressed by Eq. (11).

$$\frac{\delta\phi}{\delta t} = -g\eta + \frac{1}{2}|\nabla\phi|^2 - \frac{1}{\rho}\left(C_{dm}U_d + \nu\frac{\partial\phi}{\partial n} \right) \tag{11}$$

The energy efficiency of the sloped OWC system was calculated using the boundary conditions described above; accordingly, the

validity of the WEC numerical modeling and calculation results was verified. The incident wave energy flux can be expressed as the product of the incident wave energy and propagation velocity (group velocity). The fixed OWC WEC can be divided into four energy flux components: incident wave energy, reflected wave energy, maximum extractable energy of the turbine due to pneumatic pressure, and energy loss due to viscosity. Each of the four energy flux components can be expressed as follows (Koo et al., 2010; Kim et al., 2021).

$$E_i C_g = \frac{1}{8}\rho g H_i^2 C_g \tag{12}$$

$$E_R C_g = \frac{1}{8}\rho g H_R^2 C_g \tag{13}$$

$$AP = \frac{1}{2} C_{dm} A_d U_0^2 \tag{14}$$

$$EL = \frac{1}{2}\nu B \bar{\dot{\eta}}^2 \tag{15}$$

where H_i and H_R denote the incident and reflected wave heights, respectively, and C_g represents the group velocity. The average energy extraction rate (AP) is a value calculated per OWC chamber area and incident wave period, and it can be observed that the rate is proportional to the square of the air flow velocity in the nozzle (duct). The energy loss (EL) owing to viscosity was also calculated similarly, and it was confirmed to be proportional to the square of the average vertical velocity ($\bar{\dot{\eta}}$) of the free surface in the chamber. Therefore, the sum of the reflected wave energy flux ($E_R C_g$), average energy extraction (AP), and energy loss (EL) must be equal to the incident wave energy flux ($E_i C_g$) ($E_R C_g + AP + EL = E_i C_g$). Using this equation, the validity of this numerical modeling was verified via the numerical analysis results, which indicate that the energy of the entire WEC system is conserved within the computation domain

3. Numerical Modeling and Results

The computational domain for the numerical modeling of the sloped chamber OWC WEC is illustrated in Fig. 1. Here, d and B denote the draft and thickness of the OWC chamber skirt, respectively, L represents the width (gap) of the chamber, and h represents the water depth. In addition, B and h are 0.09 m and 0.5 m, respectively, and these values were fixed in this study, and the slope angle of the skirt was set at 33.7°, which is similar to the angle of domestic sloped breakwaters, and would enable the installation of this model on a sloped breakwater in the future.

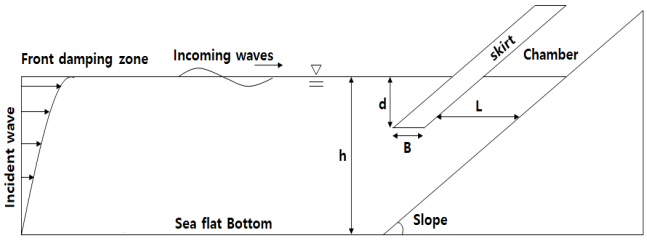

Fig. 1 Schematic diagram of a sloped OWC system with the open chamber condition

3.1 Open Chamber

To investigate the changes in the flow inside the chamber according to the OWC chamber conditions, a numerical model was applied under the condition that the pneumatic pressure inside the chamber is equal to atmospheric pressure, assuming the OWC chamber was open. For comparison with the experimental results of a previous study (Park et al., 2018b), the calculation was performed by applying the same incident wave conditions using a 1:20 scaled model. By setting the pneumatic pressure inside the chamber equal to atmospheric pressure, this model does not consider the power take-off (PTO). Tables 1 and 2 present the specifications various chamber dimensions and incident wave conditions used in the numerical analysis, respectively.

In the numerical analysis of this study, the viscosity of the fluid was not considered because the calculation was based on the assumption that the fluid was an inviscid, incompressible, and irrotational fluid. However, in real-sea conditions, energy attenuations occur, owing to the fluid viscosity between the structure and incident wave, as well as the energy loss according to the shape of the chamber structure. Therefore, to reflect the energy loss onto the numerical wave tank of the potential flow, the viscous damping coefficient should be substituted to consider the energy loss of the OWC system. For all cases in Table 1, arbitrary viscous damping coefficients were substituted to the numerical model, and the results closest to the experimental data (Park

Table 1 Specification of a numerical model of oscillating water column system (B = 0.09 m, h = 0.5 m)

Case	d (m)	L (m)
1	0.10	0.25
2	0.10	0.20
3	0.10	0.15
4	0.15	0.20
5	0.20	0.20

Table 2 Incident wave conditions

T (s)[1)]	H (m)[1)]	H/λ[1)]
1.00	0.066	0.044
1.15	0.065	0.034
1.30	0.057	0.025
1.45	0.056	0.021
1.60	0.055	0.018
1.75	0.051	0.015
1.90	0.045	0.012
2.05	0.041	0.01

[1)] T = incident wave period, H = incident wave height, λ = wavelength

et al., 2018b) with the same conditions were found, then, the adequate viscous damping coefficient was finally determined.

In Fig. 2, the results of the fully nonlinear time-domain calculations for surface elevation in the open chamber of Case 1 were compared under the conditions of incident wave period, wave height, and viscous coefficients at 1.75 s, 0.051 m, and ν = 0, 0.5, respectively. This corresponds to λ/L = 13.8 in Fig. 3. The surface elevation is the value of the difference between the wave crest and wave trough divided by 1/2. In this study, a ramp function twice the incident wave period (T) was applied to generate stable incident waves in the fully nonlinear numerical wave tank. In addition, because OWC WEC is located at a distance approximately 4 times the incident wavelength from the wave maker of the numerical wave tank, it can be inferred that the surface elevation in the chamber occurs after approximately 4 periods (t = 4 T). Under the above calculation conditions, in the calculation of the pure potential flow without viscous damping, it can be deduced that the elevation of the free surface inside the chamber is approximately 5 times higher than the incident wave, and when viscous damping effect is included, the elevation is approximately 3 times higher. Because the

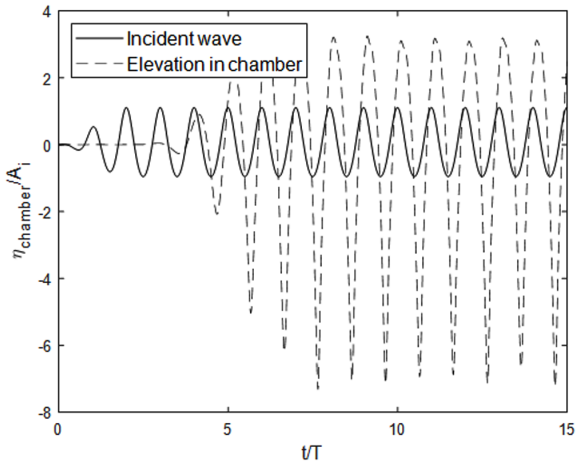

(a) T = 1.75 s, H = 0.051 m, ν = 0

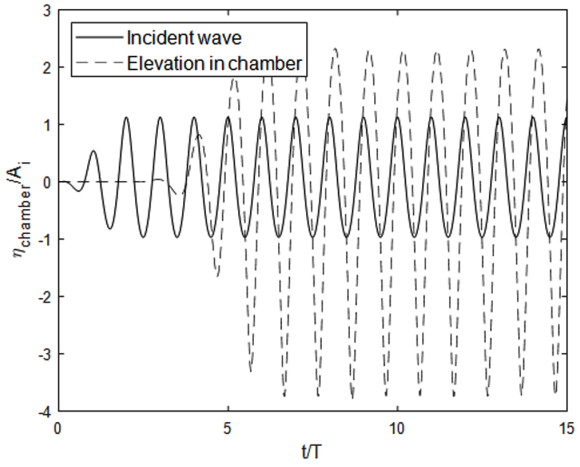

(b) T = 1.75 s, H = 0.051 m, ν = 0.5

Fig. 2 Time series of incident wave and chamber surface elevation in Case 1 (Open chamber)

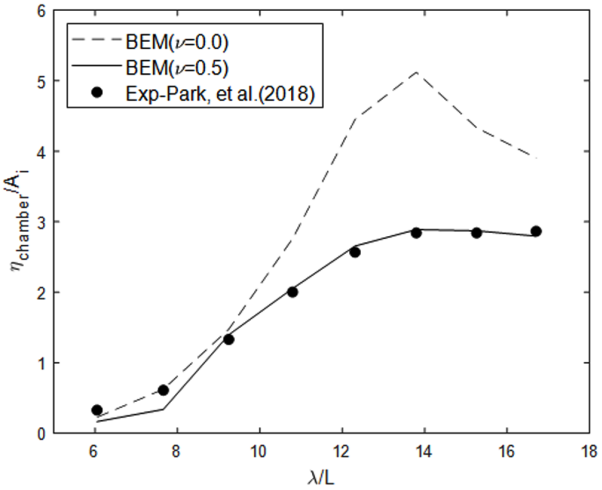

Fig. 3 Comparison of calculated surface elevations in the chamber with the experimental data at Case 1

surface elevation is high, as obtained from the results of the nonlinear calculation, the heights of the wave crest and wave trough are different, which triggers the asymmetry between the upper and lower surface elevations.

In Fig. 3, the calculated surface elevations in the chamber when viscous damping coefficient (ν = 0.5) was applied to the numerical model, and those obtained by pure potential flow analysis (ν = 0) are compared with the experimental data from Case 1. It can be observed that the results of the fully nonlinear numerical analysis with appropriate viscous damping coefficients agree well with the results of the 2D water tank experiment. In addition, when viscous damping was applied, the wave elevation in the chamber was reduced by approximately 28%. In particular, it was verified that when the incident wavelength is longer than the chamber width (approximately 12−15 times), the energy attenuation due to viscosity increases. In the conditions of this study, it can be observed that the viscous damping effect was the largest when the incident wavelength was approximately 14 times the chamber width.

In Fig. 4, similar to the case in Fig. 3, the viscous damping coefficients, which can derive the numerical results closest to the experimental results, were obtained under the conditions of Cases 2−5, by comparing the results obtained from the numerical analysis and the 2D wave tank experiment (Park et al., 2018b). When ν = 0.7 in Case 2, ν = 0.8 in Case 3, ν = 0.75 in Case 4, and ν = 0.8 in Case 5 were applied to the numerical model, the results were closest to the experimental results. Therefore, the reliability of the OWC chamber numerical modeling (open chamber condition) was verified by calculating the appropriate viscous damping coefficient according to the chamber skirt draft and chamber width compared to the experimental values.

3.2 Partial Open Chamber with Duct

The total computation domain of the sloped fixed OWC WEC with a duct is illustrated in Fig. 5.

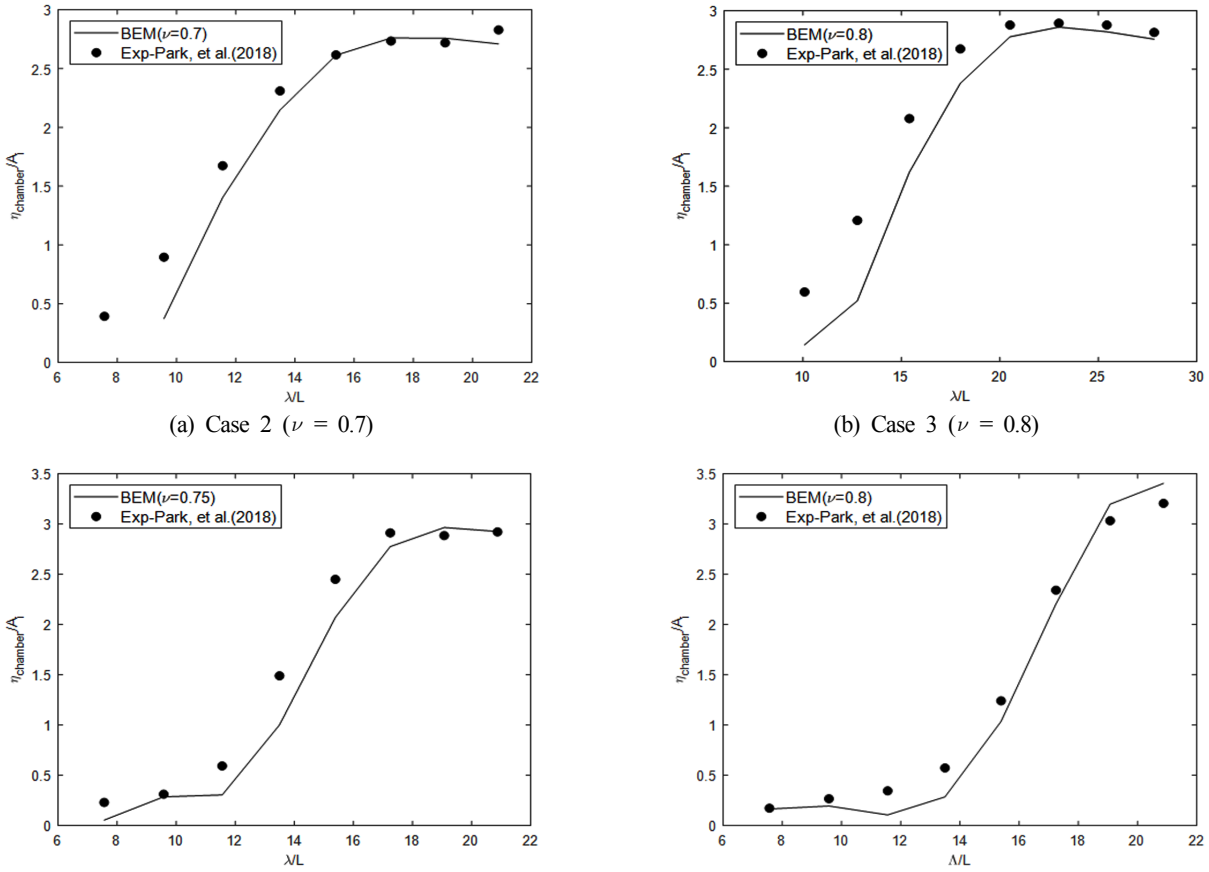

(a) Case 2 (ν = 0.7) (b) Case 3 (ν = 0.8)

(c) Case 4 (ν = 0.75) (d) Case 5 (ν = 0.8)

Fig. 4 Comparison of surface elevations in the chamber according to damping coefficients in various cases

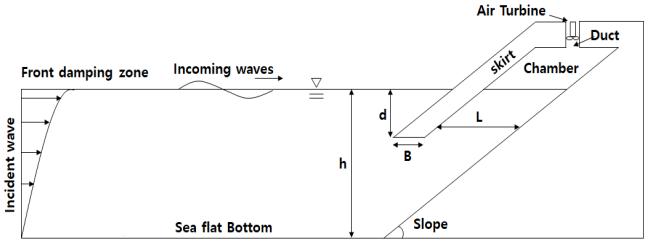

Fig. 5 Schematic of a sloped oscillating water column system with duct

Because the duct is installed in the upper part of the OWC chamber, pneumatic pressure occurs in the chamber. The pneumatic pressure inside the chamber is expressed by Eq. (10), which is substituted into the free surface boundary condition. The pneumatic damping coefficient (C_{dm}) represents the maximum extractable wave energy that can be extracted from the air turbine installed in the duct, and it is related to the ratio of the chamber and duct sizes. The pneumatic damping coefficient value (C_{dm} = 50) was obtained by comparing the numerical results with the experimental results reported in Park et al. (2018a). The ratio of the chamber cross-sectional area to the duct area was approximately 120. For the viscous damping coefficient, values obtained from a structure of the same size under the open chamber conditions were adopted.

Regarding Case 1 (d = 0.1 m, L = 0.25 m) conditions, with the incident wave period of 1.75 s and wave height of 0.051 m, the incident wave and free surface elevation in the chamber were compared in time series (Fig. 6). Unlike the open chamber condition, the free surface elevation in the chamber was reduced to approximately 1/2, compared to the incident wave height, and to approximately 1/4 compared to the open chamber results, as the wave energy was extracted owing to the presence of the duct. To verify the pneumatic pressure effect, the results were compared with the results of the water tank experiment conducted by Park et al. (2018a), under the same conditions (Fig. 7). In

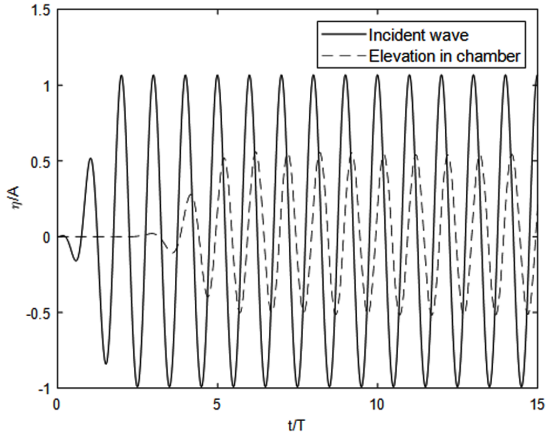

Fig. 6 Time series of incident wave and chamber elevation in Case 1 (T = 1.75 s, H = 0.051 m, ν = 0.5, Partial open chamber)

the open chamber (C_{dm} = 0) case, i.e., when the pneumatic pressure was zero, as the incident wavelength increased, the water surface in the chamber was elevated up to approximately 2.5 times the incident wave height; however, when a duct was installed in the chamber, the surface elevation decreased. This is because the pressure in the air chamber increased, owing to the installed duct; hence, free surface elevation in the chamber was suppressed. In fact, this can be regarded as the same effect when the wave energy was extracted with the air turbine of OWC, which led to the decrease in the energy in the chamber, and reduced the surface elevation. The above calculation is a case in which the air in the chamber is smoothly discharged from the duct without excessive compression, assuming that an air turbine with a large diameter, such as a Wells or an impulse turbine, is mainly used in the OWC. Therefore, in the case in which the viscous damping term has already been considered, the difference between the surface elevation in the open chamber and that in the chamber with the duct installed can be ascertained as the maximum extractable wave energy by the air turbine.

Fig. 8 presents the value of each energy flux component according to incident wave period and wave height conditions in Table 2 under Case 1 (d = 0.1 m, L = 0.25 m). It can be observed that the sum of the reflected wave energy flux, viscous damping energy, and air energy in the chamber is almost identical to the incident wave energy flux. This indicates that all energy flux components are accurately measured in the OWC WEC system. It can be observed that the energy (E-air) due to the air flow in the chamber increases as the incident wave period increases, which is approximately 20–40% of the incident wave energy. In addition, it can be observed that the reflected wave energy decreases with the increase in the period, which is at least 50% or more of the incident wave energy. In the future, it is necessary to develop a method that minimizes the reflected wave energy, such that more wave energy can be extracted. No significant change exists in the viscous damping energy relative to the change in the incident wave period.

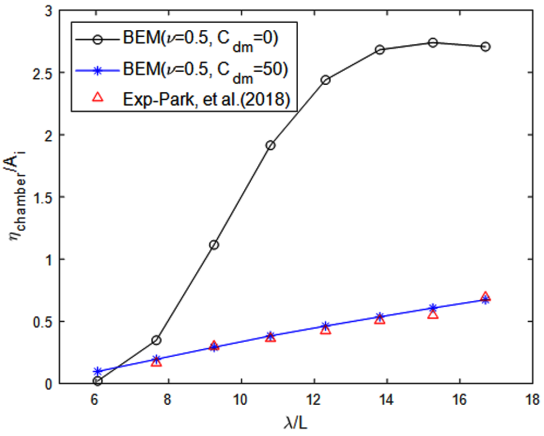

Fig. 7 Comparison of surface elevations in the chamber with a pneumatic damping coefficient

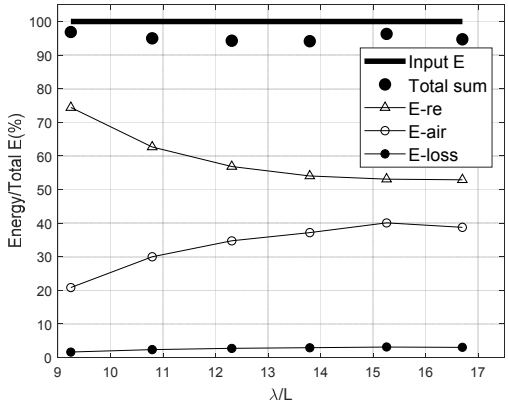

Fig. 8 Energy conservation of each energy flux component in Case 1 (d = 0.1 m, L = 0.25 m)

3.3 Real Scale Model

In this study, numerical analysis was performed on a 1:20 scaled model compared to the real size model for comparative validation with existing experimental results (Park et al., 2018a, 2018b), and via this comparison, it was determined that the validity of the numerical model was verified. Based on this finding, an appropriate viscous damping coefficient was calculated while increasing the size of the numerical model to predict the energy extraction (power) of the sloped OWC WEC on a real scale.

Fig. 9 illustrates the comparison with experimental values by substituting appropriate viscous damping coefficients for the real scale model (L = 5 m, d = 2 m), which is enlarged by 20 times compared to the scale model (L = 0.25 m, d = 0.1 m) under Case 1(L/d = 2.5). Accordingly, the changes in the viscous damping coefficient (ν/ν_0, ν_0 is the viscous coefficient of the scale model (d = 0.1 m) can be illustrated in Fig. 10 for various scale factors (2, 5, 10, 15, 20 times the initial scale model) of Cases 2, 4, and 5, with the same chamber width, and Cases 1–3 with the same draft of the chamber skirt. The obtained results confirmed that the viscous damping coefficient increased with a similar trend, according to the scale in all Cases.

To investigate the energy efficiency in actual sea environments, a calculation was performed under the wave conditions shown in Table 3, considering the average wave period of the Korean coast. The

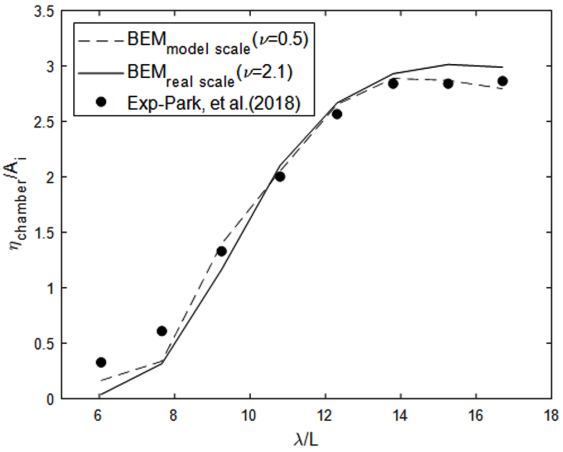

Fig. 9 Comparison of surface elevation in the chamber at model and real scales (Model: d = 0.1 m, L = 0.25 m, ν = 0.5, Real: d = 2 m, L = 5 m, ν = 2.1)

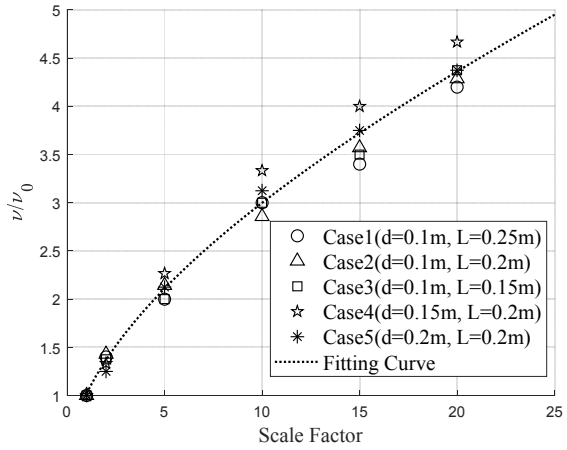

Fig. 10 Viscous damping coefficients with scale factor

viscous damping coefficient of the real scale model (20-times larger model, scale factor = 20) was obtained for each case. The maximum extractable energy was obtained by applying the calculated damping coefficient to the numerical analysis, and the obtained results are presented in Fig. 11. Because the pneumatic damping coefficient (C_{dm}) is related to the volume ratio, C_{dm} = 50 used in the scale model was adopted without alterations. When comparing the maximum extractable energy under the given incident wave conditions, the obtained value was the largest in Case 1. Table 3 presents the maximum extractable energy under the incident wave conditions, as

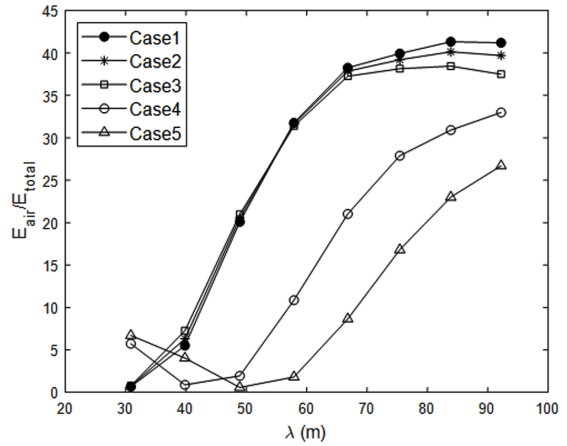

Fig. 11 Comparison of E-air for Cases 1–5

Table 3 Real scale condition and E-air at Case 1 (L = 5 m, d = 2 m)

T_real (s)	H_real (m)	λ (m)	E-air (kW/m)
4.47	1.32	30.85	0.05
5.14	1.3	39.81	0.55
5.81	1.14	48.90	1.94
6.48	1.12	57.87	3.48
7.16	1.1	66.80	4.57
7.83	1.02	75.41	4.59
8.50	0.9	83.87	4.01
9.17	0.82	92.20	3.53

well as the shape of Case 1 for the conditions. Under the conditions of period (T = 7.83 s), wavelength (λ = 75.41 m), and wave height (H = 1.02 m), the value of the maximum extractable energy was up to 4.59 kW/m, which is approximately 40% of the incident wave energy.

4. Conclusion

In this study, a sloped fixed OWC WEC was modeled using a 2D fully nonlinear numerical wave tank method based on potential flow. The viscous damping coefficients were calculated according to the chamber dimension, by comparing the numerical results obtained under the condition of an open OWC chamber with experimental results. Based on the obtained results, the wave elevation in the chamber was calculated relative to the chamber width and skirt draft. To consider the numerical model in which the pneumatic pressure is generated by the free surface elevations owing to the application of the duct in the OWC chamber, the pneumatic damping coefficient representing the maximum extractable energy from the air turbine installed in the duct. The viscous damping coefficient obtained from the open chamber condition were substituted to calculate the wave elevation in the chamber, which was compared to that of the experimental results under the same conditions, to verify the validity of the calculation results. In addition, energy conservation was verified in the system by calculating all energy flux components of the WEC system. The obtained results indicated that approximately 40% of the incident wave energy can be extracted under the conditions of Case 1. This value includes the energy loss due to turbine efficiency and viscous damping. Although the reflected wave energy gradually decreased in the long wave condition, the results indicated that the value was at least 50% or more of the incident wave energy. Therefore, a method for minimizing the reflected wave energy is required to extract the energy in further studies. In addition, a regular wave was adopted as an incident wave to accurately determine the energy extraction relationship, according to the shape of the OWC structure. The change in the viscous damping coefficient of the structure was predicted according to the scale factor, by expanding the numerical analysis scale model by approximately 20 times. By implementing the changes to the numerical analysis, the maximum extractable wave energy (approximately 4.59 kW/m) in the real scale structure (approximately 20 times that of the Case 1 model) was calculated, which was approximately 40% of the incident wave energy. In the future, for the accurate estimation of energy extraction in actual marine environmental conditions, follow-up studies with the applications of irregular wave conditions are required, and further studies on mutual verification should be conducted via a CFD simulation analysis based on viscous fluid.

Funding

This research was supported by the Basic Research Project of Science and Engineering, National Research Foundation of Korea (NRF-2018R1D1A1B07040677).

References

Bae, S. (2021). 2050 Carbon Neutral. Electric Power, 1, 70–71.

European Marine Energy Centre Ltd. (EMEC). (2018). Marine Energy/Wave Devices. Retrieved 20 April 2021 from http://www. emec.org.uk/marine-energy/wave-devices/

Gaspar, L.A., Teixeira, P.R.F., & Didier, E. (2020). Numerical Analysis of the Performance of Two Onshore Oscillating Water Column Wave Energy Converters at Different Chamber Wall Slopes. Ocean Engineering, 201, 107119. https://doi.org/10.1016/j.oceaneng.2020.107119

Heo, S. (2016). Climate Change and Concerted Actions by Mankind. Journal of Korean Social Trend and Perspective, 96, 214–220.

Kim, D.M., Min, E.H., & Koo, W. (2021). Numerical Study on the Optimal Shape and Performance of an Oscillating Water Column Using Analytic Air Damping Coefficients and Numerical Wave Tank. Journal of The Korean Society for Marine Environment & Energy, 24(1), 1–8. https://doi.org/10.7846/JKOSMEE.2021.24.1.1

Kim, J.H., Lew, J.M., Hong, D.C., & Hong, S.W. (2006). A Study on Motion and Wave Drift Force of a BBDB Type OWC Wave Energy Device. Journal of Ocean Engineering and Technology, 20(2), 22–28.

Kim, S.J., Koo, W., & Kim, M.H. (2015). Nonlinear Time-domain NWT Simulations for Two Types of a Backward Bent Duct Buoy (BBDB) Compared with 2D Wave-tank Experiments. Ocean Engineering, 108(1), 584–593. https://doi.org/10.1016/j.oceaneng.2015.08.038

Kim, S.J., Kwon, J., Kim, J.D., Koo, W., Shin, S., & Kim, K. (2012). Experimental Study of Hydrodynamic Perfromance of Backward Bent Duct Buoy (BBDB) Floating Wave Energy Converter. Journal of Ocean Engineering and Technology, 26(6), 53–58. https://doi.org/10.5574/KSOE.2012.26.6.053

Koo, W.C., Kim, M.H., & Choi, Y.R. (2010). Numerical Analysis of Chamber Flow and Wave Energy Conversion Efficiency of a Bottom-Mounted Oscillating Water Column Wave Power Device. Journal of the Society of Naval Architects of Korea, 47(3), 388–397. https://doi.org/10.3744/SNAK.2010.47.3.388

Koo, W., Kwon, J.S., Kim, J.D., Kim, S.J., Kim, M.W., & Choi, M.K. (2012). Experimental Study of Shape Parameter of Land-based OWC Wave Energy Converter. Journal of Ocean Engineering amd Technology, 26(3), 33–38. https://doi.org/10.5574/KSOE.2012.26.3.033

Lee, K.R., Koo, W., & Kim, M.H. (2013). Fully Nonlinear Time-domain Simulation of a Backward Bent Duct Buoy Floating Wave Energy Converter Using an Acceleration Potential Method. International Journal of Naval Architecture and Ocean Engineering, 5(4), 513–528. https://doi.org/10.2478/IJNAOE-2013-0150

Liu, C., Huang, Z.H., Keung, A.L.W., & Geng, N. (2010). A Numerical Study of Wave Energy Converter in the Form of an Oscillating Water Column Based on a Mixed Eulerian-Lagrangian Formulation. Proceedings of the ASME 2010 29th International Conference on Ocean, Offshore and Arctic Engineering, Shanghai, China, 589–596. https://doi.org/10.1115/OMAE2010-21056

Ning, D.Z., Guo, B.M., Wang, R.Q., Vyzikas, T., & Greaves, D. (2020). Geometrical Investigation of a U-shaped Oscillating Water Column Wave Energy Device. Applied Ocean Research, 97, 102105. https://doi.org/10.1016/j.apor.2020.102105

Ning, D.Z., Shi, J., Zou, Q.P., & Teng, B. (2015). Investigation of Hydrodynamic Performance of an OWC (Oscillating Water Column) Wave Energy Device Using a Fully Nonlinear HOBEM (Higher-Order Boundary Element Method). Energy, 83, 177–188. https://doi.org/10.1016/j.energy.2015.02.012

Ning, D.Z., Wang, R.Q., Zou, Q.P., & Teng, B. (2016). An Experimental Investigation of Hydrodynamics of a Fixed OWC Wave Energy Converter. Applied Energy, 168, 636–648. https://doi.org/10.1016/j.apenergy.2016.01.107

Park, S., Kim, K.H., Nam, B.W., Kim, J.S., & Hong, K. (2018a). A Study on the Performance Evaluation of the OWC WEC Applicable to Breakwaters using CFD. Journal of The Korean Society for Marine Environment & Energy, 21(4), 317–327. https://doi.org/10.7846/JKOSMEE.2018.21.4.317

Park, S., Nam, B.W., Kim, K.H., & Hong, K. (2018b). Parametric Study on Oscillating Water Column Wave Energy Converter Applicable to Breakwater. Journal of Advanced Research in Ocean Engineering, 4(2), 66–77. https://doi.org/10.5574/JAROE.2018.4.2.066

Sarmento, A.J.N.A., & Falcao, A.F. (1985). Wave Generation by an Oscillating Surface-pressure and Its Application in Wave-energy Extraction. Journal of Fluid Mechanics, 150, 467–485. https://doi.org/10.1017/S0022112085000234

Yang, H.J., Koo, W., & Kim, S.J. (2019). A Study on th Shape Parameters of a Sloped Oscillating Water Column WEC Using a 2D Full Nonlinear Numerical Wave Tank. Proceedings of 2019 Fall Conference of the Society of Naval Architects of Korea, Gyeongju, Korea, 390-393.

Yang, H.J., & Koo, W.C. (2020). A Study on the Performance Evaluation of the Sloped Oscillating Water Column WEC Using a 2D Full Nonlinear Numerical Wave Tank. Proceedings of 2020 Fall Conference of the Korean Society of Ocean Engineers, Korea, 224–227.

Author ORCIDs

Author name	ORCID
Yang, Hyunjai	0000-0001-6258-2315
Min, Eun-Hong	0000-0003-1045-9475
Koo, WeonCheol	0000-0002-4384-0996

KSOE

Journal of Ocean Engineering and Technology 35(4), 305-312, August, 2021
https://doi.org/10.26748/KSOE.2021.043

pISSN 1225-0767
eISSN 2287-6715

Original Research Article

Mechanism Development and Position Control of Smart Buoy Robot

Hwi-Geun Park[1] and Hyun-Sik Kim[2]

[1]*Graduate Student, Department of Mechanical System Engineering, Tongmyong University, Busan, Korea*
[2]*Professor, School of Mechanical Engineering, Tongmyong University, Busan, Korea*

KEY WORDS: Smart buoy robot, Positioning control, Docking and charging, Lighting, Automatic anchoring

ABSTRACT: *There is a gradual increase in the need for energy charging in marine environments because of energy limitations experienced by electric ships and marine robots. Buoys are considered potential energy charging systems, but there are several challenges, which include the need to maintain a fixed position and avoid hazards, dock with ships and robots in order to charge them, be robust to actions by birds, ships, and robots. To solve these problems, this study proposes a smart buoy robot that has multiple thrusters, multiple docking and charging parts, a bird spike, a radar reflector, a light, a camera, and an anchor, and its mechanism is developed. To verify the performance of the smart buoy robot, the position control under disturbance due to wave currents and functional tests such as docking, charging, lighting, and anchoring are performed. Experimental results show that the smart buoy robot can operate under disturbances and is functionally effective. Therefore, the smart buoy robot is suitable as an energy charging system and has potential in realistic applications.*

1. Introduction

In recent years, there have been increasing studies on technologies employed in the Fourth Industrial Revolution, including technologies related to the maritime industry. As a result, there have been extensive development and application of autonomous surface vessels, unmanned surface vessels, and surface/underwater robots (Kwon et al., 2017; Kang et al., 2014; Jeong et al., 2018; Yeu et al., 2019).

In addition, the International Maritime Organization (IMO) has enacted safety regulations on factors that contribute to the destruction of marine environments by vessels, so there is an increased need for the development of electric vessels (Clayton et al., 2000).

However, electric vessels and unmanned surface/underwater robots have finite power supply owing to their limited size. Because of this problem, small electric boats and electric ships may drift on the water when the battery is fully discharged. Currently, in South Korea, the Korea Coast Guard is dispatched to charge the battery of drifting electric boats or ships, or another vessel may tow drifting electric boats or ships to port. However, it takes a long time for the Korea Coast Guard to arrive at the location of the drifting boat or ship. Further, there may be collisions when drifting electric boats or ships encounter other vessels.

In order to solve these problems, there have been studies on the development of marine robots that can harvest marine energy, such as sail drones, wave gliders, and underwater gliders (Man et al., 2020). However, energy harvesting technologies cannot be applied uniformly because the shapes and characteristics of robots are diverse. In addition, energy harvesting technologies generally supply power in proportion to the size of the robot. Because marine robots that harvest energy are limited in their size, this method cannot be considered a realistic solution from an efficiency perspective.

To solve this problem, there is the need for a system that is fixed to a specified position and that can charge batteries. A buoy was considered because it is fixed to a specified position in the ocean. A buoy is tethered to an anchor, so it can maintain its position. Buoys are used for various roles, such as showing a route or informing oncoming traffic about hazardous areas (Kim, 2015). However, anchors that secure buoys to fixed positions may be disconnected owing to inclement weather conditions in the ocean. In such a case, the buoy cannot maintain its specified position and may drift towards shore. Moreover, the different shapes of buoys make it difficult for docking by vessels, which may damage the buoy during docking.

In order to solve these problems, research on marine charging light buoy robots was also conducted in South Korea. However, modularization for maintenance and optimization were not achieved during the design and manufacturing processes. In addition, there was

Received 8 June 2021, revised 2 July 2021, accepted 9 July 2021
Corresponding author Hyun-Sik Kim: +82-51-629-1565, hyunskim@tu.ac.kr

also a problem with respect to waterproofing (Park et al., 2019).

Therefore, in this study, the problem regarding waterproofing was factored in during the design and manufacturing processes, and the modularization of the robot was considered for maintenance. In addition, we proposed the development of a smart buoy robot mechanism that enables the buoy robot to maintain its specified position using underwater motors. Unlike the shapes of existing buoys, the proposed robot has four docking parts and is shaped like the letter X, making it easy for vessels to dock with it.

The International Association of Marine Aids to Navigation and Lighthouse Authorities (IALA) and the Ministry of Oceans and Fisheries (MOF) recommend specific colors and light colors for standard buoys (IALA, 2017). However, because the proposed buoy is a non-standard buoy, we considered an arbitrary color and light color. We differentiated the color by combining the purple color with the yellow color of special aid to navigation, and we used purple light.

Section 2 describes the development of the buoy robot mechanism, and Section 3 focuses on the design of the buoy robot controller. Section 4 explains the experiment and considerations made when verifying the performance of the buoy robot mechanism and proposed controller. Finally, Section 5 summarizes the paper.

2. Development of Buoy Robot Mechanism

The operation concept shown in Fig. 1 was first considered for the development of the buoy robot

The body of the robot is formed in the shape of a buoy, and a manipulator is mounted on the robot so it can deliver a cable when a vessel that needs to be charged is docked with the robot. When the robot is moving, the manipulator is folded against the column to minimize the effect of disturbance. The camera is mounted on the robot so that it can check for ships.

The buoy robot was designed based on the operation concept using a three-dimensional (3D) tool called Computer Aided Three dimensional

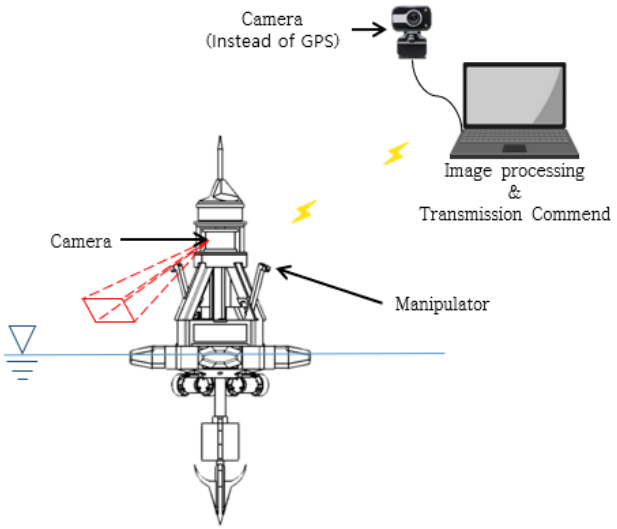

Fig. 1 Diagram of operation concept

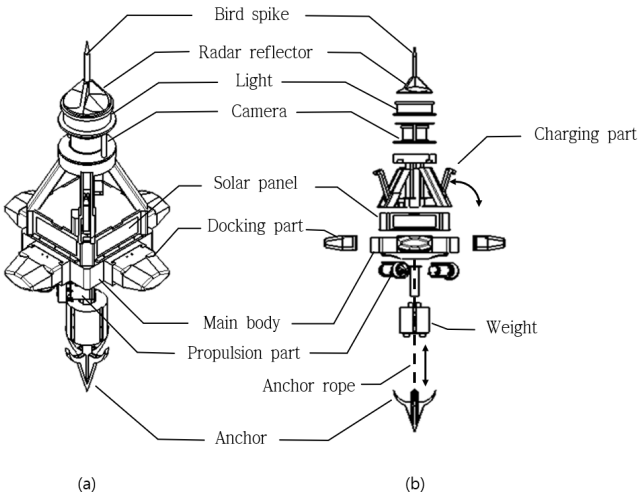

Fig. 2 Mechanism of buoy robot

Interactive Application (CATIA). Fig. 2(a) shows the final design, and Fig. 2(b) illustrates the design that considers modularization, as mentioned previously. Each module was made such that it is easy to disassemble and assemble them. The buoy is made in the shape of the letter X, formed by four docking parts. This shape was considered to allow the bow and stern of a ship to dock with the robot, making it easy to secure the ship to the buoy. In addition, to reduce the maintenance cost, the buoy was designed such that the docking parts can be separated from it and replaced if they are damaged.

Moreover, because bird excrement is acidic, the bird spike performs the function of preventing corrosion, reducing the need for the maintenance of the buoy robot.

The radar reflector is a radio aid to navigation that amplifies and reflects the radar signals. The lighting is a visual aid to navigation that uses light to convey to ships the position guidance and the purpose of the buoy. This system uses purple light.

The camera was installed to visually check the ship that is docked or docking with the buoy robot. The charging part uses the robot arm to deliver the charging cable to the ship that is docking with the buoy robot.

Next, the placement of the solar panel was considered for energy harvesting. The sensor, motor drive, and battery are placed in the main body. The weight was considered to enhance the attitude stability by lowering the buoy robot's center of gravity. The anchor is connected to

Table 1 Functions of buoy robot

Buoy robot	Rapidity	Propulsion part
	Charging	Docking part
		Robot hand
	Stability	Bird spike
		Radar reflector
		Light
		Camera
		Anchor

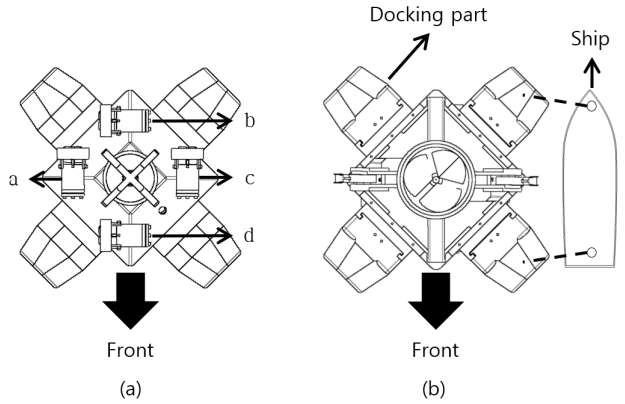

Fig. 3 Propulsion and docking part

the DC motor placed inside the main body via the anchor rope, and the anchor is designed such that automatic anchoring and retraction are possible. Hence, the buoy robot can be anchored at a specified position, and the anchor is retracted when the buoy robot needs to move. Each function mentioned above is categorized and summarized in Table 1.

Fig. 3(a) shows the composition of the propulsion motor, which is used to control the position and movement of the buoy robot. A total of four motors were used: a, b, c, and d. Motors a and c form a set, and motors b and d form another set to control the buoy robot. Because the energy consumption is high when all four motors are used, sets of motors with parallel forces are used. Hence, the position of the buoy robot can be maintained even if one or two motors break down.

The dotted lines in Fig. 3(b) indicate the ropes between the docking parts and the ship. Here, the bow and stern of the ship are secured to two docking parts. As mentioned earlier, there are four docking parts, so it is easy to secure a ship. At most, two ships can dock with the buoy robot simultaneously.

Fig. 4 shows the shape of the completed prototype. The prototype was made as a miniaturized model to make it convenient for

Fig. 4 Prototype of buoy robot

Table 2 Specification of prototype

Size	Turning radius	degree	0
	Weight (on air)	kg	3.5
	Payload	kg	1.25
	Length over all (*L*)	mm	410
	Moulded brdadth (*B*)	mm	410
	Depth (*D*)	mm	365
	Height (*H*)	mm	490
Speed	Electric propulsion (Max. speed)	m/s	0.07
		knot	0.136

fabrication and experimentation, and the prototype was fabricated using a 3D printer based on 3D modeling. As mentioned previously, yellow and white colors were used for the body of the buoy robot, and purple color was used for the docking part, bird spike, and radar reflector. The part that covers the body of the buoy robot was fabricated using acrylic. Table 2 shows the specifications of the completed robot.

3. Design of Buoy Robot Controller

The buoy robot performs positioning control by receiving the error value of the image coordinates using the camera that is connected to the host PC. Fig. 5 shows the flowchart of the control algorithm. First, the heading is controlled using the attitude heading reference system (AHRS). The position is then controlled by using the error value of the current position from the target position on the image coordinates.

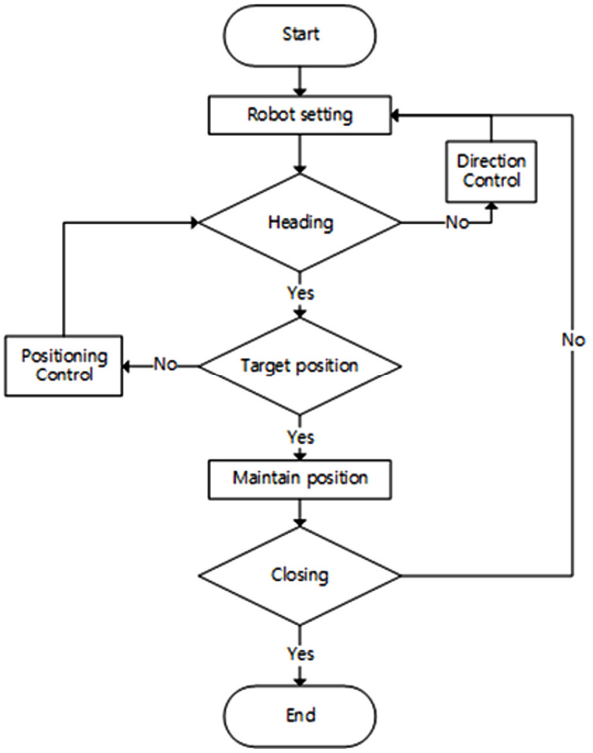

Fig. 5 Flow chart of control algorithm

3.1 Position Accuracy, PA

The PA related to the performance index of the position control is defined by Eq. 1 when the reference position x_r, y_r is determined. The PA denotes the maximum error position value of the buoy robot.

$$r_i = \sqrt{(x_i - x_r)^2 + (y_i - y_r)^2} \tag{1}$$
$$PA = \max(r_i)$$

Here, x_i, y_i is the position value of the buoy robot at the i-th sampling time, and max() is a function that calculates the maximum value.

3.2 Current Direction Prediction

In order to control the position of the buoy robot robustly in the presence of current disturbances, it is necessary to predict the direction of the current. In this study, we selected a method that utilizes the position information to predict the direction of the current. When a current occurs, the buoy is generally pushed in the direction the current flows, and its position information is changed. In order to predict the direction of the current using the change in the position information, Eq. 2 below is considered to first determine the effect of the current. The direction of the current is predicted by using the difference between the target position value and the position value at the moment this equation is satisfied.

$$r^2 < (x_i - x_r)^2 + (y_i - y_r)^2 \tag{2}$$

Here, r is the reference radius, and it is set empirically to determine whether the buoy robot was affected by the current (Park, 2021).

In Fig. 6, the solid lines intersecting at the center of the buoy robot are the x and y axes of the image reference coordinate system. The dotted arrows indicate the moving direction for each set of thrusters, as explained in Fig. 3.

Here, the thrusters can propel the buoy robot uniformly at 45° with reference to the image reference coordinate system. Therefore, the area

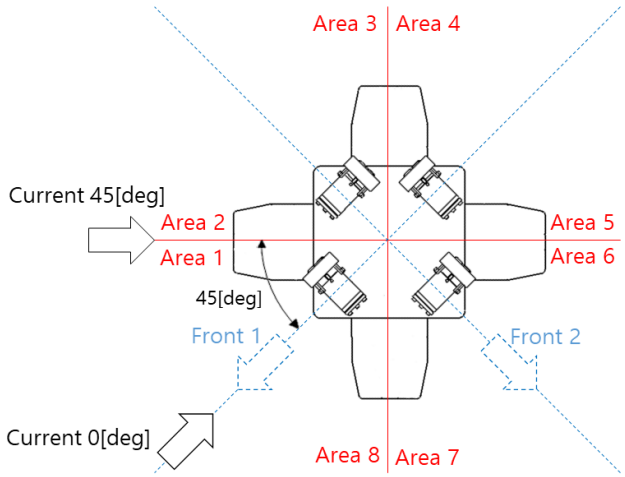

Fig. 6 Anaysis of current directions and areas

Fig. 7 Coordinate system of camera

of the image reference coordinate system can be subdivided using the dotted arrows. The dotted lines formed using the direction of motion are composed of straight-line regions. They can be divided into eight areas using the straight-line regions and the image reference coordinate system.

Because each of the eight regions has an area of 45°, the direction of the currents generated in all regions is equivalent to two cases--the direction is a minimum of 0° and a maximum of 45°. The solid arrow denotes the arrow for the direction of the current mentioned.

Fig. 7 shows the actual display of the camera that was installed for the experiment as a substitute for GPS. Of the three red, green, blue (RGB) colors, the red color is tracked for ease of implementation. With regard to acquiring the buoy robot's position information, the red color is tracked to simplify camera image processing. The radar reflector was set to red color, and the radius of the circle related to Eq. (2) was formed based on the radar reflector. Using this setup, it is possible to know the region in which the buoy robot is located.

Fig. 8 shows a control block diagram. The P-Controller, which is a proportional controller using an error, was considered. In addition, the distributor is used to distribute the control values to the motors M_1, M_2, M_3, M_4 which control P_x, P_y. Here, x_r, y_r is the target position and denotes (97, 42). e_x denotes the x-coordinate error, and e_y denotes the y-coordinate error. x_i, y_i indicates the current x, y coordinates values. The P-Controller derives and using the x and y error values, respectively, and control values are input into each motor (M_1, M_2, M_3, M_4) through the distributor.

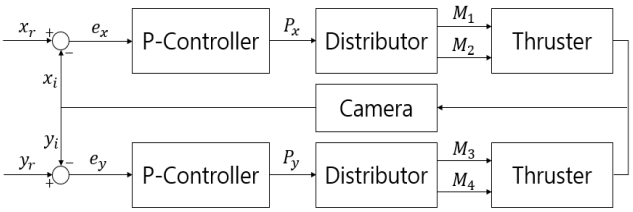

Fig. 8 Block diagram of position control system

4. Experimental Results

A test evaluation was performed to verify the performance of the developed robot. First, functional tests were performed to verify the mechanism of the buoy robot. The test evaluation was composed of four categories. Propulsion (T1) is a test evaluation category that is related to the propulsion of the robot, and mechanism (T2) is a category for the robot's lighting, charging, and anchoring functions.

Communication (T3) is a category that determines whether data transmission and control are possible by performing communication between the robot and the host PC to control the robot. Positioning control (T4) is a category that checks whether the control method proposed in Section 3 has been applied to the robot to enable the position control.

The results of the requirements analysis are mobility (R1), manipulability (R2), observability (R3), stability (R4), and maintainability (R5). The functional categories are the forward/reverse rotation function of the underwater motor (F1), lighting function (F2), docking and charging function (F3), automatic anchoring and retraction function (F4), camera function (F5), attitude restoration function (F6), modularization function (F7), and program download function (F8). H/W and S/W categories are components of the H/W and S/W family tree. Table 3 shows the test evaluation results that determine whether each category maintains traceability.

Fig. 9 shows that the (a) docking and charging function, (b) lighting function, and (c) automatic anchoring function are working properly.

The position control experiments were conducted for three cases (when current was not generated, when the current was generated from the oncoming direction, and when the current was generated from the 45° direction), and the results were compared.

Fig. 10 shows the experimental environment, and a water tank was used for the indoor experiment. In addition, a camera was used in place of the GPS, and images were processed to distinguish and track the red color using the RGB.

Table 3 Traceability

Requir-ement	Function	H/W component	S/W component	Test & Evaluation	Result
R1	F1	H2, H5, H6	S1, S4	T1, T4	○
	F2	H33, H51, H71	S21	T2	○
R2	F3	H131, H2, H31, H4, H5, H6	S1, S22, S3, S4	T1, T2, T3, T4	○
	F4	H32, H5	S23, S3	T2, T4	○
R3	F5	H2, H42, H5, H6, H71	S1, S24, S3, S4	T1, T2, T3, T4	○
R4	F6	H13	-		○
R5	F7	H1	-		○
	F8	H7	S4		○

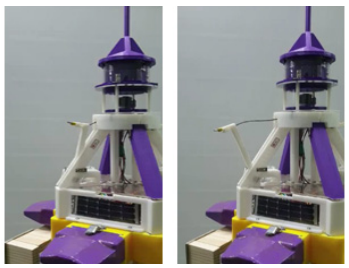

(a) Docking and charging function

(b) Light function

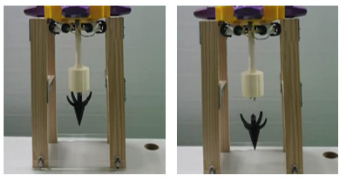

(c) Automatic anchoring funtion

Fig. 9 Functional tests of buoy robot

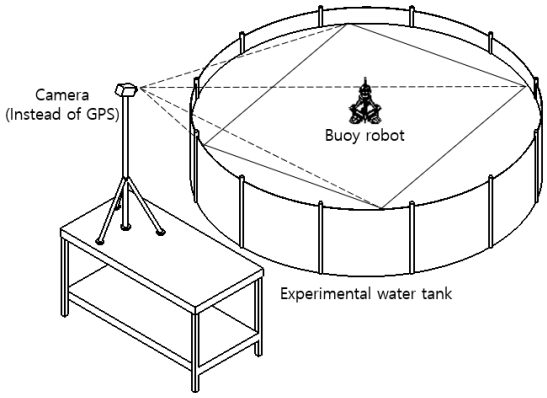

Fig. 10 Experimental enviroment

Figs. 11–13 illustrate the test evaluation scenarios. Here, the large arrow indicates the front, and the five small arrows represent the

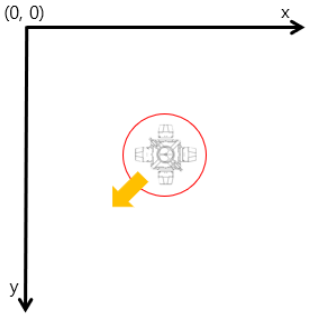

Fig. 11 Scenario for position control (no disturbance)

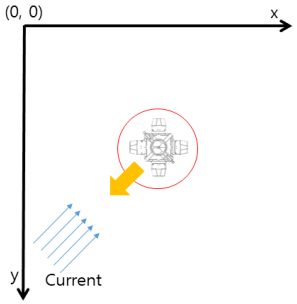

Fig. 12 Scenario for position control (0° disturbance)

current. Fig. 11 shows the scenario where position control is performed at the target position when there is no current disturbance.

Fig. 12 shows the scenario where position control is performed at the target position when there is a current disturbance in the 0° direction.

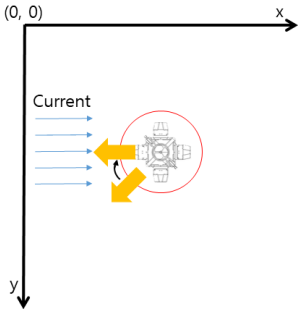

Fig. 13 Scenario for position control (45°)

Fig. 13 shows the scenario where position control is performed at the target position when there is a current disturbance in the 45° direction.

The experiments were conducted for each scenario mentioned above after empirically setting the radius of the discriminant-related circle to 10. The results of the experiments are as follows.

The maximum X, Y coordinates of the camera images are (320, 240), and the basic unit of the coordinates is measured to be about 1 cm. The experimental results are shown on the area where the X-axis ranges from 50 to 140 and the Y-axis ranges from 20 to 65. The target position is (97, 42). In the legend, the diamond mark denotes the target position, and small circles denote the sampling positions of the buoy robot. In addition, the dotted line represents the PA-related circle, and the solid line represents the discriminant-related circle.

In Fig. 14, the PA is 7.1 cm, and there is no current disturbance. Therefore, position control was performed inside the discriminant-related circle. Because small circles are densely populated, it can be seen that position control is well performed.

In Fig. 15, the current was generated from the 0° direction. Because a large number of small circles are distributed in the upper right region of the graph, it can be seen that the current was generated in the direction of (70, 60). Even though a few small circles were pushed outside the discriminant-related circle owing to the effect of the current, position control was performed without performing direction control because the current was generated from the oncoming direction. Because small circles are distributed in similar positions, it can be seen that position control is well performed. The PA is 10.8 cm,

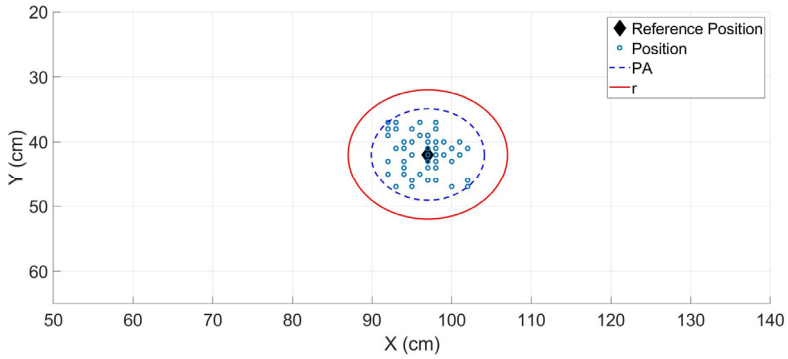

Fig. 14 Performance of position control (no disturbance)

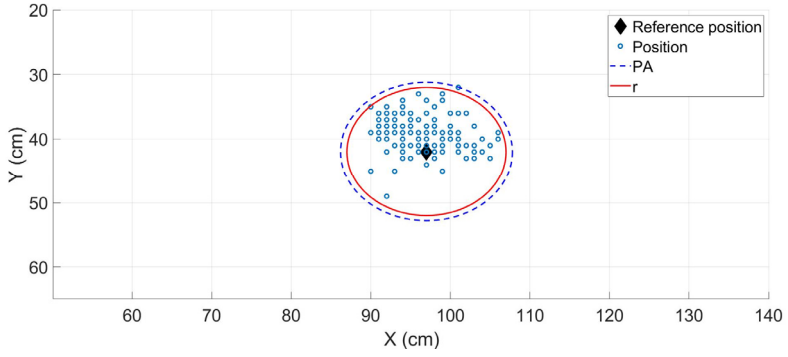

Fig. 15 Performance of position control (0° disturbance)

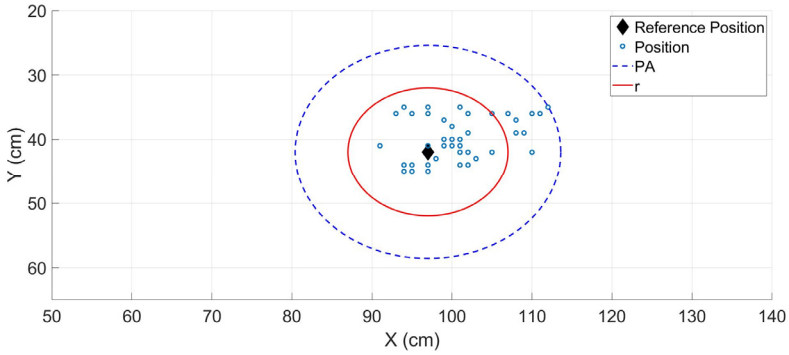

Fig. 16 Performance of position control (45° disturbance)

Table 4 Experimental results

Scenario	No disturbance	0-disturbance	45-degree disturbance
Heading initial value	0.0°	0.0°	0.0°
Heading change value	×	×	45.0°
Disturbance	×	◯	◯
PA	7.1 cm	10.8 cm	16.6 cm
r	10.0 cm	10.0 cm	10.0 cm

so the PA value is increased by 3.7 cm compared to the case when there was no current.

In Fig. 16, the current was generated from the 45° direction. Because many of the small circles are distributed on the right side of the graph, it can be seen that the current was generated in the direction of (70, 45). The small circles were pushed out of the discriminant-related circle owing to the effect of the current. Because the current was generated from the direction that is not directly in front of it, direction control was first performed, followed by position control. Because the position control was performed after the direction control, it can be seen that the position control has increased. In addition, the PA is 16.6 cm. Compared to the case when there was no current, it can be seen that the PA value is increased by about 9.5 cm.

The experimental results for the three types of scenarios are summarized in Table 4. Direction control was performed to change the direction from 0° to 45° only for the scenario where the current was generated from the 45° direction. In addition, it can be seen that the error radius for each scenario is increased owing to the current.

5. Conclusion

This study investigated the mechanism and position control of a new smart buoy robot that considers the shape, colors, and light such that they are different from those of existing buoys.

The developed smart buoy robot is shaped like the letter X, making it easy for docking, and this is different from existing buoys. A purple light was used, which is not in conflict with the IALA recommendations, and a yellow color was used to provide special aid for navigation purposes, and the buoy was made to have the color purple. Maintenance was considered through modularization, and various mechanisms, such as docking, charging, automatic anchoring, and retraction, can be verified from the perspective of functionality.

In addition, the proposed position controller used the P-Controller, and three experiment scenarios were modeled. Based on the experiment results, it was confirmed that the proposed position controller has outstanding performance. When the current was generated from the 45° direction, the buoy robot was pushed out of the reference radius. Therefore, direction control is performed, followed by position control, using the radius of the current direction discriminant-related circle. As a result, the buoy robot was pushed out by the current during the direction control process. However, after the direction control, it was seen that the buoy robot overcomes the current head-on.

This study has established a foundation for domestic research on smart buoy robots. However, there was no study on energy harvesting technologies and their efficiency, which have potential for application to smart buoy robots. In the future, we plan to continue our research on the efficiency of marine energy harvesting techniques that are suitable for smart buoy robots.

References

Kwon, Y.J., Kang, G.M., & Park, S.H. (2017). The Fourth Industrial Revolution and Marine Technology. Journal of Innovation Studies, 12(2), 203-222. http://dx.doi.org/10.46251/INNOS.2017.05.12.2. 203

Kang, H.J., Man, D.W., & Kim, H.S. (2014). Development of Mechanism for Micro Surface Robot with Rotating Sonar-Beam. Journal of Korean Institude of Intelligent Systems, 24(4), 437-442. http://dx.doi.org/10.5391/JKIIS.2014.24.4.437

Jeong, J.S., Sa, Y.M., & Kim, H.S. (2018). Development of Autonomous Surface Robot for Marine Fire Safety. Journal of Ocean Engineering and Technology, 32(2), 138-142. https://doi.org/10.26748/KSOE. 2018.4.32.2.138

Yeu, T., Choi, H.T., Lee, Y., Chae, J., Lee, Y., Kim, S.S., ... & Lee, T.H. (2019). Development of Robot Platform for Autonomous Underwater Intervention. The Korean Society of Ocean Engineers, 33(2), 168-177. https://doi.org/10.26748/

KSOE.2019.021

Clayton, D.H., Sudhoff, S.D. , & Grater, G.F. (2000). Electric Ship Drive and Power System. Proceedings of Conference Record of the 2000 Twenty-Fourth International Power Modulator Symposium, 85−88. https://doi:10.1109/MODSYM.2000.896171.

Man, D.W., Cho, G., & Kim, H.S. (2020). Comparative Study on Keel Effects of Catamaran-Type Sail Drone. ICIC Express Letters, Part B: Applications, 11(3), 261−266. https://doi.org/10.24507/icicelb.11.03.261

Kim, H.S. (2015). Development of Buoy-based Autonomous Surface Robot-kit. Journal of Ocean Engineering and Technology, 29(3). 249−254. http://dx.doi.org/10.5574/KSOE.2015.29.3.249

Park, H.G., Man, D.W., Jo, Y.J., & Kim, H.S. (2019). Lighting Buoy Type Marine Charging Robot Base on Marine Energy Harvesting. Proceedings of KIIEE (Busan・Ulsan・Kyungnam Branch) Annual Conference, 59−62.

International Association of Marine Aids to Navigation and Lighthouse Authorities (IALA). (2017). R1001-The IALA Maritime Buoyage System. Retrieved from https://www.iala-aism.org/product/r1001-iala-maritime-buoyage-system/

Park, H.G. (2021). Study on Development and Position Control of Smart Buoy Robot (Master's thesis). University of Tongmyong, Busan, Korea.

Author ORCIDs

Author name	ORCID
Park, Hwi-Geun	0000-0003-3139-2337
Kim, Hyun-Sik	0000-0003-4821-9784

Instructions for Authors

General information

To submit a manuscript to the Journal of Ocean Engineering and Technology (JOET), it is advised to first carefully read the aims and the scope section of this journal, as it provides information on the editorial policy and the category of papers it accepts. Unlike many regular journals, JOET usually has no lag in acceptance of a manuscript and its publication. Authors that find a match with the aims and the scope of JOET are encouraged to submit as we publish works from all over the world. JOET adheres completely to guidelines and best practices published by professional organizations, including Principles of Transparency and Best Practice in Scholarly Publishing (joint statement by COPE, DOAJ, WAME, and OASPA (http://doaj.org/bestpractice) if otherwise not described below. As such, JOET would like to keep the principles and policies of those professional organizations during editing and the publication process.

Research and publication ethics

Details on publication ethics are found in http://joet.org/authors/ethics.php. For the policies on research and publication ethics not stated in the Instructions, Guidelines on Good Publication (http://publicationethics.org/) can be applied.

Requirement for membership

One of the authors who submits a paper or papers should be member of the Korean Society of Ocean Engineers (KSOE), except a case that editorial board provides special admission of submission.

Publication type

Article types include scholarly monographs (original research articles), technical articles (technical reports and data), and review articles. The paper should have not been submitted to other academic journal. When part or whole of a manuscript was already published to conference papers, research reports, and dissertations, then the corresponding author should note it clearly in the manuscript.

Copyright

After published to JOET, the copyright of manuscripts should belong to KSOE. A transfer of copyright (publishing agreement) form can be found in submission website (http://www.joet.org).

Manuscript submission

Manuscript should be submitted through the on-line submission website (http://www.joet.org). The date that manuscript was received through on-line website is the official date of receipt. Other correspondences can be sent by an email to the Editor in Chief or secretariat. The manuscript must be accompanied by a signed statement that it has been neither published nor currently submitted for publication elsewhere. The manuscript should be written in English or Korean. Ensure that online submission are in a standard word processing format. Corresponding author must write the manuscript using the JOET template provided in Hangul or MS Word format. Ensure that graphics are high-resolution. Be sure all necessary files have been uploaded/ attached.

Authors' checklist

Please refer to “Authors' Checklist” for details.

Article structure

Manuscript must be edited in the following order: (1) Title, (2) Authors' names and affiliations, (3) Keywords, (4) Abstract, (5) Nomenclature (optional), (6) Introduction, (7) Main body (analyses, tests, results, and discussions), (8) Conclusions, (9) Conflict of interest (optional), (10) Funding (optional), (11) Acknowledgements (optional), (12) References, (13) Appendices (optional), (14) Author’s ORCIDs.

Abstract

A concise and factual abstract is required. The abstract should state briefly the background, purpose and methods of the research, the principal results and conclusions. An abstract should be written in around 300 words. References are not cited in abstract whenever possible. Also, non-standard or uncommon abbreviations should be avoided, but if essential they must be defined at their first mention in the abstract itself.

Keywords

Immediately after the abstract, provide a maximum of 5 or 6 keywords.

Unit

Use the international system units(SI). If other units are mentioned, please give their equivalent in SI.

Equations

All mathematical equations should be c1early printed/typed using well accepted explanation. Superscripts and subscripts should be typed clearly above or below the base line. Equation numbers should be given in Arabic numerals enclosed in parentheses on the right-hand margin.

Tables

Tables should be numbered consecutively with Arabic numerals. Each table should be fully titled. All tables should be referred to in the texts.

Figures

Figures should be numbered consecutively with Arabic numerals. Each figure should be fully titled. All figures should be referred to in the texts. All the illustrations should be of high quality meeting with the publishing requirement with legible symbols and legends.

Conflict of interest

It should be disclosed here according to the statement in the Research and publication ethics regardless of existence of conflict of interest. If the authors have nothing to disclose, please state: “No potential

conflict of interest relevant to this article was reported."

Funding

Funding to the research should be provided here. Providing a FundRef ID is recommended including the name of the funding agency, country and if available, the number of the grant provided by the funding agency. If the funding agency does not have a FundRef ID, please ask that agency to contact the FundRef registry (e-mail: fundref.registry@crossref.org). Additional detailed policy of FundRef description is available from http://www.crossref.org/fundref/. Example of a funding description is as follows:

The study is supported by the Inha University research fund (FundRef ID: 10.13039/501100002632), and the Korea Health Personnel Licensing Examination Institute research fund (FundRef ID: 10.13039/501100003647).

Acknowledgments

Any persons that contributed to the study or the manuscript, but not meeting the requirements of an authorship could be placed here. For mentioning any persons or any organizations in this section, there should be a written permission from them.

References in text

References in texts follow the APA style. Authors can also see how references appear in manuscript text through the 'Template'.

Reference list

Reference list follows the APA style. Authors can see how references should be given in reference section through the 'Template'.

Appendices

The appendix is an optional section that can contain details and data supplemental to the main text. If there is more than an appendix, they should be identified as A, B, C, etc. Formulae and equations in appendices should be given separate numbering: Eq. (A1), Eq. (A2), etc.; in a subsequent appendix, Eq. (B1) and so on. Similarly for tables and figures: Table A1; Fig. A1, etc.

ORCID (Open Researcher and Contributor ID)

All authors are recommended to provide an ORCID. To obtain an ORCID, authors should register in the ORCID web site: http://orcid.org. Registration is free to every researcher in the world. Example of ORCID description is as follows:

Joonmo Choung: https://orcid.org/0000-0003-1407-9031

Peer review and publication process

The peer review process can be broadly summarized into three groups: author process, review process, and publishing process for accepted submissions. General scheme is presented in Figure 1.

Check-in process for review

If the manuscript does not fit the aims and scope of the Journal or does not adhere to the Instructions to Authors, it may be rejected immediately after receipt and without a review. Before reviewing, all submitted manuscripts are inspected by Similarity Check powered by iThenticate (https://www.crossref.org/services/similarity-check/), a plagiarism-screening tool. If a too high degree of similarity score is found, the Editorial Board will do a more profound content screening.

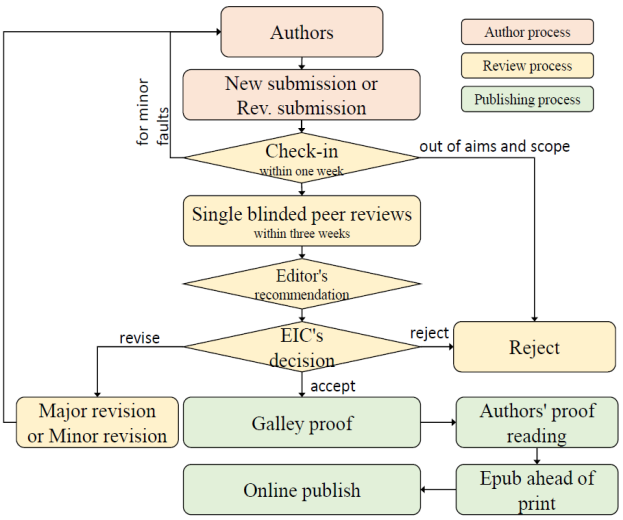

Figure 1 Flow chart of the peer review and publication process of JOET

The criterion for similarity rate for further screening is usually 15%; however, rather than the similarity rate, the Editorial Board focuses on cases where specific sentences or phrases are similar. The settings for Similarity Check screening are as follows: It excludes quotes, bibliography, small matches of 6 words, small sources of 1%, and the Methods section.

Number of reviewers

Reviewers will be selected from the list of reviewers. Manuscripts are then peer reviewed by at least 2 experts in the corresponding field, usually by 2.

Peer review process and the author response to the reviewer comments

JOET adopts single blind review, which means that the authors do not know the identity of the reviews. All papers, including those invited by the Editor, are subject to peer review.

The review period is 4 weeks. Usually the first decision is made within a week after completion of the review. The Editorial Board's decision after the review will be one of followings: Accept, Minor revision, Major revision, or Rejection. The Editorial Board may request the authors to revise the manuscript according to the reviewers' comments. If there are any requests for revision of the manuscript by the reviewers, the authors should do their best to revise the manuscript. If the reviewer's opinion is not acceptable or is believed to misinterpret the data, the author should reasonably indicate that. After revising the manuscript, the author should upload the revised files with a separate response sheet to each item of the reviewer's commentary. The author's revisions should be completed within 3 months after the request. If it is not received by the due date, the Editorial Board will notify the author. To extend the revision period beyond 3 months, the author should negotiate that with the Editorial Board. The manuscript review process can be provided for up two rounds. If the authors wish further review, the Editorial Board may consider it. The Editorial Board will make a final decision on the approval of the submitted manuscript for publication and can request any further corrections, revisions, and deletions of the article text if necessary. Statistical editing is also performed if the data requires professional statistical review by a statistician.

Processing after acceptance

If the manuscript is finally accepted, the galley proof will be sent to the corresponding author after professional manuscript editing and English proofreading. Proofreading should be performed for any misspellings or errors by the authors. Proofreading manuscript for publication is provided to the corresponding author, and the corresponding author must review the proofreading manuscript. Corresponding authors are responsible for the content of the proofreading manuscript and any errors. After final proofreading, the manuscript may appear at the journal homepage as an article in press with a unique DOI number for rapid communication. All published articles will be replaced by the replacement XML file and a final PDF.

Feedback after publication

If the authors or readers find any errors, or contents that should be revised, it can be requested from the Editorial Board. The Editorial Board may consider erratum, corrigendum or a retraction. If there are any revisions to the article, there will be a CrossMark description to announce the final draft. If there is a reader's opinion on the published article with the form of Letter to the editor, it will be forwarded to the authors. The authors can reply to the reader's letter. Letter to the editor and the author's reply may be also published.

How the journal handle complaints and appeals

The policy of JOET is primarily aimed at protecting the authors, reviewers, editors, and the publisher of the journal. If not described below, the process of handling complaints and appeals follows the guidelines of the Committee of Publication Ethics available from: https://publicationethics.org/appeals

- *Who complains or makes an appeal?*

Submitters, authors, reviewers, and readers may register complaints and appeals in a variety of cases as follows: falsification, fabrication, plagiarism, duplicate publication, authorship dispute, conflict of interest, ethical treatment of animals, informed consent, bias or unfair/inappropriate competitive acts, copyright, stolen data, defamation, and legal problem. If any individuals or institutions want to inform the cases, they can send a letter via the contact page on our website: https://www.joet.org/about/contact.php. For the complaints or appeals, concrete data with answers to all factual questions (who, when, where, what, how, why) should be provided.

- *Who is responsible to resolve and handle complaints and appeals?*

The Editorial Board or Editorial Office is responsible for them. A legal consultant or ethics editor may be able to help with the decision making.

- *What may be the consequence of remedy?*

It depends on the type or degree of misconduct. The consequence of resolution will follow the guidelines of the Committee of Publication Ethics (COPE).

Article processing charge

Payment due

Article processing charge (APC) covers the range of publishing services JOET provides. This includes provision of online tools for editors and authors, article production and hosting, and customer services. Upon editorial acceptance of an article for the regular review service and upon submission of an article for the fast review service, the corresponding author will be notified that payment is due.

APC

The APC up to 6 pages is ₩200,000 (or ＄200) and ₩550,000 (or ＄550) for the for the regular and fast review services, respectively. An extra APC of $50 per page is charged for papers longer than 6 pages, No taxes are included in this charge. For the fast review service, an advance fee of ₩250,000 ($250) should be paid on submission.

Payment methods

Credit card payment can be made online using a secure payment form as soon as the manuscript has been editorially accepted. We will we send a receipt by email once payment has been processed. Please note that payment by credit card carries a surcharge of 10% of the total APC.

Invoice payment is due within 7 days of the manuscript receiving editorial acceptance. Receipts are available on request.

Journal of Ocean Engineering and Technology 00(0), 000-000, December, 2100
https://doi.org/10.26748/KSOE.2100.000
pISSN 1225-0767
eISSN 2287-6715

Original Research Article, Technical Article, Review Article, etc

Title of Article

Firstname Lastname[1], Firstname Lastname[2] and Firstname Lastname[3]

[1]*Professor, Department of OO, OO School, OO University, Busan, Korea*
[2]*Graduate Student, Department of OO, OO University, Seoul, Korea*
[3]*Senior Researcher, Department of OO, OO Engineering. Corp., Seoul, Korea*

KEY WORDS: Lumped mass line model, Explicit method, Steel lazy wave riser (provide a maximum of 5 or 6 keywords.)

ABSTRACT: *A concise and factual abstract is required. The abstract should state briefly the background, purpose and methods of the research, the principal results and conclusions. An abstract should be written in around 300 words. References are not cited in abstract whenever possible. Also, non-standard or uncommon abbreviations should be avoided, but if essential they must be defined at their first mention in the abstract itself.*

Nomenclature (Optional)

ITOC	Increment of total operating cost ($/yr)
LHV	Lower heating value (kJ/kg)
Pw	Power (kW)
T	Temperature (K)
V	Volume (m^3)
ρ	Density (kg/m^3)

1. Introduction

The introduction should briefly place the study in a broad context and highlight why it is important. It should define the purpose of the work and its significance. The current state of the research field should be reviewed carefully and key publications cited. Please highlight controversial and diverging hypotheses when necessary. Finally, briefly mention the main aim of the work and highlight the principal conclusions. As far as possible, please keep the introduction comprehensible to scientists outside your particular field of research.

2. General Information for Authors

2.1 Research and Publication Ethics

Authorship should be limited to those who have made a significant contribution to the conception, design, execution, or interpretation of the reported study. All those who have made significant contributions should be listed as co-authors. Where there are others who have participated in certain substantive aspects of the research project, they should be acknowledged or listed as contributors.

The corresponding author should ensure that all appropriate co-authors and no inappropriate co-authors are included on the paper, and that all co-authors have seen and approved the final version of the paper and have agreed to its submission for publication.

Details on publication ethics are found in the journal's website (http://joet.org/authors/ethics.php). For the policies on research and publication

Received 00 February 2100, revised 00 October 2100, accepted 00 October 2100
Corresponding author Firstname Lastname: +82-51-759-0656, e-mail@e-mail.com
It is a recommended paper from the proceedings of 2019 spring symposium of the Korea Marine Robot Technology (KMRTS).

ethics not stated in the Instructions, Guidelines on Good Publication (http://publicationethics.org/) can be applied.

2.2 Requirement for Membership

One of the authors who submits a paper or papers should be member of The Korea Society of Ocean Engineers (KSOE), except a case that editorial board provides special admission of submission.

2.3 Publication Type

Article types include scholarly monographs (original research articles), technical articles (technical reports and data), and review articles. The paper should have not been submitted to other academic journal. When part or whole of a manuscript was already published to conference papers, research reports, and dissertations, then the corresponding author should note it clearly in the manuscript.

Example: It is noted that this paper is revised edition based on proceedings of KAOST 2100 in Jeju.

2.4 Copyright

After published to JOET, the copyright of manuscripts should belong to KSOE. A transfer of copyright (publishing agreement) form can be found in submission website (http://www.joet.org).

2.5 Manuscript Submission

Manuscript should be submitted through the on-line submission website (http://www.joet.org). The date that manuscript was received through on-line website is the official date of receipt. Other correspondences can be sent by an email to the Editor in Chief or secretariat. The manuscript must be accompanied by a signed statement that it has been neither published nor currently submitted for publication elsewhere. The manuscript should be written in English or Korean. Ensure that online submission are in a standard word processing format. Corresponding author must write the manuscript using the JOET template provided in Hangul or MS Word format. Ensure that graphics are high-resolution. Be sure all necessary files have been uploaded/ attached.

2.5.1 Authoer's checklist

Authoer's checklist and Transfer of copyright can be found in submission hompage (http:/www.joet.org).

3. Manuscript

Manuscript must be edited in the following order: (1) Title, (2) Authors' names and affiliations, (3) Keywords, (4) Abstract, (5) Nomenclature (optional), (6) Introduction, (7) Main body (analyses, tests, results, and discussions), (8) Conclusions, (9) Conflict of interest (optional), (10) Funding (optional), (11) Acknowledgements (optional), (12) References, (13) Appendices (optional), (14) Author's ORCIDs.

3.1 Unit

Use the international system units(SI). If other units are mentioned, please give their equivalent in SI.

3.2 Equations

All mathematical equations should be clearly printed/typed using well accepted explanation. Superscripts and subscripts should be typed clearly above or below the base line. Equation numbers should be given in Arabic numerals enclosed in parentheses on the right-hand margin. The parameters used in equation must be defined. They should be cited in the text as, for example, Eq. (1), or Eqs. (1)–(3).

$$G_{GEV}(x;\mu,\sigma,\xi)=\begin{cases}\exp[-(1+\xi(x-\mu)/\sigma)^{-1/\xi}] & \xi\neq 0\\ \exp[-\exp(-(x-\mu)/\sigma)] & \xi=0\end{cases} \tag{1}$$

in which μ, σ, and ξ represent the location ("Shift" in figures), scale, and shape parameters, respectively.

3.3 Tables

Tables should be numbered consecutively with Arabic numerals. Each table should be typed on a separate sheet of paper and be fully titled. All tables should be referred to in the texts.

Table 1 Tables should be placed in the main text near to the first time they are cited

Item	Buoyancy riser
Segment length[1)] (m)	370
Outer diameter (m)	1.137
Inner diameter (m)	0.406
Dry weight (kg/m)	697
Bending rigidity ($N \cdot m^2$)	1.66E8
Axial stiffness (N)	7.098E9
Inner flow density ($kg \cdot m^3$)	881
Seabed stiffness ($N/m/m^2$)	6,000

[1)]Tables may have a footer.

3.4 Figures

Figures should be numbered consecutively with Arabic numerals. Each figure should be fully titled. All the illustrations should be of high quality meeting with the publishing requirement with legible symbols and legends. All figures should be referred to in the texts. They should be referred to in the text as, for example, Fig. 1, or Figs. 1−3.

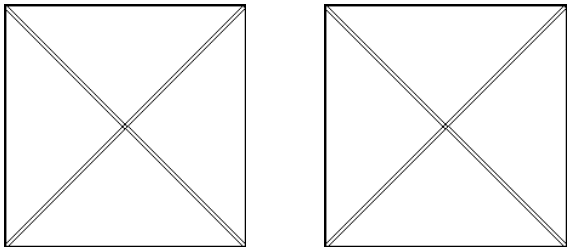

(a) Description of what is contained in the first panel

(b) Description of what is contained in the first panel

Fig. 1 Schemes follow the same formatting. If there are multiple panels, they should be listed as: (a) Description of what is contained in the first panel; (b) Description of what is contained in the second panel. Figures should be placed in the main text near to the first time they are cited

3.5 How to Describe the References in Main Texts

All references should be listed at the end of the manuscripts, arranged in order of Alphabet. References in texts follow the American Psychological Association (APA) style. The exemplary form of listed references is as follows:

Single author: (Kim, 1998) or Kim (1998)

Two authors: (Kim and Lee, 2000) or Kim and Lee (2000)

Three or more authors: (Kim et al., 1997) or Kim et al. (1997)

Two or more papers: (Lee, 1995a; Lee, 1995b; Ryu et al., 1998)

Year unknown: (Kim, n.d.) or Kim (n.d.)

4. Results

This section may be divided by subheadings. It should provide a concise and precise description of the experimental results, their interpretation as well as the experimental conclusions that can be drawn. Tables and figures are recommended to present the results more rapidly and easily. Do not duplicate the content of a table or a figure with in the Results section. Briefly describe the core results related to the conclusion in the text when data are provided in tables or in figures. Supplementary results can be placed in the Appendix.

5. Discussion

Authors should discuss the results and how they can be interpreted in perspective of previous studies and of the working hypotheses. The findings and their implications should be discussed in the broadest context possible. Future research directions may also be highlighted

6. Conclusions

This section can be added to the manuscript.

Conflict of Interest (Optional)

It should be disclosed here according to the statement in the Research and publication ethics regardless of existence of conflict of interest. If the authors have nothing to disclose, please state: “No potential conflict of interest relevant to this article was reported.”

Funding (Optional)

Please add: “This research was funded by Name of Funder, grant number XXX” and “The OOO was funded by XXX”. Check carefully that the details given are accurate and use the standard spelling of funding agency names at https://search.crossref.org/funding

Acknowledgments (Optional)

In this section you can acknowledge any support given which is not covered by the author contribution or funding sections. This may include administrative and technical support, or donations in kind (e.g., materials used for experiments). For mentioning any persons or any organizations in this section, there should be a written permission from them.

References

- Journal name should not be abbreviated.
- A private report with limited access or download availability can not be a reference.
- Include the digital object identifier DOI or URL for all references where available.
- Reference list follows the American Psychological Association (APA) style.

Referring to journal publications:

Author, A.A., Author, B.B., & Author, C.C. (Year). Title of Article. Journal Title, vol(no), pp–pp. https://doi.org/xx.xxxx/xxxxxx

Author, A.A., Author, B.B., Author, C.C. (accepted; in press). Title of Article. Title of Periodical. Retrieved from http://xx.xxx/x.pdf

Lee, T.K., Kim, T.W., Rim, C.W., & Kim, S.C. (2013). A Study on Calculation of Local Ice Pressures for ARAON Based on Data Measured at Arctic Sea. Journal of Ocean Engineering and Technology, 27(5), 88–92. https://doi.org/10.5574/KSOE.2013. 27.5.088

Lee, T.K., Kim, T.W., Rim, C.W., & Kim, S.C. (accepted; in press). A Study on Calculation of Local Ice Pressures for ARAON Based on Data Measured at Arctic Sea. Journal of Ocean Engineering and Technology, Retrieved from http://xxx.xxx/xxx.pdf

Referring to conference proceedings:

Author, A.A., Author, B.B., & Author, C.C. (Year). Title of Article. Proceeding Title, City, Country, pp–pp. https://doi.org/xx.xxxx

Aoki, S., Liu, H., & Sawaragi, T. (1994). Wave Transformation and Wave Forces on Submerged Vertical Membrane. Proceedings of International Symposium Waves - Physical and Numerical Modeling, Vancouver, Canada, 1287–1296.

Tsukamoto, C.L., Lee, W., Yuh, J., Choi, S.K., & Lorentz, J. (1997). Comparison Study on Advanced Thruster Control of Underwater Robots. Proceedings of International Conference on Robotics and Automation, 1845–1850. https://doi.org/110.1109/ROBOT.1997.619056

Referring to books:

Author, A.A. (Year). Title of Book (xx ed.). Location: Publisher.

Strunk, W., & White, E.B. (2000). The Elements of Style (4th ed.). NewYork, USA: Longman.

Schlichting, H. (1968). Boundary Layer Theory (6th ed.). New York, USA: McGraw-Hill.

Referring to theses or dissertations:

Author, A.A. (Year). Title of Doctoral Dissertation or Master’s thesis (Doctoral Dissertation or Master’s thesis). Name of Institution, City, Country.

Giovanni, I. (1998). Modelling and Identification of Underwater Robotic Systems (Ph.D. Thesis). University of Genova, Genova, Italy.

Referring to technical reports, rules, or guidelines:

Author, A.A. (Year). Title of report (Reprot No. xxx), Location: Publisher.

Likhomanov, V. (2010). Full-Scale Ice Trials of the Korean Research Icebreaker ARAON. Daejeon, Korea: Arctic and Antarctic Research Institute (AARI).

ABS. (2011). Guide for Ice Loads Monitoring Systems. Houston, USA: American Bureau of Shipping.

Lloyd's Register. (2011). FDA ICE Fatigue Induced by Ice Loading, ShipRight Design and construction - Fatigue Design Assesment. London, United Kingdom: Lloyd's Register.

Larson, M., & Kraus, N.C. (1989). SBEACH: Numerical Model for Simulating Storm-Induced Beach Change - Report 1 Empirical Foundation and Model Development (Technicla Report CERC-89-9). Coastal Engineering research center Vicksburg Ms.

Referring to patents:

Righsholder, A.A. (Year). Title of Patent. Patent number, Patent office with country.

Dawoo Shipbulding & Maringe Engineering (DSME). (2013). Distance Length Standardization Method for Preventing Interference at the time of Uploading Cell Guide of Container Ship. Unexamined Patent Publication 1020130044635, Korean Interllectual Property Office.

Referring to websites:

Righsholder, A.A. (Year). Title of webpage. Retrieved Month Year from http://xxxx

International Association of Classification Societies (IACS). (2010a). Common Structural Rules for Bulk Carriers. Retrieved July 2010 from http://www.iacs-data.org.uk

US Congressional Hearing. (2009). Strategic Importance of the Arctic in Us Policy. Retrieved June 2019 from https://fas.org/irp/arctic.pdf

Dawoo Shipbulding & Maringe Engineering (DSME). (2013). Distance Length Standardization Method for Preventing Interference at the time of Uploading Cell Guide of Container Ship. Retrieved June 2019 from https://patentimages.storage./pdfs/792.pdf

Referring to software:

Righsholder, A.A. (Year). Title of Software. Downloaded Month Year from http://xxxx

Standard

Organization. (Year). Title of the standard in italics [Translated title − if applicable] (Standard No.). Retrieved from https://...

International Organization for Standardization. (2005). Industrial sewing machines: Safety requirements for sewing machines, units and systems (ISO Standard No. 10821). Retrieved from http://www.standard.no/no/Nettbutikk/produktkatalogen/Produktpresentasjon/?ProductID=113554

Translation

Author, A. A. (Year of publication). Title of work: Capital letter also for subtitle (T. Translator, Trans.). Location: Publisher. (Original work published YEAR). DOI

Ura, T., & Takakawa, S. (2015). All about Submersibles (W.S. Kim, D.S. Kim, Y.H. Choi,.C.H. Park, J.S. Park, P.M. Lee, H.S. Jung, Trans.). Korea: CIR. (Original Work Published in 1994, Japan: Seizan-Shoten Publiching)

in text: (Ura and Takakawa, 1994/2015)

Referring to some exceptional cases:

- when authors are missing, institution can replace authors

National Oceanic and Atmospheric Administration (NOAA). (2015). Deep-ocean Assessment and Reporting of Tsunamis (DART). Retrieved December 2019 from https://nctr.pmel.noaa.gov/Dart/

- when dates or years are missing, it is replaced with "n.d."

National Oceanic and Atmospheric Administration (NOAA). (n.d.). Deep-ocean Assessment and Reporting of Tsunamis (DART).

- when more then seven authors, first 6 authors ... last author.

Yeu, T., Choi, H.T., Lee, Y., Chae, J., Lee, Y., Kim, S.S., ... Lee, T.H. (2019). Development of Robot Platform for Autonomous Underwater Intervention. Journal of Ocean Engineering and Technology, 33(2), 168−177. https://doi.org/10.26748/KSOE. 2019.021

Appendix (Optional)

The appendix is an optional section that can contain details and data supplemental to the main text. For example, explanations of experimental details that would disrupt the flow of the main text, but nonetheless remain crucial to understanding and reproducing the research shown; figures of replicates for experiments of which representative data is shown in the main text can be added here if brief, or as Supplementary data. Mathematical proofs of results not central to the paper can be added as an appendix.

All appendix sections must be cited in the main text. In the appendixes, Figures, Tables, etc. should be labeled starting with 'A', e.g., Fig. A1, Fig. A2, etc.

Examples:

https://doi.org/10.26748/KSOE.2019.022

https://doi.org/10.26748/KSOE.2018.4.32.2.095

Author ORCIDs

All authors are recommended to provide an ORCID. To obtain an ORCID, authors should register in the ORCID web site: http://orcid.org. Registration is free to every researcher in the world. Example of ORCID description is as follows:

Author name	ORCID
So, Hee	0000-0000-000-00X
Park, Hye-Il	0000-0000-000-00X
Yoo, All	0000-0000-000-00X
Jung, Jewerly	0000-0000-000-00X

Authors' Checklist

The following list will be useful during the final checking of a manuscript prior to sending it to the journal for review. Please submit this checklist to the KSOE when you submit your article.

< Checklist for manuscript preparation >

☐ I checked my manuscript has been 'spell-checked' and 'grammar-checked'.
☐ One author has been designated as the corresponding author with contact details such as
- E-mail address
- Phone numbers

☐ I checked abstract 1) stated briefly the purpose of the research, the principal results and major conclusions, 2) was written in around 300 words, and 3) did not contain references (but if essential, then cite the author(s) and year(s)).
☐ I provided 5 or 6 keywords.
☐ I checked color figures were clearly marked as being intended for color reproduction on the Web and in print, or to be reproduced in color on the Web and in black-and-white in print.
☐ I checked all table and figure numbered consecutively in accordance with their appearance in the text.
☐ I checked abbreviations were defined at their first mention there and used with consistency throughout the article.
☐ I checked all references mentioned in the Reference list were cited in the text, and vice versa according to the APA style.
☐ I checked I used the international system units (SI) or SI-equivalent engineering units.

< Authorship checklist >

JOET considers individuals who meet all of the following criteria to be authors:

☐ Made a significant intellectual contribution to the theoretical development, system or experimental design, prototype development, and/or the analysis and interpretation of data associated with the work contained in the article.
☐ Contributed to drafting the article or reviewing and/or revising it for intellectual content.
☐ Approved the final version of the article as accepted for publication, including references.

< Checklist for publication ethics >

☐ I checked the work described has not been published previously (except in the form of an abstract or as a part of a published lecture or academic thesis).
☐ I checked when the work described has been published previously in other proceedings without copyright, it has clearly noted in the text.
☐ I checked permission has been obtained for use of copyrighted material from other sources including the Web.
☐ I have processed Plasgiarism Prevention Check through reliable web sites such as www.kci.go.kr, http://www.ithenticate.com/, or https://www.copykiller.org/ for my submission.
☐ I agree that final decision for my final manuscript can be changed according to results of Plasgiarism Prevention Check by JOET administrator.
☐ I checked one author at least is member of the Korean Society of Ocean Engineers.
☐ I agreed all policies related to 'Research and Publication Ethics'
☐ I agreed to transfer copyright to the publisher as part of a journal publishing agreement and this article will not be published elsewhere including electronically in the same form, in English or in any other language, without the written consent of the copyright-holder.
☐ I made a payment for reviewing of the manuscript, and I will make a payment for publication on acceptance of the article.
☐ I have read and agree to the terms of Authors' Checklist.

Title of article	:	
Date of submission	: DD/MM/YYYY	
Corresponding author	:	signature
Email address	:	

※ E-mail this with your signature to ksoehj@ksoe.or.kr

Publishing Agreement

ARTICLE DETAILS

Title of article :

Corresponding author :

E-mail address :

DOI : https://doi.org/10.26748/KSOE.2XXX.XXX

YOUR STATUS

I am one author signing on behalf of all co-authors of the manuscript.

ASSIGNMENT OF COPYRIGHT

I hereby assign to the Korean Society of Ocean Engineers, the copyright in the manuscript identified above and any tables, illustrations or other material submitted for publication as part of the manuscript (the "Article"). This assignment of rights means that I have granted to Korean Society of Ocean Engineers the exclusive right to publish and reproduce the Article, or any part of the Article, in print, electronic and all other media (whether now known or later developed), in any form, in all languages, throughout the world, for the full term of copyright, and the right to license others to do the same, effective when the Article is accepted for publication. This includes the right to enforce the rights granted hereunder against third parties.

SCHOLARLY COMMUNICATION RIGHTS

I understand that no rights in patents, trademarks or other intellectual property rights are transferred to the Journal owner. As the author of the Article, I understand that I shall have: (i) the same rights to reuse the Article as those allowed to third party users of the Article under the CC-BY-NC License, as well as (ii) the right to use the Article in a subsequent compilation of my works or to extend the Article to book length form, to include the Article in a thesis or dissertation, or otherwise to use or re-use portions or excerpts in other works, for both commercial and non-commercial purposes. Except for such uses, I understand that the assignment of copyright to the Journal owner gives the Journal owner the exclusive right to make or sub-license commercial use.

USER RIGHTS

The publisher will apply the Creative Commons Attribution-Noncommercial Works 4.0 International License (CC-BY-NC) to the Article where it publishes the Article in the journal on its online platforms on an Open Access basis.
The CC-BY-NC license allows users to copy and distribute the Article, provided this is not done for commercial purposes and further does not permit distribution of the Article if it is changed or edited in any way, and provided the user gives appropriate credit (with a link to the formal publication through the relevant DOI), provides a link to the license, and that the licensor is not represented as endorsing the use made of the work. The full details of the license are available at http://creativecommons.org/licenses/by-nc/4.0/legalcode.

REVERSION OF RIGHTS

Articles may sometimes be accepted for publication but later rejected in the publication process, even in some cases after public posting in "Articles in Press" form, in which case all rights will revert to the author.

☑ I have read and agree to the terms of the Journal Publishing Agreement.

Corresponding author:

name signature

※ E-mail this with your signature to ksoehj@ksoe.or.kr (Papers will not be published unless this form is signed and returned)

Research and Publication Ethics

Journal of Ocean Engineering and Technology (JOET) adheres to the guidelines published by professional organizations, including Committee on Publication Ethics (COPE; https://publicationethics.org/)

1. Authorship

JOET considers individuals who meet all of the following criteria to be authors:

1) Made a significant intellectual contribution to the theoretical development, system or experimental design, prototype development, and/or the analysis and interpretation of data associated with the work contained in the article.
2) Contributed to drafting the article or reviewing and/or revising it for intellectual content.
3) Approved the final version of the article as accepted for publication, including references.

Contributors who do not meet all of the above criteria may be included in the Acknowledgment section of the article. Omitting an author who contributed to your article or including a person who did not fulfill all of the above requirements is considered a breach of publishing ethics.

Correction of authorship after publication: JOET does not correct authorship after publication unless a mistake has been made by the editorial staff.

2. Originality and Duplicate Publication

All submitted manuscripts should be original and should not be in consideration by other scientific journals for publication. Any part of the accepted manuscript should not be duplicated in any other scientific journal without permission of the Editorial Board, although the figures and tables can be used freely if the original source is verified according to the Creative Commons Attribution License (CC BY-NC). It is mandatory for all authors to resolve any copyright issues when citing a figure or table from other journal that is not open access.

3. Conflict-of-Interest Statement

Conflict of interest exists when an author or the author's institution, reviewer, or editor has financial or personal relationships that inappropriately influence or bias his or her actions. Such relationships are also known as dual commitments, competing interests, or competing loyalties. These relationships vary from being negligible to having a great potential for influencing judgment. Not all relationships represent true conflict of interest. On the other hand, the potential for conflict of interest can exist regardless of whether an individual believes that the relationship affects his or her scientific judgment. Financial relationships such as employment, consultancies, stock ownership, honoraria, and paid expert testimony are the most easily identifiable conflicts of interest and the most likely to undermine the credibility of the journal, the authors, or of the science itself. Conflicts can occur for other reasons as well, such as personal relationships, academic competition, and intellectual passion. If there are any conflicts of interest, authors should disclose them in the manuscript. The conflicts of interest may occur during the research process as well; however, it is important to provide disclosure. If there is a disclosure, editors, reviewers, and reader can approach the manuscript after understanding the situation and the background of the completed research.

4. Management Procedures for the Research and Publication Misconduct

When JOET faces suspected cases of research and publication misconduct such as a redundant (duplicate) publication, plagiarism, fabricated data, changes in authorship, undisclosed conflicts of interest, an ethical problem discovered with the submitted manuscript, a reviewer who has appropriated an author's idea or data, complaints against editors, and other issues, the resolving process will follow the flowchart provided by the Committee on Publication Ethics (http://publicationethics.org/resources/flowcharts). The Editorial Board of JOET will discuss the suspected cases and reach a decision. JOET will not hesitate to publish errata, corrigenda, clarifications, retractions, and apologies when needed.

5. Editorial Responsibilities

The Editorial Board will continuously work to monitor and safeguard publication ethics: guidelines for retracting articles; maintenance of the integrity of the academic record; preclusion of business needs from compromising intellectual and ethical standards; publishing corrections, clarifications, retractions, and apologies when needed; and excluding plagiarism and fraudulent data. The editors maintain the following responsibilities: responsibility and authority to reject and accept articles; avoiding any conflict of interest with respect to articles they reject or accept; promoting publication of corrections or retractions when errors are found; and preservation of the anonymity of reviewers.

6. Hazards and human or animal subjects

If the work involves chemicals, procedures or equipment that have any unusual hazards inherent in their use, the author must clearly identify these in the manuscript. If the work involves the use of animal or human subjects, the author should ensure that the manuscript contains a statement that all procedures were performed in compliance with relevant laws and institutional guidelines and that the appropriate institutional committee(s) has approved them. Authors should include a statement in the manuscript that informed consent was obtained for experimentation with human subjects. The privacy rights of human subjects must always be observed.

Ensure correct use of the terms sex (when reporting biological factors) and gender (identity, psychosocial or cultural factors), and, unless inappropriate, report the sex and/or gender of study participants, the sex of animals or cells, and describe the methods used to determine sex and gender. If the study was done involving an exclusive population, for example in only one sex, authors should justify why, except in obvious cases. Authors should define how they determined race or ethnicity and justify their relevance.

7. Secondary publication

It is possible to republish manuscripts if the manuscripts satisfy the conditions of secondary publication. These are:

- The authors have received approval from the Editorial Board of both journals (the editor concerned with the secondary publication must have access to the primary version).
- The priority for the primary publication is respected by a publication interval negotiated by editors of both journals and the authors.
- The paper for secondary publication is intended for a different group of readers
- The secondary version faithfully reflects the data and interpretations of the primary version.
- The secondary version informs readers, peers, and documenting agencies that the paper has been published in whole or in part elsewhere, for example, with a note that might read, "This article is based on a study first reported in the [journal title, with full reference]"
- The title of the secondary publication should indicate that it is a secondary publication (complete or abridged republication or translation) of a primary publication.

8. Complaints and Appeals

The process of handling complaints and appeals follows the guidelines of the COPE available from: https://publicationethics. org/appeals

9. Post-publication discussions and corrections

The post-publication discussion is available through letter to editor. If any readers have a concern on any articles published, they can submit letter to editor on the articles. If there found any errors or mistakes in the article, it can be corrected through errata, corrigenda, or retraction.

The Korean Society of Ocean Engineers